Numerical and experimental study of airfoils with porous trailing edge

Simone Tamaro

Technische Universiteit Delft

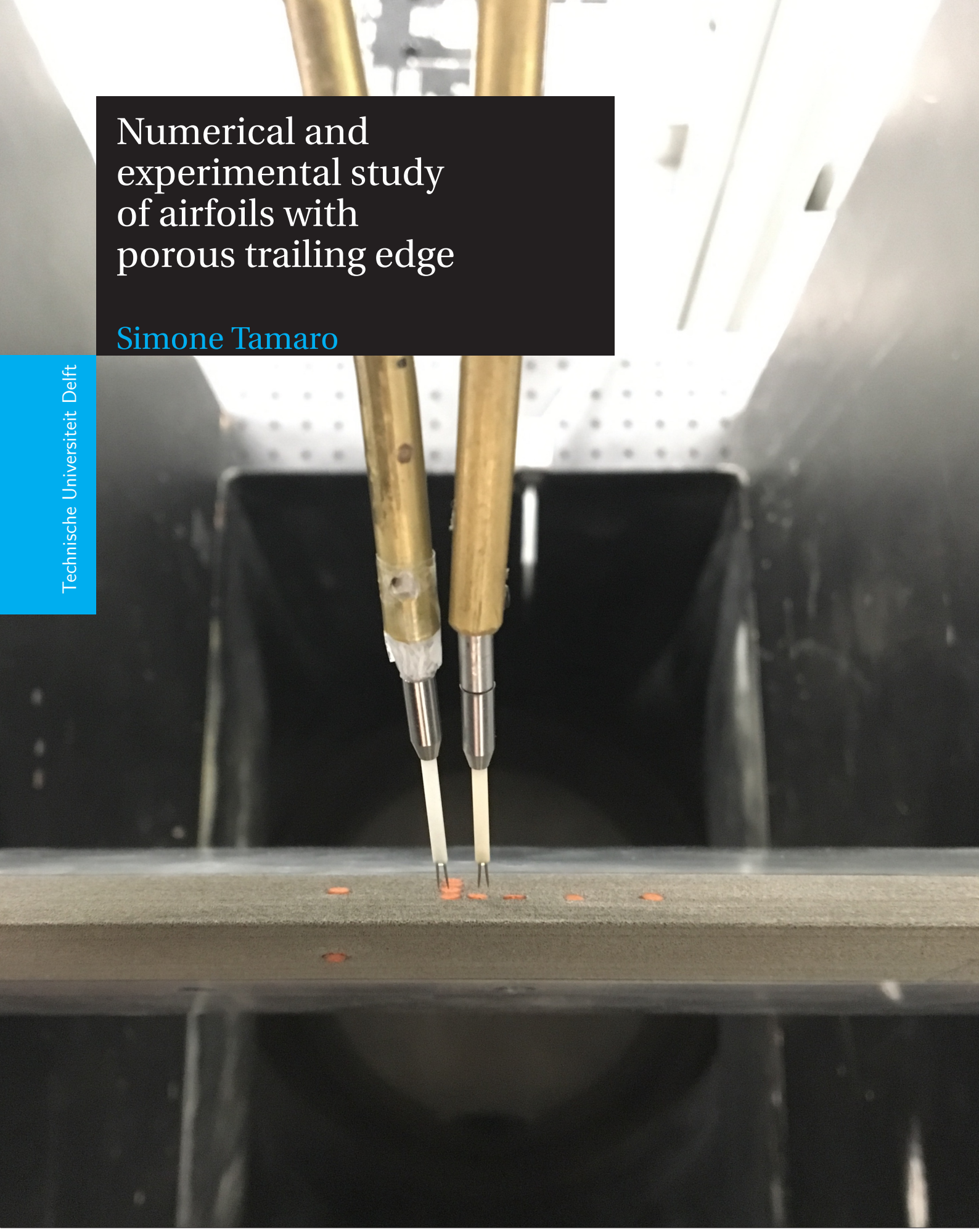

TU Delft Delft University of Technology

Challenge the future

Numerical and experimental study of airfoils with porous trailing edge

by

Simone Tamaro

in partial fulfillment of the requirements for the degrees

Master of Science
in Engineering (European Wind Energy)

at The Technical University of Denmark,

Master of Science
in Aerospace Engineering

at the Delft University of Technology,

to be defended publicly on Friday August 23rd, 2019 at 10:00 AM.

Supervisors:	Dr. F. Avallone	TU Delft
	Dr. D. Ragni	TU Delft
	Prof. W. Z. Shen	DTU
Thesis committee:	Dr. F. Avallone	TU Delft
	Prof.dr. D. Casalino	TU Delft
	Dr. D. Ragni	TU Delft
	Dr. M. Reck	GEA
	Prof. W. Z. Shen	DTU

TU Delft Delft University of Technology

Danmarks Tekniske Universitet DTU EWEM

Abstract

The addition of porous material to the trailing edge of airfoils was studied numerically and experimentally. The purpose of this work is to inspect whether the penalization method can be successfully used to describe flows through porous media. In the numerical study, the penalization method was applied to the incompressible Navier-Stokes equations. The flow has been studied with turbulent, unsteady simulations. The SIMPLE algorithm and a mixed scale model for LES were used in EllipSys2D. The code was validated with a test case on a flat plate. In this case, porous inserts are capable of suppressing vortex shedding by mitigating the pressure discontinuity at the trailing edge. An agreement with wind tunnel data could be observed both in the wake and in the boundary layer.
The code was then applied to study a NACA0018 airfoil at zero angle of attack. In this case, porous materials reduce the energy content of turbulent signals in the wake. The power spectral density of pressure fluctuations in correspondence of the porous insert is reduced in the whole spectrum. The same airfoil was considered with the addition a single roughness element to trip the boundary layer at 20% of the chord. The height of the step was chosen from the results of a sensitivity analysis. The presence of the trip triggers turbulence transition successfully. Pressure drag for the porous case was found to be dependent on the presence of the trip.
In the experimental study, measurements were taken on a symmetric NACA0018 airfoil at zero angle of attack. Hot-wire anemometry and surface microphones were used to measure the flow. Porous inserts with different permeabilities have been studied. Porous materials at the trailing edge increase the shear of velocity profiles in the boundary layer and reduce the power spectral density of pressure fluctuations in correspondence of the trailing edge.
According to this study, the penalization method is a promising tool to study flows through porous media.

Preface

Preface I would like to thank Professor Wen Zhong Shen from DTU for being a great supervisor. He always provided me with help no matter where he was and really helped me to learn. I would also like to thank Professors Daniele Ragni and Francesco Avallone in Delft for the continuous incitement to do more and do better. I learned so much from them. All my supervisors have been committed, serious and helpful even in the hardest moments. I am grateful for this.

I have to thank Syamir Alihan Showkat Ali and Professor Azerpayvand for being so kind to share their wind tunnel results with me. I like the academic environment because of acts of collaboration like this one.

I would like to mention many friends who helped me through the hardest times. These are Patrick, Erin, Jesse, Gert-Jan, Reinier, Sebastian, Federico and Rogier. I shared an unforgettable journey with them. A special thanks goes to Filippo for the great support and to Erica, Virginia, Asier, Fabio, Jules, Stefano and Elena for their friendship. Thank you Francesca for staying close to me in this important step of my life.
I want to thank also Francesca, Luca and Simone from Trieste who did not forget about me after two years I have been abroad.

Lastly, I would like to thank my family, which is the most precious thing I have in life. I would like to thank my sister Cecilia for being always close to me no matter what. I would like to thank my parents allowed me to be where I am now. I will always be grateful for all the sacrifices they made for me. Thank you for teaching me the values of respect and equality. This thesis is dedicated to you and I hope it will make you happy.

Kongens Lyngby, July 2019

Contents

List of Symbols

α	Constant for LES
β	Thermal expansion coefficient
δ	Average pore size
Δ	Average cell size LES
δ^*	Boundary layer displacement thickness
η	Curvilinear coordinate (orthogonal)
$\mathcal{F}$	Polynomial function for source tripping
μ	Dynamic viscosity
ν	Kinematic viscosity
ν_t	Eddy viscosity
ϕ	Porosity
τ	Viscous stress tensor
τ_0	Residual term spatial averaging LES
θ	Boundary layer momentum thickness
ξ	Curvilinear coordinate (streamwise)
ζ	Angle perpendicular to airfoil at trip location
$\mathbf{u}$	Horizontal velocity, vector
$\mathbf{v}$	Vertical velocity, vector
$\mathbf{U}$	Velocity vector
A	Finite volume EWNS coefficients
c	Chord length
C	Courant number
C_0	Constant for LES
C_D	Drag coefficient
C_F	Forchheimer coefficient
C_L	Lift coefficient
c_p	Specific heat (constant pressure)
C_p	Pressure coefficient
c_p	Specific heat (constant pressure)
c_s	Speed of sound
D	Drag force

E	Voltage
f	Frequency
G	Mass flux
H	Shape factor boundary layer
h	Body reference height
J	Jacobian of coordinate transformation
K	Permeability
k	Kinetic energy
K_{ND}	Coefficient of permeability
L	Lift force
L^*	Reference length
p	Pressure
P_0	Incompressible pressure splitting technique
P_i	Polynomial coefficients
R	Air flow resistivity
$R_{\text{operating}}$	Operating resistance hot wire probe
R_{tot}	Total resistance hot wire anemometry
R_{20}	Resistance of hot wire probe measured at 20 °C
Re	Reynolds number
Re_p	Pore size Reynolds number
S_0	Entropy
S	Source term
S_{trip}	Perturbating source term for tripping
St	Strouhal number
T	Temperature
TI	Turbulence intensity
U	Horizontal velocity component
U', u'	Horizontal velocity component fluctuation
U_{RMS}	Root mean square of horizontal velocity
U_f	Friction velocity
V	Vertical velocity component
V', v'	Horizontal velocity component fluctuation
V_{RMS}	Root mean square of vertical velocity
$\mathbf{v}_d$	Darcy velocity
x	Horizontal coordinate
X	Horizontal coordinate 2nd coordinate system and measurements
y	Vertical coordinate
Y	Vertical coordinate 2nd coordinate system and measurements
y^+	Non-dimensional wall distance
Z	Streamwise coordinate wind tunnel experiment

Z	Non-dimensional wall distance wind tunnel experiment

List of abbreviations

2D	Two-dimensional
3D	Three-dimensional
CAA	Computational aeroacoustics
CFD	Computational Fluid Dynaimcs
DNS	Direct numerical simulation
EIA	Environmental impact assessment
EWNS	East-west-north-south (*compass* sum)
FD	Finite difference
FFT	Fast Fourier transform
FV	Finite volume
HW	Hot-wire
HWA	Hot-wire anemometry
LDA	Laser doppler anemometry
LEE	Linarized Euler equations
LES	Large eddy simulation
NLDE	Nonlinear disturbance equations
PIV	Particle image velocimetry
PSD	Power spectral density
RANS	Reynolds averaged Navier-Stokes equations
RMS	Root mean square
SIMPLE	Semi-Implicit Method for Pressure-Linked Equations
SPL	Sound pressure level
TE	Trailing edge

Chapter 1

Introduction

1.1 Background

The modern idea of wind power started with pioneering work of inventors in Denmark in the 70ies. Wind turbines have evolved and changed their look in the course of the years. Their efficiency and reliability are today higher than ever. Nowadays, power extraction from wind represents a solid branch of the energy industry worldwide. Bids for planning and construction of wind farms are constantly submitted by manufacturers both onshore and offshore. The industry of wind energy is constantly developing and it is almost ready to challenge fossil fuels as primary sources of energy. From an academic point of view, wind energy research fosters the development of new ideas and concepts in many, multidisciplinary contexts.
One of the many issues which usually arise in an Environmental Impact Assessment (EIA) of a wind farm, or in the development phase of a new turbine model is linked to noise emissions. Currently, wind turbines must operate within the limitations set by national laws to protect the health of those exposed.
Among the sound sources from a wind turbine, it is possible to list mechanical sources such as generators and gear-boxes. However, the main contributor to the total sound power level is noise generated aerodynamically at the trailing edge of the blades of the turbines. This occurs when turbulent boundary layer structures interact with the trailing-edge. This mechanism is such that noise is directed towards an observer on the ground every time one of the blades moves towards it.

1.2 Motivation

Noise emission is a crucial parameter which affects the development of wind turbines. In the industry, this parameter influences important production phases such as research & development, manufacturing, and business plans. Companies

are therefore very interested in studying the phenomenon and to find solutions. Different researches have been carried in Universities to limit the aerodynamically-generated sound from blades. Among the most recent developments in sound reduction, the local application of porous materials at the trailing-edge of airfoils is one of the most promising. An example is showed in Figure 1.1.

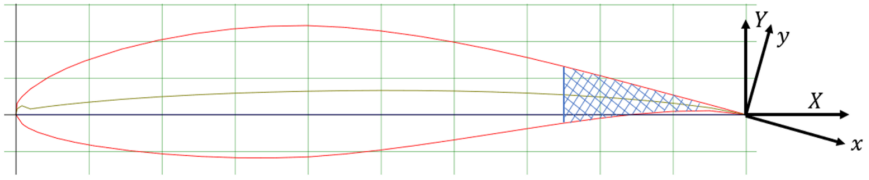

Figure 1.1: NACA 64618 airfoil with porous insert at the trailing edge ($0.2c$) and coordinate systems.

Nowadays, research on porous materials for sound reduction is highly needed to understand the phenomena involved and optimize their application. This thesis aims at contributing to the current line of research both numerically and experimentally.
In the numerical part, porous media has been included in the Navier-Stokes equations. Specifically, the penalization method has been applied on collocated, curvilinear grids with the aim of inspecting if computational fluid dynamics (CFD) can resolve flows through partially porous airfoils.
In the experimental part, near-wall velocity data has been acquired. The results of the study are used to analyse the relationship between sound reduction and fluid-porous material interaction.

1.3 Thesis outline

This document is organized as follows. First, a review of the current literature is given in Chapter 2. In Chapter 3, the numerical model is presented, and the method is described. The code is validate in Chapter 4 with a test case. In Chapter 5, the code is used to solve airfoil flows on a partially porous symmetric airfoil. The experimental part of the work is described in Chapter 6. The wind tunnel set-up and instrumentations are treated, as well as calibration and finally results.

Chapter 2

Theoretical basis and literature review

2.1 Introduction

This chapter includes the literature study. First, basic concepts in aeroacoustics are discussed. Next, a focus on numerical methods is presented. In this section of the chapter, the main challenges and the main methods are described and compared. An overview of the most relevant experiments on partially porous airfoils follows. Finally, the research questions are listed.

2.2 Fundamentals of wind turbine aeroacoustics

The role of wind turbines in supplying green energy is constantly increasing worldwide. In 2018 Wind energy has indeed been the second largest power generating capacity in the European Union [1]. Noise is however one of the main concerns related to the installation of wind turbines. Questionnaires from Pedersen et al. [2] showed that exposure to noise from wind turbines can lead to physical diseases for those exposed. Nowadays, national laws worldwide limit the maximum sound power level which can be emitted by a wind turbine. Thus, reducing noise emissions could significantly increase the number of installed turbines. The highest benefit would be for onshore projects, for which noise is currently a critical aspect. Oerlemans et al. [3] performed experimental measurements on wind turbines noise emission. This research showed that the main noise component emitted by modern wind turbines is the so-called *broadband trailing edge*. Broadband trailing edge noise is due to a turbulent boundary layer travelling downstream a solid body and interacting with its trailing-edge. A *medium impedance* discontinuity between the airfoil and the wake is believed to be the reason for the noise mechanism which is

responsible for trailing-edge noise [4].
Other mechanisms for noise generation from wind turbine airfoil are stall separation, vortex shedding in laminar boundary layer conditions and due to trailing edge bluntness. The latter is relevant in the inner regions of wind turbine blades, where airfoils with low bluntness ratio are applied for structural and anti-erosive properties. Usually bluntness-noise lies at high frequencies and its level is low compared to the broadband component. The Strouhal number is a parameter which is often used to describe vortex shedding phenomena. It is defined as an adimensional frequency f

$$St = \frac{fL^*}{U}$$

for a flow with speed U and a characteristic length L^*.
Two sketches for the broadband and bluntness mechanisms are presented in Figure 2.1.

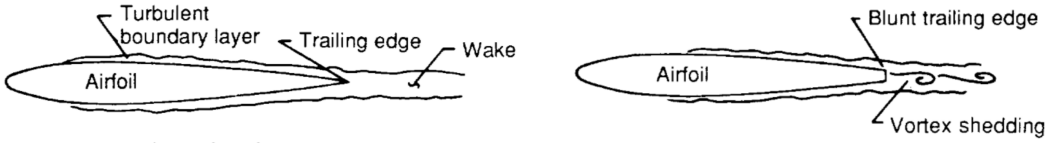

(a) Broadband mechanism **(b)** Bluntness mechanism

Figure 2.1: Trailing-edge noise mechanisms [5].

Trailing-edge sawtooth serrations have proven to be effective tools for noise reduction [6]. Although these devices showed promising results, their main drawback lies in a noise increase at the high frequencies. One of the most recent and innovative solutions for sound reduction from wind turbines is the application of porous materials to the trailing edge of the blades. Nowadays, metallic foam materials are being tested in the industry and academia. These materials have showed promising results with noise reduction especially at low frequencies. Porous materials could be competitors to serrations, which usually perform poorly at high frequencies. However, the aerodynamic effects introduced are different from those observed with serrations. Moreover, trailing edge serrations are easier to tune from an industrial point of view. As a consequence, applying porous materials to wind turbine blades to successfully reduce noise emission requires a deep analysis and study. The aerodynamic effects of porous materials on airflows are not trivial. Extensive wind-tunnel measurements have been performed and provided a comprehensive insight on the phenomena at stake [7–9]. Nevertheless, some aspects are still to be fully understood. For this reason, numerical methods are needed to support experiments and provide further developments to the physics of the phenomena involved.

2.3 Numerical methods

Numerical methods in aeroacoustics are usually referred to as *computational aeroacoustics* (CAA) methods. CAA can successfully predict noise generation from aerodynamic phenomena. Usually it is combined with CFD. CFD was first developed in the 60ies. CFD is a branch of fluid dynamics, used to predict flow fields in many situations. Nowadays CFD has become a mature method following the constant development of computers, with the possibility of running simulations on multiprocessor computers with parallel computations. Furthermore, methods such as *Finite Volume* (FV) and *Finite Difference* (FD) accelerated the development of CFD due to their ease of implementation.

Compared to classical problems in aerodynamics, CAA introduces new challenges. The main one is that the wavelength of the acoustic wave is larger than the one of the hydrodynamic fluctuations. Thus, obtaining a solution for the acoustic pressure field with ordinary CFD methods can be prohibitive due to computational costs. CAA methods can be split in two categories.
The first one involves analytically based approaches. These methods allow to compute the far-field sound information from the near field solution. This is done with analytical expressions. Usually these methods are coupled to CFD methods, such as the Lattice Boltzmann Method.
In the second category, the Navier-Stokes equations are used to describe the acoustic field. A short description of the main options in this case is presented below.

- **Direct Numerical Simulation**: this method requires high computational power and it is usually limited to low Reynolds number flows.
- **Large Eddy Simulation**: this technique is generally not capable of resolving the flow and the acoustic waves at once due to the different scales.
- **Linearized Euler equations (LEE)**: the method involves a decomposition of the variables in mean, turbulent and acoustic components. This method might suffer from excited hydrodynamic instabilities.
- **Aerodynamic/Acoustic splitting technique**: this method is based on the original formulation of Hardin and Pope [10]. The advantage of this technique is that the source strength is directly obtained, providing information on both sound radiation and scattering.
- **Nonlinear disturbance equations (NLDE)**: this method is similar to the splitting technique. In this case the variables in the Navier-Stokes are

decomposed in a mean and fluctuating component. This method was developed with the idea of extending the splitting technique to high Mach number flows.

- **Acoustic perturbation equations (APE)**: this method is divided in two steps. First, the region where sound generation occurs is solved as an unsteady, compressible problem. The acoustic perturbations equation is then solved in a computational domain which is defined around the previous.

It is also worth to mention *semi-empirical models* based on wind tunnel measurements as alternatives to CAA. Although these models are the simplest, their results and accuracy can be poor as they rely on experimental results.
The aerodynamic/acoustic splitting technique is very suitable to low Mach number flows. The computational costs are similar to an incompressible calculation, and the technique is reliable.
In the next section, a description of the aerodynamic/aeroacoustic splitting technique is presented.

2.3.1 Aerodynamic/aeroacoustic splitting technique

The aerodynamic/acoustic splitting technique was first developed by Pope and Hardin [10]. The method consists of a non-linear two steps procedure, in which the time-dependent incompressible (aerodynamic) flow is solved first for a given problem. The solution is used later to compute the lower energy (acoustic) sound field, described by a compressible solution. The compressible Navier-Stokes equations in indicial form are made of the conservation of mass, the conservation of momentum, the energy equation and an equation of state. They are presented below

$$\begin{aligned} &\frac{\partial \rho}{\partial t} + \frac{\partial}{\partial x_i}(\rho u_i) = 0 \\ &\frac{\partial}{\partial t}(\rho u_i) + \frac{\partial}{\partial x_j}(\rho u_i u_j + p_{ij}) = 0 \\ &p = p(\rho, S) \\ &T\frac{DS_0}{Dt} = c_p \frac{DT}{Dt} - \frac{\beta T}{\rho}\frac{Dp}{Dt} \end{aligned} \tag{2.1}$$

where S_0 is entropy, ρ is density, T is temperature, p pressure, u_i represents the velocity component in the x_i coordinate, c_p is the specific heat at constant pressure and β the coefficient of thermal expansion.
The splitting techniques is divided in two steps.

1st step First, the incompressible solution is computed. The incompressible Navier-Stokes equations in indicial form are expressed as:

$$\frac{\partial U_i}{\partial x_i} = 0$$

$$\frac{\partial U_i}{\partial t} + \frac{\partial}{\partial x_j}(U_i U_j) = \frac{1}{\rho_0}\frac{\partial P_0}{\partial x_i} + \nu \frac{\partial^2 U_i}{\partial x_j \partial x_j} = 0$$

with P_0, U_i and ρ_0 being the incompressible pressure, velocity and ambient density. The kinematic viscosity ν is defined as $\nu = \mu/\rho$, with μ dynamic viscosity of the fluid. Numerical methods to solve the incompressible Navier-Stokes equations are discussed in Section 2.3.2.

2nd step Once step one has been completed, all the compressible variables can be defined as the sum of the computed incompressible contribution and their relative fluctuations u_i', p', ρ'.

$$\begin{aligned} u_i &= U_i + u_i' \\ p &= P_0 + p' \\ \rho &= \rho_0 + \rho' \end{aligned} \tag{2.2}$$

These decompositions can be inserted into the continuity and momentum equations of the inviscid, compressible Navier-Stokes formulation

$$\frac{\partial \rho'}{\partial t} + \frac{\partial f_i}{\partial x_i} = 0$$

$$\frac{\partial f_i}{\partial t} + \frac{\partial}{\partial x_j}\left[f_i(U_j + u_j') + \rho_0 U_i u_j' + p'\delta_{ij} \right] = 0$$

with $f_i = \rho u_i' + \rho' U_i$. In order to close the system of equations, pressure can be expressed as a function of density with the speed of sound c_s (equation of state for pressure i.e. $p = p(S, \rho)$):

$$\frac{\partial p'}{\partial t} - c_s^2 \frac{\partial \rho'}{\partial t} = -\frac{\partial P_0}{\partial t}$$

and closure is finally achieved with the further assumption that for a general flow

$$c_s^2 = \frac{\gamma p}{\rho} \tag{2.3}$$

where γ is the ratio between the specific heat at constant pressure and at constant volume. For a diatomic gas such as air it assumes the value of 1.4. Note that this relationship may not be valid inside a porous material. At this point, the

compressible Navier-Stokes equations can be solved for the fluctuating terms.
The aerodynamic/acoustic splitting technique is limited to low Mach number flows ($\approx$Ma$<$ 0.3), as it requires the validity of the incompressible solution.
A numerical procedure to compute the aerodynamic and acoustic fields is presented in the next section.

2.3.2 Solution strategy on 2D non-orthogonal collocated grids

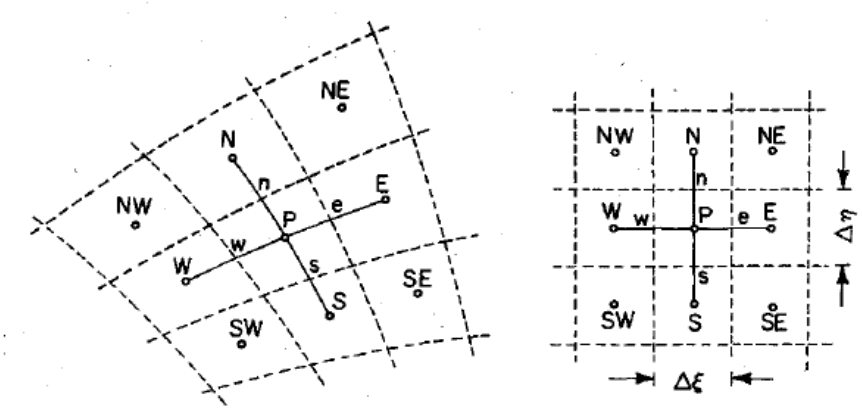

Figure 2.2: Curvilinear grid (left) and relative cartesian grid (right) [11].

The CFD code *EllipSys 2D* will be used in the numerical part of this thesis project. It is based on collocated grids and curvilinear, non-orthogonal meshes. These kind of meshes are made of curved elements which generally are not perpendicular at their intersections. An example of non-orthogonal mesh is presented in Figure 2.2 left, with the relative Cartesian coordinates displayed on the right.
On *collocated grids*, all the variables are stored in the same positions (i.e. cell centers). The alternative to collocated grids are *staggered grids*, in which different grids are used for storing pressure and velocity. An example of two dimensional grid for spatial discretization is presented in Figure 2.3.

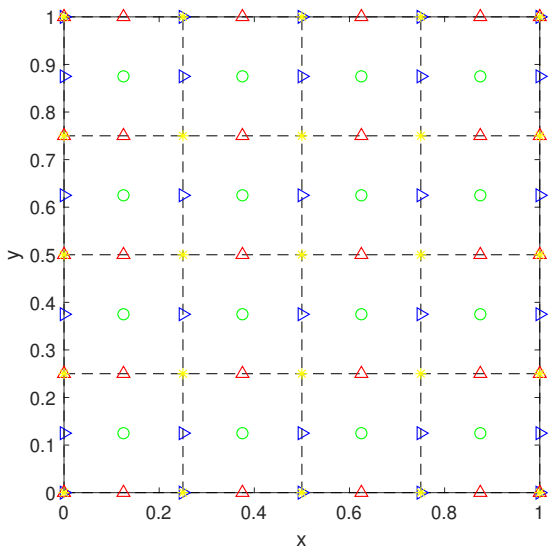

Figure 2.3: 2D staggered grids for spatial discretization.

On collocated grids all the variables are stored in the green circles (cell centers). On staggered grids instead, only pressure is computed in the center of the cells. With regards to Figure 2.3, the two components of velocities are defined on the blue and red triangles respectively. These points lie on the cell boundaries of the pressure grid. This is beneficial when solving the Navier-Stokes equations to compute gradients. Furthermore, staggered grids are effective in avoiding pressure velocity decoupling. This phenomenon occurs when weak linkage exists between local pressure and velocity. Collocated grids usually perform poorly in this sense, and one of their main drawback is indeed the emergence of pressure oscillations. A brief presentation of the problem follows.

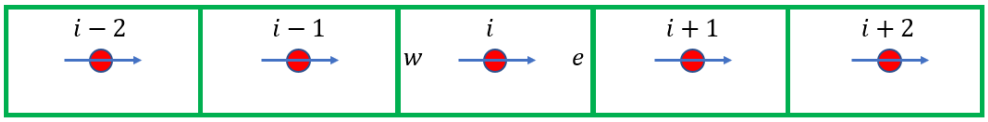

Figure 2.4: 1-D collocated grid.

We consider a one-dimensional collocated grid as in Figure 2.4. On this grid, information at the cell faces must be interpolated from adjacent cell centers. If

linear interpolation is applied to evaluate pressure, we have that

$$p_w = 0.5(p_{i-1} + p_i)$$

$$p_e = 0.5(p_i + p_{i+1})$$

The net pressure force acting on a control volume is usually needed in the momentum equation, which links velocity and pressure. With finite volume, the net force acting on a cell with face area A can be expressed as

$$A(p_w - p_e) = 0.5A(p_{i-1} - p_{i+1})$$

It can be seen that weak linkage is present, as p_i does not appear in the equation. Hence, a big discontinuity between p_{i-1} (or p_{i+1}) and p_i would not be detected and the converged nonphysical solution would erroneously satisfy the Navier-Stokes equations. As a result, *odd-even decoupling* can occur i.e. pressure oscillations. This problem, is also known as *checkerboard oscillation*.

2.3.2.1 SIMPLE method and Rhie-Chow interpolation

Because of the considerations made above, collocated grids require a special solution technique. The *Semi-Implicit Method for Pressure-Linked Equations* (SIMPLE) approach can be used to avoid unstable pressure fluctuations [12]. The SIMPLE method requires two steps; a predictive step and then a corrective step. In the predictive step the momentum equation is solved for a known pressure field. The velocities obtained at this point generally do not satisfy continuity. In the corrective step, continuity is enforced by solving a pressure equation. Because at this point it is now the momentum equation which is not respected, this procedure is done iteratively until convergence.
The Rhie/Chow interpolation method can be used in the SIMPLE method to express pressure gradients into fluxes [11]. This method allows to compute coefficients and variables at the cell faces. Instead of linearly interpolating velocity between the momentum equations for neighbouring cells, which would lead to odd-even pressure decoupling (discussed in previous paragraph), Rhie and Chow proposed linear interpolation for all terms except for the pressure source in the momentum equation. Furthermore, the pressure source is directly extracted from the neighbouring cell centers.
In the next paragraphs, the SIMPLE algorithm is analyzed in details with the aid of Figure 2.5, which represents a classic 3×3 grid for finite volume formulations in CFD.

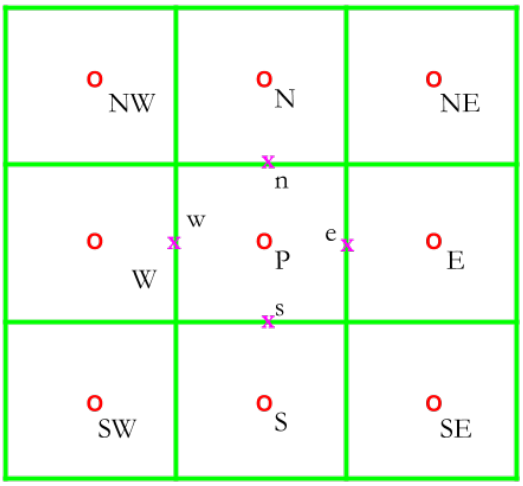

Figure 2.5: An example of grid for finite volume discretization.

Predictor step The two-dimensional finite volume formulation of the momentum equation for a grid like the one in Figure 2.5 can be expressed as

$$A_P U_P^{t+\Delta t} + A_W U_W^{t+\Delta t} + A_E U_E^{t+\Delta t} + A_S U_S^{t+\Delta t} + A_N U_N^{t+\Delta t} = S_T + S_V + S_F + S_P + S_C \tag{2.4}$$

where S_T represents the instationary term, S_V the volume source, S_F the *false source term* from the cross-diffusive fluxes, S_P the pressure source terms and finally S_C the terms from convection. The solution of the predictor step U_P^* from Equation 2.4 can be written as

$$U_P^* = \frac{S_{U,momentum} - \sum A_{nb} U_{nb}}{A_{P,U}} \tag{2.5}$$

with A_P and A_{nb} being respectively the coefficients for the center point and for the neighbour cell points which are computed from the finite volume discretization of the momentum equation. $\sum_{\text{EWNS}}$ indicates compass summation.
Considering now for instance the eastern wall, the horizontal-component of velocity is estimated on a curvilinear grid with the Rhie-Chow interpolation method as

$$U_e^* = \underbrace{\overline{\left(\frac{S_{U,momentum} - \sum A_{nb} U_{nb}}{A_{P,U}}\right)}_e}_{①} - \underbrace{\overline{\left(\frac{1}{A_{P,U}}\right)}_e \left[(\alpha_{\xi x})_e (p_E - p_P) + (\alpha_{\eta x})_e (p_{ne} - p_{se})\right]}_{②} \tag{2.6}$$

where the over-lined term are computed from linear interpolation and the asterisk * means that the velocity is obtained in the predictor step. $S_{u,momentum}$ includes all

the source terms from the momentum equations except the pressure source terms. These source terms are defined in the finite volume integration of the momentum equation from the diffusive fluxes. α, ξ and η are geometric parameters used to transform the Cartesian grid (defined in two-dimensions by x, y) into a curvilinear one. ξ and η are defined as in Figure 2.2 and are functions of the Cartesian coordinates x and y

$$\xi = \xi(x, y) \qquad \eta = \eta(x, y)$$

The first term in Equation 2.6 is a linear interpolation of the solution of the momentum equation in Equation 2.5 with the estimated pressure field before correction. The second term is an additional term which prevents non-physical oscillations. Here, *ne* and *se*, respectively the north-east and south-east coefficients for the cross-term pressure gradients, are needed due to the non-orthogonality of the mesh. Usually they can be approximated as

$$p_{ne} - p_{se} = \frac{1}{4}\Big[(p_N - p_S) + (p_{NE} - p_{SE})\Big]$$

The mass fluxes for a cell are defined as

$$G_1 = \rho U \alpha_{\xi x} + \rho V \alpha_{\xi y} \qquad G_2 = \rho U \alpha_{\eta x} + \rho V \alpha_{\eta y}$$

Following the Rhie Chow interpolation presented in Equation 2.6, the east flux can be expressed as

$$G^*_{1e} = \rho_e \Big[(\alpha_{\xi x})_e U^*_e + (\alpha_{\xi y})_e V^*_e\Big] \tag{2.7}$$

where ρ_e is computed by linear interpolation, and V^*_e is computed in the same way as U^*_e in Equation 2.6.
If a backward differentiation scheme in time is applied to solve the momentum equation, the cell centered velocities which are being interpolated in the first term of Equation 2.6 are of the form

$$U^*_P = \left[\frac{J\rho}{\delta t}(2U^n_P - 0.5U^{n-1}_P) - \sum_{\text{EWNS}} A_{nb} U^*_{nb}\right] \Big/ A^*_{P,U} \tag{2.8}$$

where n and $n-1$ indicate the time step considered.
When flux is computed with the Rhie-Chow interpolation method, fluxes at time step n (prior iteration) and $n-1$ (previous time step) are obtained from interpolating the necessary velocities. However, they have already been computed in the previous time steps and hence they can be directly used. Eventually, only one interpolation for the momentum equation coefficients is needed. This correction to the Rhie-Chow interpolation was proposed by Shen et al. in [13] and offered a

more robust procedure for the solution of unsteady flows on collocated grids. The corrected formulation is presented below

$$G_{1e}^{*} = \overline{\left(\frac{2J\rho/\delta t}{A_{P,U}}\right)}\bigg|_e G_{1e}^{n} - \overline{\left(\frac{0.5J\rho/\delta t}{A_{P,U}}\right)}\bigg|_e G_{1e}^{n-1} + \overline{H}\bigg|_e + \overline{\frac{B}{A_{P,U}}}(p_E^n - p_P^n) \quad (2.9)$$

where B is a geometric parameter to account for the curvilinear mesh, and H is a flux defined from the auxiliary velocities

$$U_{aux} = -\sum_{\text{EWNS}} \frac{A_{nb}U_{nb}^{*}}{A_{P,U}^{*}} \qquad V_{aux} = -\sum_{\text{EWNS}} \frac{A_{nb}V_{nb}^{*}}{A_{P,V}^{*}}$$

It can be seen that Equation 2.9 is directly linked to Equation 2.8. The correction lies in the fact that no overline is present above the fluxes, i.e. they are not interpolated but their known value is used instead. G_e^n is the flux at the prior iteration, while G_e^{n-1} is the converged flux from the previous time step.

Corrector step Once the momentum equation has been solved for the cell-center velocities and the velocities at the walls have been interpolated with the Rhie-Chow method, an equation for the pressure can be obtained by combining the momentum and continuity equations.
The current velocities from the predictor step defined at the cell centers do not generally satisfy continuity. The variables must thus be corrected as

$$\begin{aligned} U &= U^{*} + U^{C} \\ V &= V^{*} + V^{C} \\ p &= p^{*} + p^{C} \end{aligned} \quad (2.10)$$

where * indicates results from the predictor step, and ^{C} identifies the correction term.
At a cell face, the correction for the velocities U^C can be obtained by considering Equation 2.6 along with Equations 2.10, with the idea that the corrected value of U could theoretically be computed from Equation 2.6 if the corrected parameters were known. The following relation is obtained for the corrective term of the horizontal velocity component on an eastern face

$$U_e^C = \overline{\left(\frac{-\sum A_{nb}U_{nb}^{C}}{A_{P,U}}\right)}_e - \overline{\left(\frac{1}{A_{P,U}}\right)}_e \Big[(\alpha_{\xi x})_e(p_E^C - p_P^C) + (\alpha_{\eta x})_e(p_{ne}^C - p_{se}^C)\Big] \quad (2.11)$$

Now, in order to obtain a decoupled solution for pressure and velocity, the first term is neglected.

$$\overline{\left(\frac{-\sum A_{nb}U_{nb}^{C}}{A_{P,U}}\right)}_e \approx 0 \quad (2.12)$$

This is approximation is typical of the SIMPLE method. At this point, an equation for the pressure can be obtained if the fluxes G from the velocities in Equations 2.11 are inserted in the continuity equation

$$G_e^C + G_e^* - G_w^C - G_w^* + G_n^C + G_n^* - G_s^C - G_s^* = 0$$

The last equation can be rewritten as a pressure equation

$$A_P p_P^C + \sum A_{nb} p_{nb}^C = S_{mass} \tag{2.13}$$

This equation can be solved for the correction of the pressures at the cell center P_P. S_{mass} represents the *mass deficit*, defined as the balance of fluxes obtained from the momentum equation. This balance is generally different from zero because the velocities computed in the predictor step do not generally satisfy continuity.
At this point, pressure and velocity can be corrected together with an under-relaxation parameter α_P

$$p = p^* + \alpha_p p^C$$

taking an eastern face as an example, the corrected flux can be expressed as

$$G_e = G_e^* + A_E(p_E^C - p_P^C)$$

The SIMPLE algorithm proposed by Rhie and Chow is presented below, with the addition of the aerodynamic/acoustic splitting technique (the acoustic field is solved in steps 3.a, 3.b). A visual representation is plotted in Figure 2.6:

1. Solve the momentum equation with a known pressure distribution from the previous time-step, iteration or from a first guess. At this stage, the obtained velocity field does not generally satisfy continuity.

2. Solve the pressure-correction equation to enforce continuity. The pressure equation is obtained by inserting the correction for the cell face fluxes into the continuity equation. Once the pressure field is computed, the correction for the velocity field can be obtained as well.

3. Correct velocity and pressure. Generally, the cell centered velocities do not satisfy the momentum equation at this stage.

   (a) Apply the provisional incompressible pressure and velocity to the compressible acoustic model

   (b) Solve the compressible acoustic model with a predictor-corrector step as the one used for the aerodynamic field

4. If the field satisfy both continuity and momentum equations to the desired extent, a new time-step can be taken. Otherwise, the procedure is repeated until convergence. An under-relaxation parameter for pressure is often necessary.

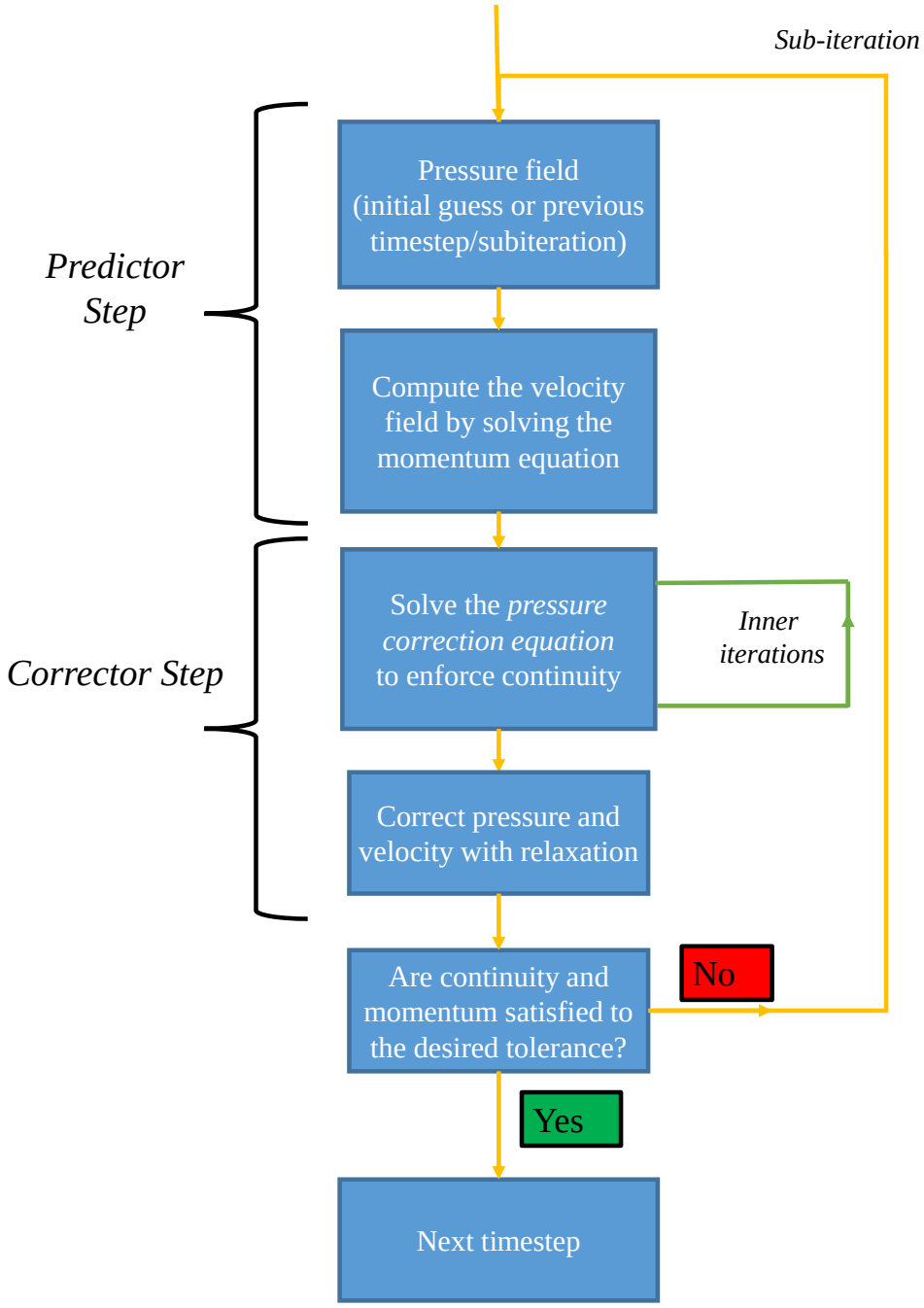

Figure 2.6: A schematic representation of the SIMPLE algorithm.

Next, relevant literature about the description of porous media flows in the Navier-Stokes equations is presented.

2.3.3 Description of porous materials with the Navier-Stokes equations

Intense research has been performed on the mathematical description of flows through porous media.

Darcy's law Darcy's law relates *Darcy velocity* $\mathbf{u}$ and pressure gradient $\nabla \mathbf{p}_p$ for a fluid in a porous media. Henry Darcy presented this result in [14], as part of his research on the development of a water supply for the city of Dijon in France in the 19$^{\text{th}}$ century. Darcy's law is presented in Equation 2.14 for a material with permeability $\mathbf{K}$, porosity ϕ and dynamic viscosity of the fluid μ

$$\mathbf{v}_d = -\frac{\mathbf{K}}{\mu}\nabla \mathbf{p}_p \tag{2.14}$$

where the Darcy velocity $\mathbf{v}_d$ can be considered [15] as

$$\mathbf{v}_d = \phi \mathbf{u}$$

Cimolin et al. defined a Reynolds number Re_p for the flow inside through the pores in [16]. This non-dimensional number allows to evaluate the validity of Darcy's Law. Re_p was defined as the product of the flow density, velocity and pore size (δ) divided by the dynamic viscosity coefficient as follows

$$Re_p = \frac{\rho U \delta}{\mu}$$

If Re_p is higher than one, inertial effects must be included and therefore more general models such as the Forchheimer equation must be used.

Forchheimer equation The Forchheimer equation describe the pressure gradient for a fluid due to the interaction with a porous material. It is made of a linear and a quadratic term. The latter is responsible for describing inertial effects. The Forchheimer equation is presented in Equation 2.15

$$\nabla \mathbf{p}_p = -\frac{\mu}{\mathbf{K}}\mathbf{v}_d - \rho\frac{C_F}{\sqrt{\mathbf{K}}}|\mathbf{u}|\mathbf{v}_d - C_{F,2}|\mathbf{u}|^2\mathbf{v}_d \tag{2.15}$$

where C_F is the *Ergun constant* or *Forchheimer coefficient*. The Ergun coefficient is dependent on the flow velocity. For low-speed flows, it assumes low values. Indeed, in these cases, inertial effects can be neglected and Darcy Equation is valid.

Commonly, and also in the present study, C_F is assumed to be dependent on the material used.
An evaluation of Re_p with typical values from wind tunnel experiments ($U = 10$ m/s, $\delta = 800$ μm) gives values above 300. This justifies the inclusion of the Forchheimer model in the current study.
Moreover, due to the very high Reynolds number of the flows to be inspected (i.e. to the order of 10^6), the addition of a cubic term was also considered in this study. Lage et al. inspected the validity of the Forchheimer Equation in [17]. In this study, the authors determined experimentally the pressure drop of a flow across porous test blocks. Their results showed the need of a cubic term in the Forchheimer Equation to describe high speed flows through porous media.

In a porous material, *permeability* is a parameter which describes to what extent the flow is influenced by the material. More specifically, it accounts for pressure losses due to flow viscosity. In its most general formulation, it is described by a symmetric and positive definite tensor, assuming values of infinity for a "void material", and zero for a solid one. In the former case, Darcy's law correctly predicts the absence of any pressure gradient.

$$\mathbf{K} = \begin{bmatrix} k_{11} & k_{12} & k_{13} \\ k_{21} & k_{22} & k_{23} \\ k_{31} & k_{32} & k_{33} \end{bmatrix}$$

Permeability can be measured experimentally for a homogeneous material according to the Hazen-Dupuit-Darcy equation [7]

$$\frac{\Delta p}{t} = \frac{\mu}{K} v_d + \rho C v_d^2$$

where t is the thickness of the sample, Δp is the static pressure drop across the sample, ρ is the density and C is the *form coefficient*, which describes pressure losses due to inertial effects.
Porosity provides an indication of how much void space is present inside the material and is defined as

$$\phi = 1 - \frac{\rho_p}{\rho_b}$$

where ρ_p is the density of the porous material and ρ_b is the density of the metallic alloy of the material. A porosity close to one characterizes light samples with high inner void space, while null porosity defines solid materials. Porosity and permeability can be functions of space and time [15].
Air flow resistivity R is defined for a homogeneous sample as

$$R = \frac{\Delta p}{t\, v_d} \tag{2.16}$$

This parameter is often used in literature to characterize different porous materials [8, 18]. A good approximation of this parameter for metallic materials [7] is

$$R = \mu/K$$

2.3.3.1 Penalization method

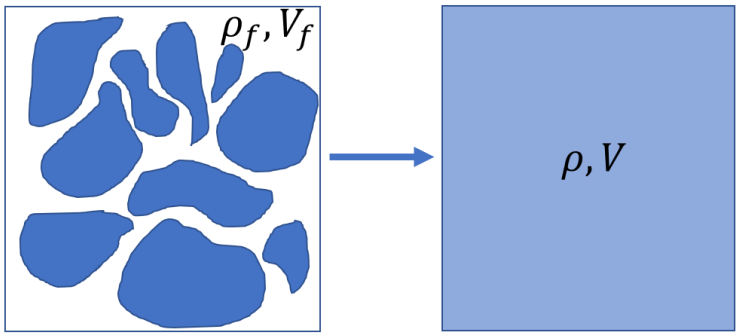

Figure 2.7: In the penalization method the porous domain on the left is considered as a homogenized volume with density and volume ρ and V, in which the Forchheimer equation is applied.

The most straightforward way to simulate flows through porous media is to directly include Darcy's law in the Navier-Stokes equations. This is done by reducing the complex porous region to a *fictitious domain* in which modified Navier-Stokes equations are used to describe the flow. This method is the Brinkman/Navier-Stokes or *penalization method*. As mentioned above, it involves the addition of a term to the momentum equation to account for the viscous damping of the velocities which occurs in the porous medium, as also proposed by [15]. This method is easy to implement, robust and efficient.
The modified versions of the vector form of the continuity and momentum equations include the penalization term from Darcy's law as well as a modified fluid density $\phi\rho$ to account for flow inside the pores. They are presented in Equation 2.17.

$$\begin{aligned} \frac{\partial \phi\rho}{\partial t} + \nabla \cdot (\phi\rho\mathbf{u}) &= 0 \\ \frac{\partial \phi\rho\mathbf{u}}{\partial t} + \nabla \cdot (\phi\rho\mathbf{u}\mathbf{u}) = -\nabla\mathbf{p} + \nabla \cdot \boldsymbol{\tau} + \phi\rho\mathbf{f} &- \underbrace{\mu\mathbf{K}^{-1}\phi\mathbf{u} - (\phi\rho)\phi^2\frac{C_F}{\sqrt{\mathbf{K}}}|\mathbf{u}|\mathbf{u} - \phi^3 C_{F,2}|\mathbf{u}|^2\mathbf{u}}_{Penalization} \end{aligned} \tag{2.17}$$

where $\mathbf{f}$ are the external body forces, τ is the tensor of the viscous stresses which, for a *Newtonian* fluid, can be expressed in indicial notation as

$$\tau_{ij} = \mu\left(\frac{\partial U_i}{x_j} + \frac{\partial U_j}{x_i}\right) - \frac{2}{3}\delta_{ij}\mu\frac{\partial U_k}{\partial x_k}$$

When the penalization method is employed, there is no need to mesh the flow obstacles or to treat the interface between porous and fluid media [19]. It is important to mention that the method is suitable for materials with porosity close to 1, which is consistent with the materials currently tested in wind tunnel measurements [7,9].

The majority of articles dealing with the penalization method in aerodynamics are mainly focused on passive flow control. Just recently, the method was adopted to specifically study aeroacoustics. For instance, the penalization method was implemented by Schulze et al. in [15] to optimize the permeability distribution of the trailing edge of a flat plate. In this case, the momentum equation of the Navier-Stokes equations is modified with the addition of a *Darcy term* consistently with the penalization method. Furthermore, the density of the fluid inside the porous material was corrected with the porosity ϕ as in Equation 2.17.

$$\rho_{porous} = \rho\phi$$

An optimization framework based on the Lagrangian multipliers was developed by the authors to compute the optimal permeability distribution in space. According to this study, towards the leading edge solid materials are required, while towards the trailing edge, complex distributions of porosities are needed. Reductions of almost 20 dB compared to a non-optimized porous set-up were estimated by the study.

The challenge of the numerical part of this thesis work is to implement a porous model for the estimation of noise emission from airfoils in turbulent unsteady flows.

2.4 Experimental literature

Data from wind tunnel analysis showed that the study of velocity profiles and spectra could be useful to understand the effects of porous materials on turbulence. This is because turbulent flows are responsible for broadband trailing edge noise. Inspecting turbulence is one meaningful way to predict noise. Furthermore, analyzing the spectrum of the turbulent signals can be a valid method to understand which noise mechanisms are playing a role.

2.4.1 Results from wind tunnel experiments

In this section, four relevant articles on the application of porous materials to the trailing edge section of airfoils and flat plates are reviewed. The main parameters used by the authors are presented in Table 2.1.

Table 2.1: Summary of the main measurement parameters for the papers reviewed.

Paper	TE porosity	Reynolds #	Airfoil	Year
Geyer et al. [8, 18]	96 - 99%	3.8×10^5-8.5×10^5	SD 7003	2014
Showkat Ali et al. [9]	74.8% & 90.2%	6×10^5	Flat plate	2018
Rubio et al. [7]	89.3% & 91.7%	2.63×10^5	NACA 0018	2018

Geyer et al. In [18] the sound intensity and spectrum of a half-symmetric SD 7003 type airfoil entirely made of different porous materials were compared with a reference non-porous airfoil in the aeroacoustic wind tunnel at BTU Cottbus. Five different materials with different flow resistivities and porosities between 96% and 99% were chosen. A strong dependency between lift and flow resistivity of the material was observed, with a higher lift for higher resistivities. An opposite trend was instead described for the drag force. No such simple relationship between material properties and noise emissions could be determined. This work showed sound reductions up to 10 dB with, however, increased noise at high frequencies. On the other hand, it was observed that the aerodynamic performance of a fully porous airfoil is significantly reduced compared to the solid one. In general, this research suggested the need to localize the porous material at the trailing edge. This was done among others by Geyer and Sarradj [8].
The authors performed experiments at a chord-based Reynolds number between 3.8×10^5 and 8.5×10^5. Airfoils were tripped. Drag increased with decreasing flow resistivity. The authors suggest that this is due to the larger size of the pores with a lower flow resistivity. From the acoustic point of view, some porous media showed a narrow peak in the spectrum of the turbulent velocity fluctuations. The authors explained that this could be linked to the presence of a *false edge* in the chord-wise location when the porous material is introduced. This edge is responsible for vortex shedding due to the "false bluntness" of the airfoil. It is interesting to notice that some materials used in the experiments did not lead to a reduction of sound power level in the entire frequency range. Overall, a high dependency of the measured quantities on the material used was observed.
Boundary layer quantities measured with HWA showed that a reduction of flow resistivity leads to increasing thickness of the turbulent boundary layer. This is linked to the higher surface roughness which is also responsible for the higher drag. Turbulence spectra from partially porous airfoils was found to be lower than the

solid one only at high Strouhal numbers, meaning that trailing edge noise is reduced in this frequency range. At low Strouhal numbers, turbulent fluctuations of partially porous airfoils are higher than non-porous airfoil. This is inconsistent with [7, 9]. The authors commented on this, stating that in this frequency range porous airfoils may take to a reduction of overall noise, but could as well increase it. Noise reductions at high Strouhal numbers was instead linked to the frequency reduction of the turbulence spectra. In addition to this, at high frequencies it is assumed that the small turbulent structures interact with the porous surface with which energy is exchanged in the form of heat. The authors refer to this process as *hydrodynamic damping*.

Showkat Ali et al. Among the most recent papers on wind tunnel experiments, an extensive overview of the flow characteristics has been provided by Showkat Ali et al. [9]. The aim of the work was to accurately study the properties of the boundary layer and the wake of a partially porous flat plate. Two materials with 90.2% and 74.8% porosity and flow resistivities of 8.2×10^{-8} m^2 and 7.7×10^{-9} m^2 were tested and compared to a solid one. Results from PIV regarding trailing-edge flow, highlighted a significant delay in the vortex shedding phenomenon with increasing porosity. The high porosity material implied lower flow acceleration upstream of the trailing edge, with a more streamlined flow. The changes observed are explained by the authors to be linked to

1. the penetration of the boundary flow into the pores of the material
2. the consequent creation of an *internal hydrodynamic field*
3. a discharge process of the latter into the wake.

The results from the study of boundary layers indicated the non-validity of the non-slip boundary condition for porous surfaces. The horizontal velocity overshoot observed with a fully solid plate in the trailing-edge (TE) region is significantly reduced when porous materials are applied. This is because the acceleration at the TE due to pressure difference is milder. Although the velocity profiles for the low-porosity TE are generally similar to those of the solid case, the root-mean-square (RMS) values are indeed lower. The highly porous material is seen to reduce the RMS along the boundary layer. However, very close to the wall, an increase is observed. According to the authors, could be due to the high frictional forces introduced. Overall, HWA measurements indicate a lower energy content in the boundary layer, meaning that noise generation at the TE can be reduced with porous materials.
Velocity profiles were also obtained in the wake. In general, porous material were

seen to reduce the velocities in the wake. The lower momentum of the wake leads to a higher velocity deficit in the near-wake region, which according to the authors is responsible for a decreased drag coefficient. The Reynolds stresses were generally lower than those observed for the solid case, except for the downstream region in which the delayed vortex is present. Indeed, in this region the flow has already recovered in the solid TE case, while with porous TE phenomena of vorticity are still occurring.
The velocity power spectra in the boundary layer highlighted a lower energy content of the boundary layer structures when porous materials are applied. The only exception is observed close to wall for the highly porous insert, because of wall friction. A strong tonal frequency peak indicated the presence of vortex shedding for the solid TE case. Highly porous materials are capable of cutting off the fundamental vortex shedding frequency. However, the presence of a *broadband hump* in the velocity power spectral density emerged for the highly porous material. According to the authors this could be due to

- the presence of a recirculation region inside the material
- frictional forces acting on the rough surface

Data on the energy-frequency content in the wake are also presented. In the solid case, the fundamental frequency and the relative harmonics of the vortex shedding are clearly seen in the solid-TE case. The low-porosity material also shows these peaks, which in some cases are seen to even protrude above the solid case ones. The highly porous material can instead suppress the tonal peaks and reduce the power density. The price to be paid is the emergence of the broadband hump as observed for the velocity power spectral density in the boundary layer of the plate. After an analysis of the phenomenon, the authors could conclude that the broadband hump observed with highly porous materials is due to a flow recirculation zone inside the porous TE.
Finally, a sensitivity analysis of the length of the porous section was performed. Trailing edges with different streamline lengths were tested. The results showed that if the porous TE is too short, no change in tonal behaviour can be observed and no broadband hump is present. Indeed, tonal peaks are suppressed only if the blunt TE is at least twice as long as its height. The authors state that the suppression of flow acceleration and delay of the wake are strongly linked to the amount of flow which is discharged in the wake from the porous material.
Overall, this article underlined the importance of using materials with high enough porosity consistently with [8]. This must be done to allow the flow penetration-discharge phenomenon.

Rubio et al. Rubio et al. [7] tested a NACA 0018 airfoil with solid and porous trailing edges with 89.3 % and 91.7 % porosity metal foams were chosen to manufacture porous TE inserts which covered 20% of the total chord. The respective permeability was measured to be 6×10^{-10} m^2 and 2.7×10^{-9} m^2. Far-field noise measurements indicated a reduction of 6 dB. In the frequency domain, highest reduction of up to 10 dB are observed at low frequencies, while at high frequencies sound emission is higher. This is considered to be due to the higher wall friction which is introduced along with the porous materials, as observed by [9] for a 90.2% porosity material. Vertical velocities along the airfoil are generally increased when porous materials are used at the TE. As suggested by the authors, this aspect may be linked to the inner hydrodynamic field observed by Showkat Ali et al. [9]. The RMS values are reduced along the airfoil in almost all the boundary layer when a porous treatment is applied. The only exception was seen with the high porosity material close to the wall at the TE, due to skin friction. Here, turbulence intensity is even higher than the solid TE case. This is consistent with [9]. As mentioned above, a larger reductive effect was measured for the lower porosity material. The authors underline the fact that an increased turbulence close to the wall should (in theory) increase far-field noise. However, this is not observed as noise is generally lower when porous TEs are used. The explanation provided lies with another effect for noise reduction which is the lower acoustic impedance jump at the trailing edge which occurs with porous materials [4]. Next, an analysis of the Reynolds shear stress $-\overline{u'v'}$ showed that this parameter is generally reduced by porous material. This aspect tells that permeable treatments reduce the energy content of coherent turbulent structures. Also here, the lower permeability TE shows the highest reductions.

2.4.1.1 Comments

In this section, the main contributions from the papers are described and linked together.
The main aspect to highlight is that the effect of porous trailing edge on turbulence intensity is not clear yet. In [8] it increases turbulence intensity both in the wake and above the trailing edge. Conversely, in [7, 9] turbulence intensity is decreased at the trailing-edge in the boundary layer. Rubio et al. [7] suggest that this may indicate a dependence on the material as well as on the experimental set-up characteristics.

The review of the different articles highlighted the fact that it is not possible to determine an optimal porosity value for the material used. However, some considerations can be made:

- Porosity should be high enough to allow the penetration-discharge phenomenon
- Porosity higher than 90% is usually good to obtain noise reductions
- The higher the porosity of the materials, the more likely is the occurrence of increased turbulence close to the wall due to higher skin friction

Among the mechanisms which could be responsible for noise reduction, the following hypothesis were made

- At high frequencies, the corresponding small turbulent structures interact with the porous surface. The result is an energy dissipation into heat which was defined *hydrodynamic damping*. Furthermore, turbulence spectra are shifted towards lower frequencies when porous materials are applied. These factors are responsible for lowered trailing edge noise.
- Enhanced anisotropy of turbuent structures due to flow stretching in the streamwise direction and sweeping motions of high momentum fluid towards the wall reduce wall-normal velocity components. Thus, less pressure oscillations occur.
- The energy content of large coherent structures in the outer layer of the boundary layer is reduced by the porous materials. Hence, less low-frequency surface pressure flucutations occur. This could play role in the lowered trailing edge noise.

In [7,9], turbulence quantities measured on a solid airfoil are generally reduced by the porous materials. However, close to the porous wall, higher velocity fluctuations are observed. This aspect may be linked to flow discharge process described by [9]. With the addition that the classic no-slip condition is not valid on porous surfaces, the near-wall region could be very interesting for further research. An overview of literature regarding near-wall measurements is presented below.

2.4.2 Near-wall wind tunnel measurements

Near-wall proximity is known to be a problem for different flow measurement techniques. For instance, laser-Doppler velocimetry (LDA) and PIV face problems in the near-wall region due to the high velocity shear which affects the particle seeding. Furthermore for PIV, wall reflections are another common drawback which arises due to wall proximity. Hot-wire anemometry (HWA) presents high time and spatial resolution. Furthermore, its setup is simpler than PIV and it does not require an optical access like LDA or PIV. The main disadvantages are the need

for calibration, the impossibility to measure reverse flow and the fact that it is intrusive [20].
Wall-proximity is an issue for HWA as well. Generally, close to the wall the velocity measured with HWA will be higher than the effective. This is due to the heat conductivity of the wall material which generates additional heat flux which is detected by the hot wire. This is linked to the dependency of the calibration of the probe on the flow temperature. A decreasing trend for the thermal conductivity with regards to porosity can be generally observed for porous materials. With the highly porous materials recently in wind tunnel measurements [7,9], the thermal conductivity of the materials involved could be low enough to allow valid measurements with HWA. It is however important to pay great attention to the enhanced wall friction which is typical of porous materials [7], as well as the particularly high temperatures which can arise into the porous materials [15].
In HWA, the most common corrections to near-wall errors are [20]

- Correct voltage according to fluid temperature with fixed wire temperature
- Calibrate for different flow temperatures. Correct King's law coefficient according to flow temperature measured during acquisition
- Keep the overheat ratio[1] of the wire constant (manually or with sensor)

2.5 Research questions, aims and objectives

The research objective is to predict the effects of porous materials on the reduction of trailing-edge noise with computational aeroacoustics (CAA) simulations. The research questions with relative sub-questions are listed below.

1. Can CFD be used to describe flows through porous media?
   (a) Are the results consistent with published literature on experimental methods [7–9]?
   (b) Are the results consistent with the measurements taken with HWA?
2. What is the influence of the porous trailing edge on the airfoil flow if the results are compared to those obtained with a solid one?
   (a) How does the presence of a porous material influence the finite-volume formulation of the Navier-Stokes Equations?

[1]The overheat ratio is defined as $(R_w - R_0)/R_0$, where R_w is the wire resistance at its temperature T_w and R_0 is the wire resistance at the reference temperature T_0.

(b) How does the flow interact locally with the porous media? Can some information on turbulence be extracted?

Chapter 3

Numerical study: methodology

In this chapter, the numerical method used is described and its results are discussed. First, the inclusion of the penalization term in the solution procedure is treated.

3.1 Inclusion of porous treatments in the solution procedure

In this section, the main steps towards the solution of the flow field are treated individually. The starting point are the incompressible continuity and momentum equations (Eq. 3.1) for a porous material

$$\begin{aligned}
&\frac{\partial \phi\rho}{\partial t} + \nabla \cdot (\phi\rho\mathbf{u}) = 0 \\
&\frac{\partial \phi\rho\mathbf{u}}{\partial t} + \nabla \cdot (\phi\rho\mathbf{u}\mathbf{u}) = -\nabla\mathbf{p} + \nabla \cdot \boldsymbol{\tau} + \phi\rho\mathbf{f} - \underbrace{\mu\mathbf{K}^{-1}\phi\mathbf{u} - (\phi\rho)\phi^2\frac{C_F}{\sqrt{\mathbf{K}}}|\mathbf{u}|\mathbf{u} - \phi^3 C_{F,2}|\mathbf{u}|^2\mathbf{u}}_{Penalization}
\end{aligned} \tag{3.1}$$

Turbulence The next step is to consider turbulence. In the current work, the large eddy simulation turbulence model (LES) is used. Further considerations on this model are included in Section 3.2. The inclusion of the penalizaton term into the turbulence formulation was not considered for simplicity.

Coordinate transformation Because no divergence or derivative operators are present in the penalization term, the coordinate transformation from cartesian to curvilinear is not affected.
In the continuity equation,density is simply substituted with a new variable $\rho\phi$.

Integration over a control volume (finite volume method) In finite volume, the next step is to integrate the flow equations over a finite-volume cell. Focusing on the penalization term in the momentum equation, which has been multiplied by the Jacobian of the coordinate transformation J, we have that

$$\boxed{-\int \left[\mu K^{-1}\phi U + (\phi\rho)\phi^2 \frac{C_F}{\sqrt{K}}|\mathbf{U}|U + \phi^3 C_{F,2}|U|^2 U\right] J\,(d\mathrm{Vol}) = \mathcal{U}_1 + \mathcal{U}_2 + \mathcal{U}_3} \tag{3.2}$$

where

$$\begin{aligned}
\mathcal{U}_1 &= -\mu\phi K^{-1} \underbrace{J\Delta\xi\Delta\eta}_{=J_V} U_P^t \\
\mathcal{U}_2 &= -(\phi\rho)\phi^2 \frac{C_F}{\sqrt{K}} J_V \sqrt{U_P^{2,t} + V_P^{2,t}}\, U_P^t \\
\mathcal{U}_3 &= -\phi^3 C_{F,2} J_V \left(\sqrt{U_P^{2,t} + V_P^{2,t}}\right)^2 U_P^t
\end{aligned}$$

and

$$\boxed{-\int \left[\mu K^{-1}\phi V + (\phi\rho)\phi^2 \frac{C_F}{\sqrt{K}}|\mathbf{U}|V + \phi^3 C_{F,2}|V|^2 V\right] J\,(d\mathrm{Vol}) = \mathcal{V}_1 + \mathcal{V}_2 + \mathcal{V}_3} \tag{3.3}$$

with

$$\begin{aligned}
\mathcal{V}_1 &= -\mu\phi K^{-1} \underbrace{J\Delta\xi\Delta\eta}_{=J_V} V_P^t \\
\mathcal{V}_2 &= -(\phi\rho)\phi^2 \frac{C_F}{\sqrt{K}} J_V \sqrt{U_P^{2,t} + V_P^{2,t}}\, V_P^t \\
\mathcal{V}_3 &= -\phi^3 C_{F,2} J_V \left(\sqrt{U_P^{2,t} + V_P^{2,t}}\right)^2 V_P^t
\end{aligned}$$

J_V indicates the volume of the cell inspected, and ξ and η are curvilinear coordinates.
It is chosen to consider the Forchheimer and the Darcy terms explicitly. This means that their value at the new time level $n+1$ is only a function of known data at previous time iterations.
In this way, both these contributions can be added to the canonic finite volume equation (3.4) as source terms.

$$A_P U_P^{t+\Delta t} + A_W U_W^{t+\Delta t} + A_E U_E^{t+\Delta t} + A_S U_S^{t+\Delta t} + A_N U_N^{t+\Delta t} = S_U + S_{U,\text{penalization}} \tag{3.4}$$

The source term from the penalization terms is defined in Equation 3.5.

$$S_{U,\text{penalization}} = -\phi J_V U_P^t \left[\mu K^{-1} + \rho \phi^2 \frac{C_F}{\sqrt{K}} \sqrt{U_P^{2,t} + V_P^{2,t}} + \phi^2 C_{F,2} \left(\sqrt{U_P^{2,t} + V_P^{2,t}} \right)^2 \right] \tag{3.5}$$

with the approximation that ϕ and K can be considered uniform and thus constant. This is not the case in real conditions, with both values being functions of space and time.

SIMPLE algorithm At this point, the Rhie-Chow interpolation can be applied and the procedure described in Section 2.3.2.1 can be followed normally.
It is important to underline that the procedure presented can be applied to all the cells of a mesh provided that, for a non-porous cell, K assumes a very high value, and ϕ is equal to 1. On the other side, porosity and permeability shall assume the desired input value when a cell is porous. In this way the penalization term is negligible in normal flow conditions, while it is effective in the porous region.

3.1.1 Implementation in CFD software EllipSys2D

`EllipSys2D` is a general purpose Navier-Stokes code based on a second-order multi-block finite volume method. It has been developed at Risø National Laboratory and at the Department of Fluid Mechanics at the Technical University of Denmark. In the current work, the original scripts were modified to account for the presence of a porous treatment at the trailing-edge.
The *InitializeFlow* subroutine was modified so that density in the porous material could be expressed as the product of porosity and density of an homogenized porous domain [15]. The porous field is defined by porosity ϕ and permeability K, which are provided as an input to `EllipSys2D`. The possibility to simulate a spatial distribution of permeability was implemented by allowing different values of porosity at the cell nodes inside the trailing edge.
The penalization drag is added on the right hand side of the momentum equation as an additional source term. The source terms are finally:

$$\begin{aligned} S_U(i,j) = S(i,j) &- \mu\, \phi\, K^{-1}\, J_V U(i,j) \\ &- \rho \phi^3 C_F K^{-0.5} J_V \sqrt{U_P^{2,t} + V_P^{2,t}}\, U_P^t - \phi^3 C_{F,2} J_V \left(\sqrt{U_P^{2,t} + V_P^{2,t}} \right)^2 U_P^t \end{aligned}$$

$$S_V(i,j) = S(i,j) - \underbrace{\mu\,\phi\,K^{-1}\,J_V V(i,j)}_{\text{Darcy term}} - \underbrace{\rho\phi^3 C_F K^{-0.5} J_V \sqrt{U_P^{2,t} + V_P^{2,t}}\, V_P^t - \phi^3 C_{F,2} J_V \left(\sqrt{U_P^{2,t} + V_P^{2,t}}\right)^2 V_P^t}_{\text{Forchheimer term}}$$

3.1.1.1 Forchheimer coefficient

The Forchheimer coefficient C_F is a crucial parameter which affects the results of the simulations significantly. Many relationships between C_F and permeability and porosity have been proposed in the last century, mainly from research on oil and gas.
In the current study, it was decided to adopt the empirical relation found by Thauvin and Mohanty for high-velocity gas flows through porous media [21]. According to this formulation, C_F is expressed as a function of porosity as

$$C_F = 0.993 a b^{-1/2} \phi^{-3/2} [-]$$

with $a = 1.75$ varying between and $b = 150$. The first multiplying constant is needed to ensure units coherence [1]. This relationship was chosen because it provided values of C_F which are consistent with experiments of the same kind in literature [7].
The evaluation of the cubic term $C_{F,2}$ was made according to literature [17]. However, it was observed that the influence of this term gets less relevant with a high permeability. Eventually, given the values in [17] it was decided to set $C_{F,2}$ to 0.008 by fitting a power decay of this parameter with the permeability. Overall, the influence of the cubic term is negligible.

3.1.1.2 Non-dimensional numbers

Different non-dimensional numbers can be useful for validating the code. The most relevant ones are listed below.

- *Reynolds number* $\mathrm{Re} = \frac{L^* U_\infty}{\nu}$ with L^* characteristic length, U_∞ free-stream velocity and ν kinematic viscosity.
  This parameter allowed to replicate the same conditions of reference wind tunnel experiments in terms of model size and free stream velocity.
- *Coefficient of permeability* $K_{\mathrm{ND}} = \frac{K\phi U_\infty}{\nu h}$, where h is the height of the porous domain inspected. This coefficient was used to replicate the same characteristics of the porous materials used in the reference experiments.

[1] The original formulation from Thauvin and Mohanty requires the permeability to be expressed in Darcy (d). In the current work $1\mathrm{m}^2 = 1013250273830.9$ d

- *Pore-size Reynolds number* $Re_p = \frac{\delta U_\infty}{\nu}$ where δ indicates the average pore size. This parameter is very important, as it determines the nature of the penalization term. Darcy law is reliable for $Re_p < 1$. When $Re_p > 10$, it is necessary to include a quadratic contribution in the penalization term (Forchheimer equation). In the cases inspected and cited in this document, usually $Re_p >> 10$.

3.1.1.3 Boundary layer parameters

As mentioned in the literature review, the study of boundary layers is an important element in aerodynamics. The main parameters to analyse different boundary layers and study transition phenomena are presented below:

- Displacement thickness δ^*, defined as the mass flux defect between the viscous velocity profile inside the boundary layer and the inviscid profile outside.

$$\delta^* = \int_0^\infty \left(1 - \frac{\rho U(y)}{\rho_\infty U_\infty}\right) dy$$

- Momentum thickness θ, defined as the momentum defect caused by the boundary layer.

$$\theta = \int_0^\infty \frac{\rho U(y)}{\rho_\infty U_\infty} \left(1 - \frac{U(y)}{U_\infty}\right) dy$$

- Thickness δ_{99}, defined as $U(\delta_{99}) = 0.99 U_\infty$.

- Shape factor, defined as the ratio between the boundary layer displacement thickness and momentum thickness. The value of H increases with the adverse pressure gradient of the flow. H is seen to decrease during transition phenomena.

$$H = \frac{\delta^*}{\theta}$$

3.2 Turbulence model: large eddy simulation

The turbulence model used in the current work is a large eddy simulation model (LES). LES is one of the advanced model in turbulence. It is based on the fact that large turbulent eddies are the ones carrying more energy in a turbulent flow. For this reason, they need to be resolved accurately. On the opposite, most of the energy dissipation occurs at large wave numbers (i.e. high frequencies), which are typical of small eddies. The small eddies can therefore be modelled and do not need to be numerically resolved. A sketch to explain this is presented in Figure 3.1.

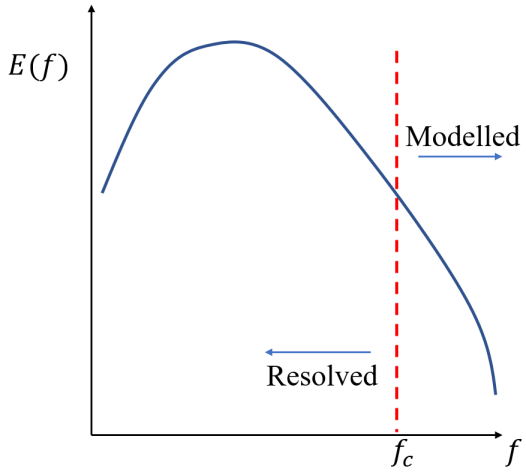

Figure 3.1: Sketch of a typical energy density spectrum of a turbulent signal, as a function of frequency. In LES only the low frequency, large eddies are resolved, while the small, high frequency ones are modelled. In the mixed scale model applied in this study, the cut-off frequency f_c depends on the mesh refinement.

For the reasons mentioned above, LES is less numerically more expensive than a direct numerical simulation (DNS), in which the smallest scales up to the Kolmogoroff length scale must be directly resolved and are the most numerically expensive. Compared to the Reynolds Averaged Navier-Stokes (RANS) method, LES is more expensive because the large eddies are directly solved, however it is also more accurate.
The LES procedure is based on a spatial averaged version of the Navier-Stokes equations, obtained with a spatial filtering procedure. In this way, large-scale turbulent motions and small-scale turbulent motions are separated. The large-scales are numerically solved, while the smallest eddies are modelled. The choice of the size of the averaging window must be made wisely and depends on the mesh refinement.
As a consequence of the filters in LES, subgrid-scale models are required to model the unresolved scales of turbulence. Mathematically this is made necessary by the introduction of a *residual-stress tensor* τ_0 in the filtering process, which requires closure.
In the current work, the residual-stress tensor is modelled via an *eddy viscosity* ν_t with the *mixed-scale turbulence model* described by Sagaut in [22] and applied to CAA by Shen et al. in [23].

The mixed-scale model is based on subgrid scales. The mixed scale model deduces subgrid information from the resolved scale by extrapolation in the fre-

quency domain. This model is more elaborated and reliable than other models which are entirely based on the resolved scales, such as the Smagorinsky model. On the other hand, it is less sophisticated than models which feature additional evolution equations.

The mixed-scale model requires the use of two spatial filters. The first filter is defined on the finest mesh available. The second filter is usually referred to as *test filter*. Usually it is twice as coarse as the first filter [23]. A sketch presenting a usual turbulence spectrum with the filters for the mixed-scale subgrid model is showed in Figure 3.2.

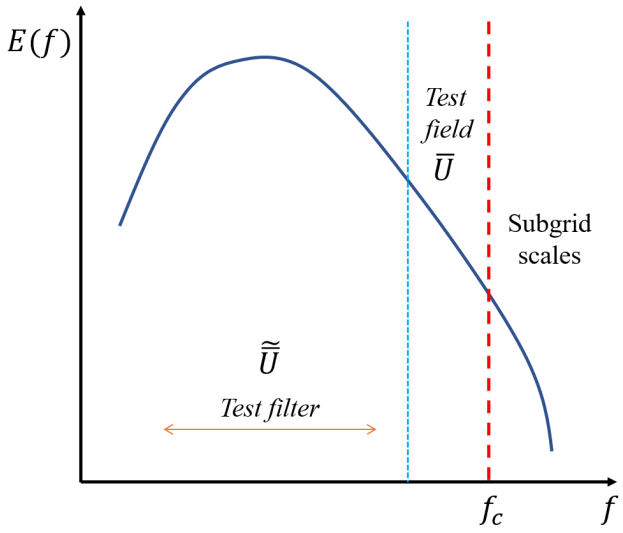

Figure 3.2: Sketch of a typical energy density spectrum of a turbulent signal, as a function of frequency. Filter regions for the mixed-scale subgrid model are indicated. The cut-off frequency f_c determines the size of the eddies to be modelled.

A short description of the mixed scale model is included next. The filtered Navier-Stokes equation in space are expressed as

$$\frac{\partial \overline{U}_i}{\partial t} + \frac{\partial \overline{U}_i \overline{U}_j}{\partial x_j} = -\frac{1}{\rho}\frac{\partial \overline{P}}{\partial x_i} + \nu \frac{\partial^2 \overline{U}_i}{\partial x_j^2} + \frac{\partial \tau_{0,ij}}{\partial x_j} \tag{3.6}$$

$$\frac{\partial \overline{U}_i}{\partial x_i} = 0 \tag{3.7}$$

where the overbar indicates spatial averaging with the first filter. The residual-stress tensor τ_0 is expressed as

$$\tau_{0,ij} = \overline{U}_i \overline{U}_j - \overline{U_i U_j} \tag{3.8}$$

With the introduction of the residual term τ, the system of Equations 3.6 and 3.8 is not closed. To achieve closure, the subgrid-scale turbulent stresses τ_0 must be modelled. By intoducing the eddy viscosity ν_t, τ_0 can be expressed as

$$\tau_{0,ij} = \nu_t \left(\frac{\partial \overline{U}_i}{\partial x_j} + \frac{\partial \overline{U}_j}{\partial x_i} \right) - \frac{2}{3} k \delta_{ij} \tag{3.9}$$

with k being the turbulent kinetic energy of the subgrid scales.
The second filter for spatial averaging comes into play when computing the kinetic energy. The kinetic energy of the subgrid scales is defined for the velocity fluctuation U' as

$$k_{sgs} = \frac{1}{2}(U'U') \tag{3.10}$$

The velocity fluctuations of the eddies lying in the subgrid region are however unknown. Therefore, k_{sgs} is usually computed by assuming similarity between the grid levels available. This means that the kinetic energy of the subgrid scales k_{sgs} is approximated with the kinetic energy at the cut-off frequency k_c. k_c can be evaluated from the resolved velocity components.

$$k_c \approx k_{sgs} \tag{3.11}$$

Explicitly,

$$k_{sgs} = \frac{1}{2} \sum_{j=1}^{2} (U_j - \overline{U}_j)^2 \approx \frac{1}{2} \sum_{j=1}^{2} (\overline{U}_j - \widetilde{\overline{U}}_j)^2 = k_c \tag{3.12}$$

where $\widetilde{\overline{U}_j}$ represents the velocity obtained with a double filtering in space.

Finally, the eddy viscosity is determined with the mixed-scale turbulence model as

$$\nu_t = C_0 |\overline{\omega}|^{\alpha} k^{(1-\alpha)/2} \Delta^{(1+\alpha)} \tag{3.13}$$

where α is a parameter between 0 and 1, ω is vorticity and C_0 is a constant. Δ is an averaged cell size (of dimensions Δ_x, Δ_y) defined in 2D as

$$\Delta = \sqrt{\Delta_x \Delta_y} \tag{3.14}$$

An upper limit on Δ translates on a limited aspect ratio of the mesh cells. This is trated in Section 3.3.1.

It is interesting to notice that with this method, the eddy viscosity is a function of the turbulent kinetic energy k. This means that close to the wall, ν_t tends to zero. Hence, no wall model is required. The main constraint is that $y+$ must be

limited below 10 to ensure to capture the viscous sublayer, ensuring that $k \to 0$ towards the wall.

In this way, the mixed-scale model is different from vorticity based methods, for which wall-models are required.
Usually [23] - as well as in this thesis work - $\alpha = 0.5$ and $C_0 = 0.02$. The eddy viscosity in Equation 3.13 can therefore be expressed as

$$\nu_t = 0.02|\overline{\omega}|^{1/2} k^{1/4} \Delta^{3/2} \tag{3.15}$$

3.2.1 LES in 2D simulations

2D simulations are approximations of real phenomena, which are normally driven by 3D effects. Using 2D simulations to describe 3D phenomena can often be misleading.
LES is usually applied to three-dimensional flows. Nevertheless, two-dimensional turbulence has very different dynamics than three-dimensional turbulence. One of the reasons for this, is that the vortex stretching phenomenon, typical of three-dimensional flows, is not present in the two-dimensional case [24].

Furthermore, two-dimensional turbulence can exhibit two inertial ranges. The first one is the usual energy transfer, known as the *-5/3 law*, which acts also in three-dimensional flows. The second one is a strong backward energy cascade from the small scales to the large scales of turbulence [22].

The main consequence of these considerations is that, generally, 2D flows feature much stronger vortices than 3D, and turbulence mechanisms are very different.

Therefore, depending on the case studied, two-dimensional simulations can perform poorly in describing phenomena which are generally dominated by three-dimensional effects. Hence, the results from the current work must be carefully and critically interpreted. Discrepancies with experimental results are expected.

3.3 Mesh

The spatial discretization of the domain is decisive to obtain correct results. In this section, the main requirements are presented.

In `EllipSys2D`, attributes must be given to each cell to allow the solver to distinguish solid surfaces and porous media from other flow conditions. A description of these attributes is presented in Table 3.1.

Table 3.1: Mesh attributes for `EllipSys2D`.

Name	Range/Value	Definition
Exterior	0	Vertex outside block
Interior	1	Normal interior vertex
Porous	50-59	Porous material 1
Porous	60-69	Porous material 2
Wall	101	Wall (no-slip, adiabatic, impermeable)
Inlet	201	Constant value inlet
Farfield	301	Farfield (U=constant + circulation)
Outlet	401	Outlet (non-valued)

3.3.1 Main criteria and constraints

Rules and requirements were adopted and rigorously applied in the mesh procedure to ensure a correct discretization. These criteria are listed below.

- **Aspect ratio** The aspect ratio of the cells in the uniform mesh area must lower than 5. This is to ensure a low average cell size Δ in the computation of the eddy viscosity in the LES turbulence model. Cells with very high aspect ratios would not allow the development of turbulent structures, with high dissipation from ν_t. This is deepened in Section 3.2. A visual example of cells with different aspect ratios is provided in Figure 3.3.

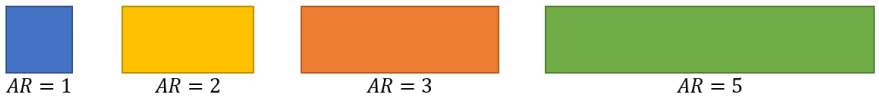

Figure 3.3: Examples of cells with different aspect ratios.

- **Boundary-layer discretization** The height of the first cells next to the wall must be set to properly describe the turbulent structures in the boundary layer. It is very important to determine this parameter well, as a too conservative guess would harm the computational costs by increasing the number of cells. Moreover, in LES, the mesh refinement determines the cut-off frequency after which turbulence is modelled. Hence, the size of the cells must be small enough to capture the events responsible for turbulence production and flow instabilities, such as perturbations.
  In CFD, the discretization of the boundary layer is usually made according

to the non-dimensional wall coordinate y^+. This parameter is defined in turbulence theory as

$$y^+ = \frac{yU_f}{\nu} \tag{3.16}$$

where ν is the kinematic viscosity and U_f is the *friction velocity*, defined as

$$U_f = \sqrt{\frac{\tau_0}{\rho}} \tag{3.17}$$

where τ_0 is the wall shear stress [25].
According to steady boundary layers theory, at values of y^+ higher than 70 and lower than 500, the mean horizontal velocity $\overline{u}$ of a boundary layer flow is linked to the vertical coordinate y by the *logarithmic law*, which is presented in Equation 3.18.

$$\overline{u} = A\,U_f \ln(y) + B_1 \tag{3.18}$$

Equation 3.18 can also be expressed in terms of *law of the wall*, as

$$\overline{u} = U_f(A\ln(y^+) + B) \tag{3.19}$$

The portion of boundary layer in which this law is valid is called *logarithmic layer*. Experiments in boundary layer flows over walls allowed to find that

$$A = 2.5\,[-] \qquad B = 5.1\,[-]$$

with A a universal constant [25].
This aspect was used to determine the friction velocity U_f to be applied in Equation 3.16, together with boundary layer results of a previous simulation. An example is provided in Figure 3.4. This figure shows the velocity profile against the natural logarithm of the vertical coordinate y of the flow over a flat plate. The results are extracted from a flat plate flow case at $x/c = 0.8$ [-], with a free stream velocity of 7 m/s. In Figure 3.4, the logarithmic correlation is well visible and it is marked in red with a linear fit.
The criterium imposed for the height of the first cells is that $5 < y^+ < 10$ for the cell-center of the first mesh element next to the solid wall of the model. This means that the height of the first cell lies at $10 < y^+ < 20$. The other dimension of the cell x^+ is then obtained from the constraint on the aspect ratio discussed earlier (i.e. $x^+ = xU_f/\nu < 50$). Normally, at least 30 mesh points in the boundary layer are needed to obtain reliable results with LES [22].

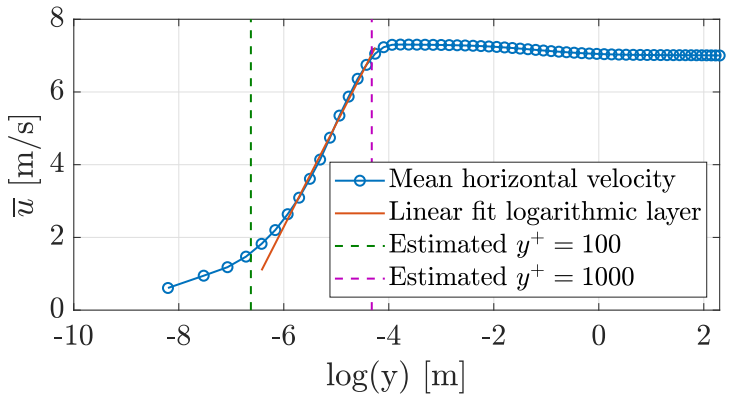

Figure 3.4: Average velocity profile at $x/c = 0.75$ from a simulation on a flat plate with timestep $\Delta t = 8 \times 10^{-5} s$. On the x axis, the natural logarithm of the vertical coordinate y is plotted. A fit of the points in the logarithmic layer is showed in red. The approximate boundaries of the logarithmic layer are marked with vertical dashed lines.

- **Wall orthogonality** The walls of the cells adjacent to the solid wall must be perpendicular to the wall perimeter. This is important to ensure that the non-slip boundary condition is correctly applied. In the code to generate the mesh, the definition of scalar product was applied to ensure wall orthogonality. The procedure is derived in Appendix A.

- **Mesh expansion** A smooth transition between mesh regions must be ensured. In order to evaluate this quality indicator, the *mesh expansion* is defined as the ratio between the dimensions of two adjacent cells. The expansion is limited to a maximum value of 10%. This is achieved with stretching functions such as hyperbolic and trigonometric functions.

- **Dimensions of the domain** The domain must be wide enough to allow free-stream conditions at the domain boundaries. For this reason, its dimensions were set to approximately 30 chords in the streamwise direction and 20 chords in the orthogonal direction.

3.3.2 Code for mesh generation

The meshes used in this thesis work are obtained with MATLAB. Meshes are built in blocks, following `EllipSys2D` multiblock solution method. The first step in the code is to build the solid object. The number of points on the perimeter determine the number of cells on the walls. The hyperbolic tangent function is used to stretch

the grid. The hyperbolic tangent is defined as

$$tanh(x) = \frac{e^x - e^{-x}}{e^x + e^{-x}}$$

This function was chosen as it provides a mild expansion below 10%, provided that it is finely sampled. The stretching function is plotted in Figure 3.5a.

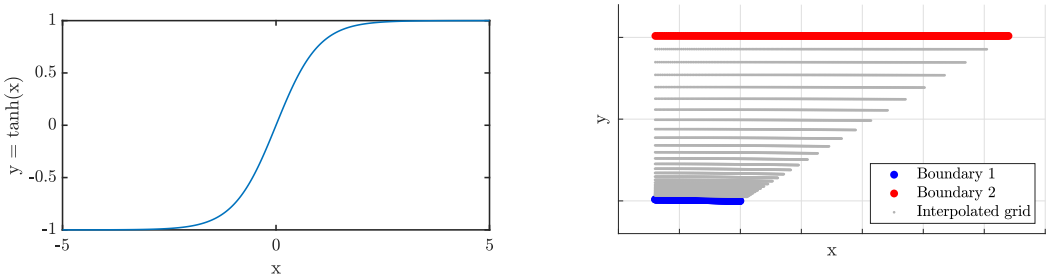

(a) Stretching function used for the mesh.

(b) Grid by interpolation between two boundaries.

Figure 3.5: Visual representation of topics in mesh generation.

Generally, the grid was generated by linear interpolation between two opposite walls, using the hyperbolic tangent for stretching. An example of this is presented in Figure 3.5b. Here, the blue points indicate the wall of the model, while the red dots are the boundary of the domain. The grey dots have been obtained via interpolation, by assigning two arbitrary values to the boundary walls, and using the values in between (generated with stretching functions) to define the grid points. The points generated were saved block by block in a mesh file `.x2d` following the right hand rule. The main script for mesh generation is included in Appendix B.

3.4 Input values

The choice of the parameters used as inputs to the simulation is essential to obtain accurate results efficiently. In this section the main inputs are briefly discussed. Figure 2.6 can be used as reference for terminology.

3.4.1 Timestep

The timestep is evaluated by limiting the amount of flow which is met by the smallest cell in the mesh within a timestep. For this criterium, the *Courant number*

C can be useful. It is defined as

$$C = \frac{u\Delta t}{\Delta x} \tag{3.20}$$

According to the Courant-Friedrichs-Lewy condition, C must be well below 1 for an explicit solver to be stable. As the solver used in this work is implicit, it allows to tolerate higher values of C. As a rule of thumb, C was kept below 15 to ensure convergence.

3.4.2 Sub-iterations

As discussed in Section 2.3.2.1, in the SIMPLE method a loop between velocity and pressure is needed to satisfy both the momentum and the continuity equations. Every cycle velocity-pressure is referred to as a *sub-iteration*. The number of sub-iterations was chosen to ensure a reduction of the residual of the pressure correction equation (Eq. 3.21) by at least one orders of magnitude.

$$A_P P_P^C + \sum A_{nb} P_{nb}^C = S_{mass} \tag{3.21}$$

The residual is defined as the imbalance in an equation solved iteratively due to the approximate solution P_P^{C*}. This is showed in Equation 3.22

$$\text{residual} = \sum_{cells} S_{mass} - A_P P_P^{C*} - \sum A_{nb} P_{nb}^C \tag{3.22}$$

3.4.3 Inner iterations for pressure correction equation

Within one sub-iteration of a time-step, iterations are needed to solve the pressure correction equation. In the same way as described above, the number of inner iterations for the pressure is determined in order to enforce a reduction of the residual by at least one order of magnitude.

3.4.4 Relaxation parameters for pressure and velocity

The relaxation parameters are chosen to optimize convergence efficiency. Their value is chosen to achieve numerical stability and improve efficiency by reducing the computational cost. Usual relaxation parameters for velocity are $\alpha_U = 0.9$ and for pressure $\alpha_p = 0.1$.

Chapter 4

Numerical study: a test case on a flat plate

The purpose of this chapter is to inspect the validity of the code described in Chapter 3.
A rectangular flat plate with an elliptic leading edge and a porous insert at the trailing edge was chosen as validation study. The experiment carried by Showkat Ali et al. in [9] was taken as reference to validate the code. To replicate this measurement campaign, a $0.05c$ thick plate was modelled with a porous trailing edge extending for $0.15c$. In the numerical case, the chord length was set to one. This means that to match the Reynolds number of 460,000 of [9], velocity was set to $U_\infty = 7$ m/s and the kinematic viscosity to $\nu = 1.5 \times 10^{-5}$ m^2/s. The coordinate systems are showed in Figure 4.1.

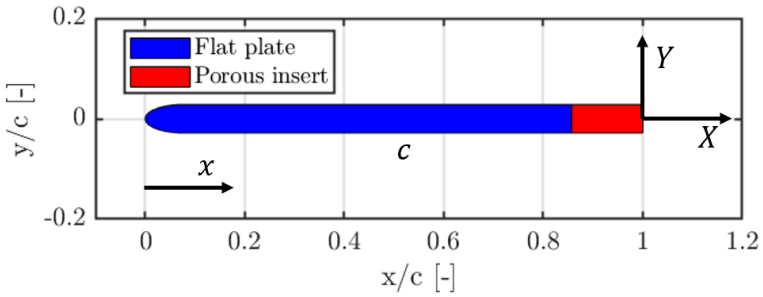

Figure 4.1: Flat plate with a 15% porous trailing edge and 5% thickness. The coordinate systems are displayed.

The plate has a chordlength c and a height at the trailing edge equal to h. The x and X axes are defined positive from leading edge towards trailing edge. The

origin of the x axis is defined at the leading edge. The origin of the X and the Y axes is defined at the trailing edge as showed in Figure 4.1.

The flow on the plate was simulated at a zero angle of attack with `EllipSys2D` for both the fully solid trailing-edge and the porous trailing-edge. Table 4.1 includes the main inputs used. The foam properties (i.e. K and ϕ) have been chosen to match wind tunnel measurements by Showkat Ali et al. [9]. The non-dimensional coefficient of permeability K_{ND} defined in Section 3.1.1.2 was used to determine K.

Table 4.1: Review of main parameters used in the simulation of the flat plate. The parameters which are the same for solid and porous cases are typed in just once.

Parameter	Solid trailing edge	Porous trailing edge
Chord-based Reynolds number	460,000	
Timestep Δt	0.0002 s	
Total time for averaging	4-8 s	4-6 s
Relaxation pressure α_p	0.1 [-]	
Relaxation velocity α_u	0.9 [-]	
Constant C_0 LES	0.04 [-]	
Constant α LES	0.5 [-]	
Sub-iterations	32	
Kinematic viscosity ν	1.5×10^{-5} m^2/s	
Porosity ϕ	1	0.9
Permeability K	1×10^{20} m^2	5×10^{-7} m^2
x-location porous trailing edge	-	$[0.857c,\ c]$
Angle of attack	0°	
Mesh blocks 64×64	40	36

4.1 Mesh

An orthogonal, cartesian mesh was chosen to discretize the domain around the flat plate. Although it would have been desirable to include tape strips to force the transition to turbulent flow, it was decided to neglect this because of increased mesh complexities and computational cost.

The main approach to write the mesh has been to divide the domain into different regions, each of which divided into blocks of 64×64 cells. Figure 4.2 shows the different regions, which are marked by different colors. Three regions are used to describe the wake, while just one is dedicated to the leading edge. In the porous case, three additional regions are added between plate and wake to mesh the trailing edge.

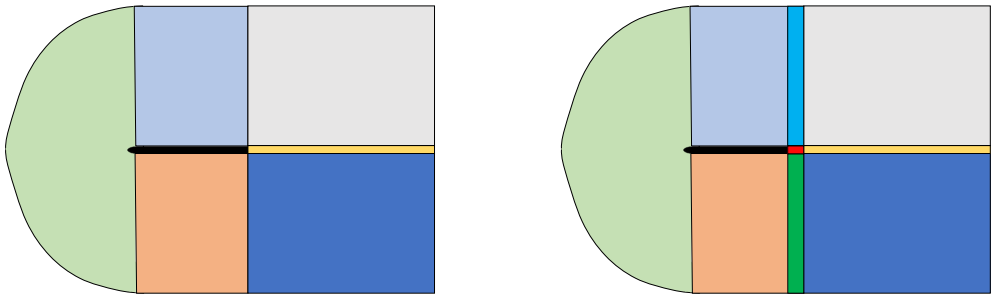

(a) Solid case. **(b)** Porous case.

Figure 4.2: Mesh strategy. Regions highlighted with different colors according to the regions they were assigned to in the mesh generation process.

A visualization of the final results for the fully solid and partially porous plates are presented respectively in Figures 4.3 and 4.4, with a zoom of the trailing edge region in Figures (b). Different attributes previously listed in Table 3.1 are marked with different colours.

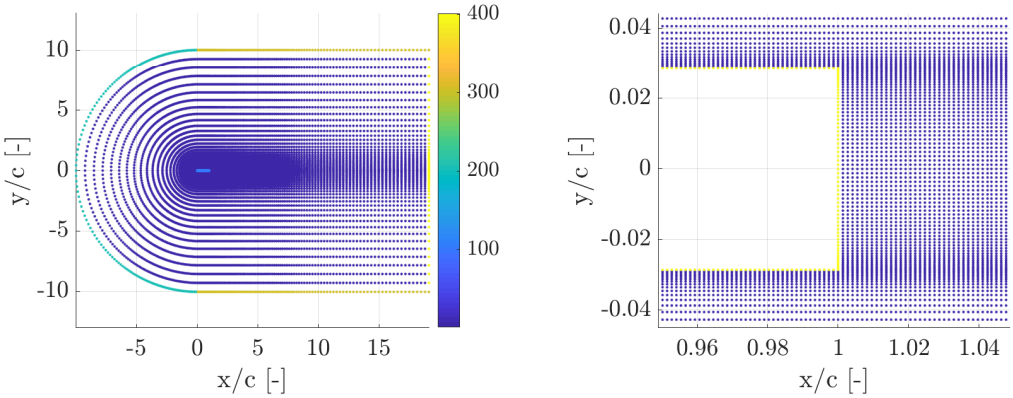

(a) Flat plate. **(b)** Zoom of the trailing edge.

Figure 4.3: Orthogonal mesh for a 5% thick flat plate with an elliptic nose. This mesh is made of 40 blocks of 64×64 cells. The domain boundaries are marked with different colors to distinguish inlet, farfield and outlet. The wall where non-slip condition are applied is light blue.

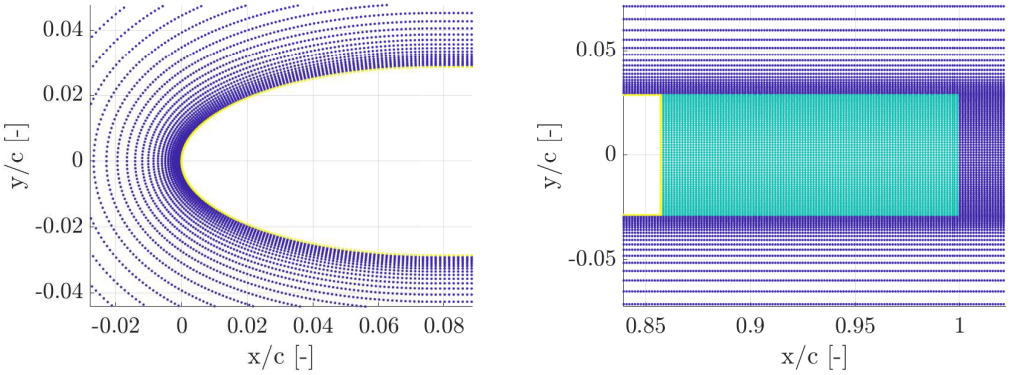

(a) Zoom of the leading edge.

(b) Zoom of the trailing-edge.

Figure 4.4: Orthogonal mesh for a 5% thick flat plate with an elliptic nose and porous trailing edge at 15% of the chord. This mesh is made of 36 blocks of 64×64 cells. The porous material is marked with green points. The penalization method is applied in this region.

4.1.1 Sensitivity study

The influence of the mesh on the results has been studied with a sensitivity analysis. The finest mesh was made according to the limitation on wall cells height (y^+) and aspect ratio (Section 3.3.1). In the solid case, the mesh is made of 40 blocks of 64×64 cells, for a total of 163,840 mesh points. In the porous case, the mesh was changed. Specifically, the central block in the wake was shifted more upstream to discretize the porous trailing edge. Figure E.1124carnevale4.2 allows to see this well. This aspect meant that in order to have the same mesh structure of the solid case, the number of blocks adjacent to the horizontal walls of the plate had to be reduced. For this reason, the total amount of blocks is lower than the solid case and equal to 36. The total number of mesh points in this case is 147,456 [1].

These two meshes were compared to coarser versions, for which one point was periodically skipped, leading to blocks of 32×32 mesh points instead of 64×64. This is a feature available in `EllipSys2D` and normally used to improve convergence of steady simulations.

[1] The mesh in the wake of the porous case could have been refined to match the solid case. This was not done because it would have implied to end up with an odd number of blocks, which could not be divided optimally between a finite number of processors and nodes available in DTU cluster.

Table 4.2: Mesh sensitivity study.

	Coarse		Fine (final)	
	Solid	Porous	Solid	Porous
Blocks	40	36	40	36
Block size	32×32	32×32	64 × 64	64 × 64
Mesh points	40,960	36,864	163,840	147,456
Height of wall cells	5.3×10^{-4} c	5.3×10^{-4} c	2.6×10^{-4}	2.6×10^{-4}
Wall cells center height	2.6×10^{-4} c	2.6×10^{-4} c	1.3×10^{-4} c	1.3×10^{-4} c
C_D [-]	0.074	0.024	0.077	0.022

Table 4.2 shows the drag coefficient results obtained with the two grids. The results does not vary significantly, meaning that a further refinement should not be necessary in this case. However, it is important to underline that the boundary layer discretization applied in this case is not sufficient to capture transitional phenomena in turbulence with LES. This mistake was noticed only at a later stage.

4.2 Results

4.2.1 Numerical stability and convergence

Numerical stability and convergence of the simulations were checked using residuals. Specifically, those computed after each iteration from the solution of the pressure equation in the SIMPLE method. In the current work, it was decided to truncate the computation after a specific number of sub-iterations, with the target of reducing the residuals by at least one order of magnitude.
In the computations presented here, residuals are lowered at each timestep to an absolute value below 10^{-5}. Their trend is considered to satisfy the convergence criteria described in Section 3.4.2. Residuals are plot extensively in Appendix C.

4.2.2 Mean flow field

The mean flow field is presented and discussed in this section. The mean field for the solid insert case was obtained by averaging over 4 seconds, between 4 seconds and 8 seconds into the simulation. The porous case was instead averaged over 2 seconds, from 4 seconds to 6 seconds. The higher averaging time was adopted in the solid insert case to allow for convergence of the mean, given the strong vortex shedding phenomenon typical of this case.
Figure 4.5 presents the pressure coefficient distribution along the upper side of the

flat plate. The bottom side is equivalent. The pressure coefficient is defined and computed as

$$C_p = \frac{p - p_\infty}{0.5\rho U_\infty^2} \qquad [-] \tag{4.1}$$

In Figure 4.5, the results for the solid and porous cases are compared with XFoil. The geometry implemented in XFoil was slightly modified by removing the vertex point at the trailing edge. This was done to reduce the 90 degrees angle at the trailing-edge. This was required to achieve convergence, as low panel node angles improve numerical stability on XFoil.

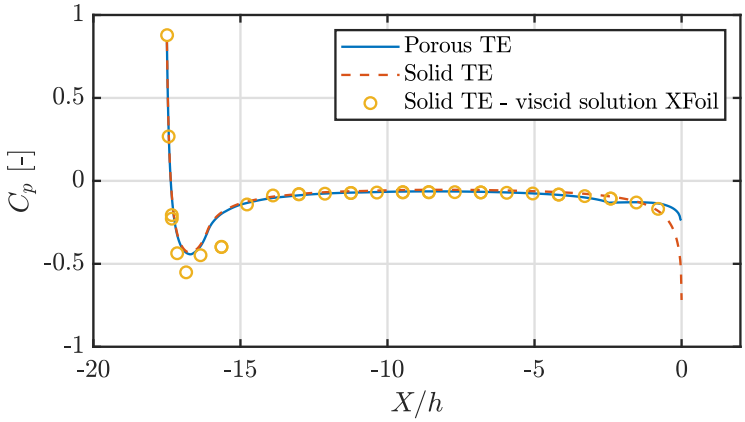

Figure 4.5: Pressure coefficient distribution along the plate. Profiles from the solid and porous case, compared with results from XFoil at the same Reynolds number. In the solution from XFoil, Ncrit is set to 9 and turbulence transition is not forced.

Both simulations show good agreement with XFoil. Results from CFD underestimate the pressure coefficient at the leading edge. The discontinuity in the porous case occurs at $X/h = -2.5$ and indicates the presence of the porous trailing edge. It can be seen that the porous solution starts to diverge from the solid one at $X/h = -5$. Moving towards the trailing edge, the porous insert varies the profile of C_p. Specifically, a milder pressure discontinuity at the trailing edge can be observed.
The mean fields of velocity and pressure are plot in Figure 4.6.

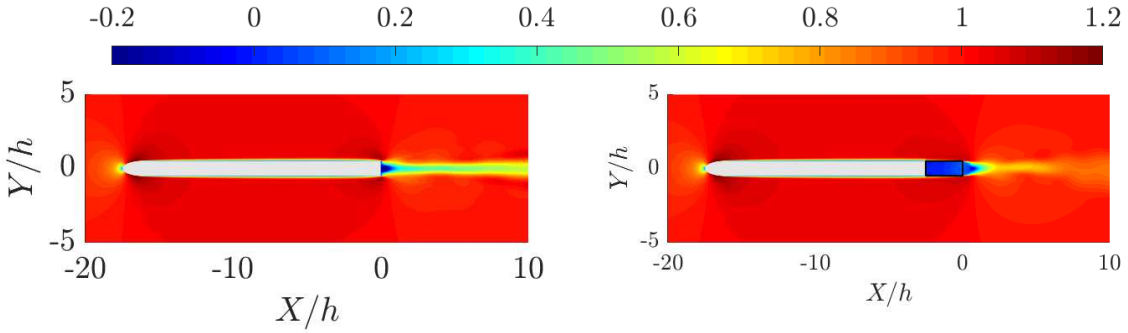

(a) Mean horizontal velocity field non-dimensionalised with U_∞.

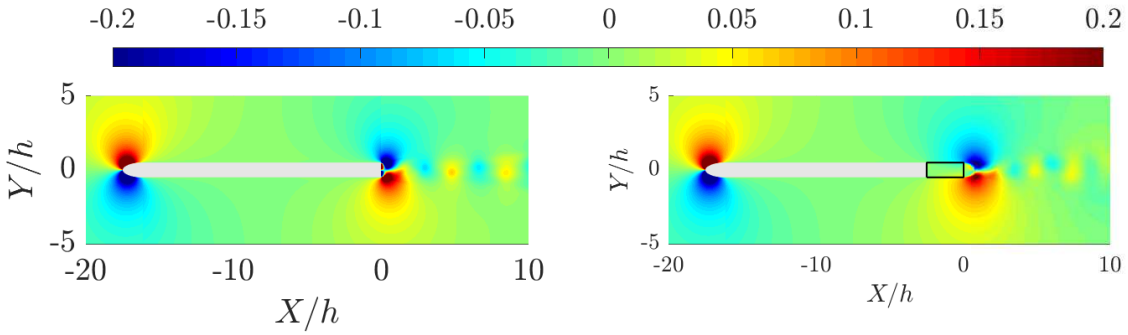

(b) Mean vertical velocity field non-dimensionalised with U_∞.

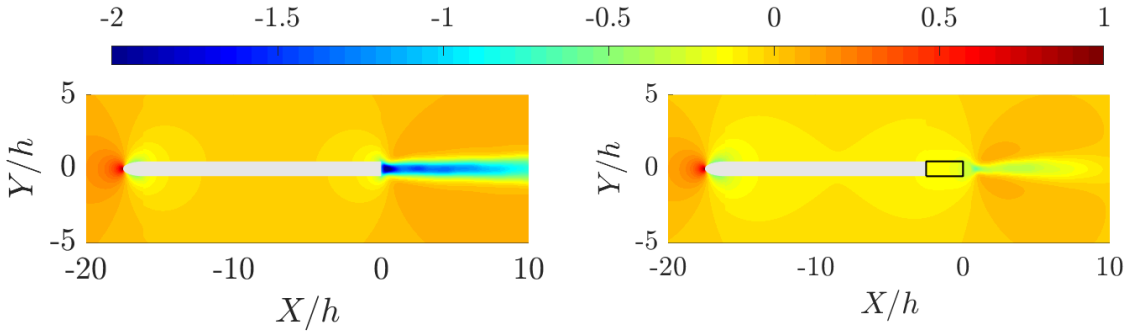

(c) Mean pressure field non-dimensionalised with the maximum field value.

Figure 4.6: Mean fields of horizontal and vertical velocity and pressure for a flat plate with a solid (left) and a porous (right) trailing edge. The velocities are non-dimensionalised with the free-stream velocity. Reynolds number of 460,000.

Figure 4.6c confirms the milder pressure gradient at the trailing edge due to the introduction of a porous insert at the trailing edge. On the other hand, pressure is generally lower along the plate when the porous insert is applied.
The porous trailing edge reduces the horizontal velocity defect with a faster wake recovery. Furthermore, in the porous case the magnitude of vortex shedding is highly reduced.
Compared to Showkat Ali, the results from CFD seem to intensify the effects of the porous media measured in the wind tunnel. The reason for this, could be the higher vortex strength of 2D simulations. Figure 4.6a allows to see a very strong wake deficit in the solid case, which could be due to the very high vortex shedding phenomenon. It is important to notice that the flow seems to be laminar over the flat plate. No transition is seen. A more detailed analysis of the velocity fields in the wake and of the boundary layers follows later in the report.

4.2.3 Turbulent flow field

The root mean square (RMS) of a signal can be used to evaluate the turbulence intensity of a signal. The RMS is defined and computed as

$$U_{RMS} = \sqrt{\frac{1}{n}\Big((U_1 - \overline{U})^2 + (U_2 - \overline{U})^2 + ... + (U_n - \overline{U})^2\Big)} \tag{4.2}$$

The root mean square of a signal provides information about the magnitude of its fluctuations around its mean. *Turbulence intensity* TI is defined as

$$TI = \frac{U_{RMS}}{U_\infty} \tag{4.3}$$

The RMS value is interesting in aeroacoustics as it can be linked to the sound emission. The TI field of the horizontal and vertical velocity signals are presented in Figure 4.7.

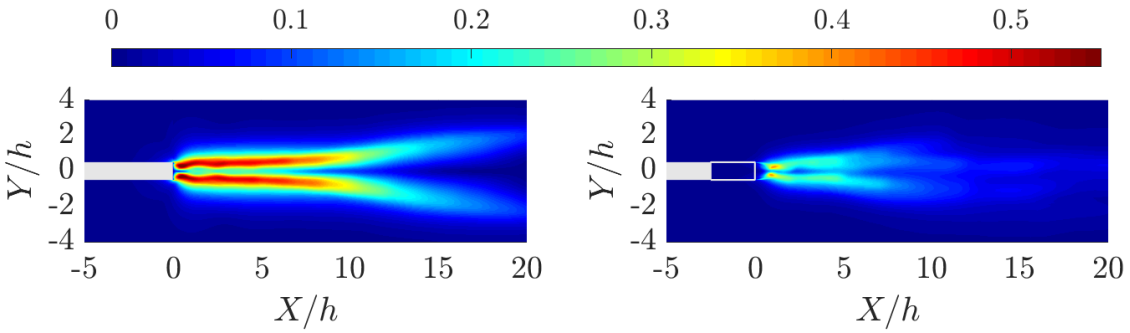

(a) U_{RMS}/U_∞.

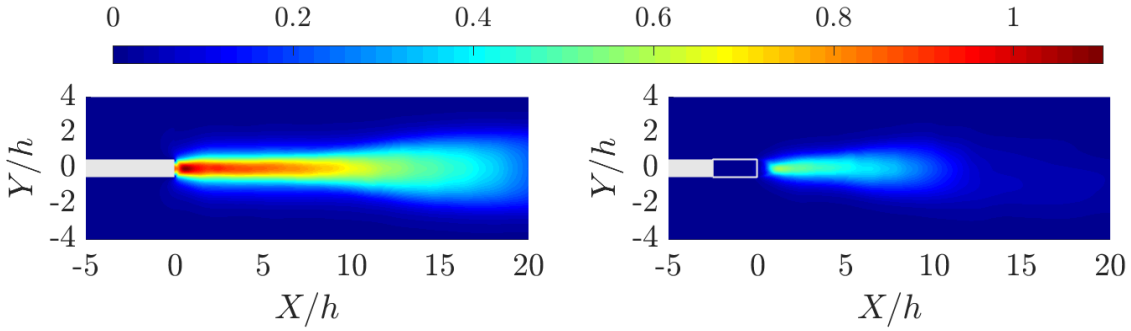

(b) V_{RMS}/U_∞.

Figure 4.7: Turbulence intensity in the wake for U and V.

In the solid case, it can be seen that the RMS of the horizontal and vertical velocity is very high in correspondence of the vortex shedding region $0 < X/h < 20$. The RMS field suggests that the flow is laminar along the flat plate. This could mean that the mesh is not refined enough next to the wall.

The porous insert reduces the RMS of the velocity quite significantly. This statement is valid for both components. Compared to Showkat Ali, results from CFD suggest a very strong effect of turbulence suppression in the wake. On the opposite, Showkat Ali et al. discussed a delay of vortex shedding and velocity reduction in the wake rather than a total suppression of the phenomenon. The reasons for this difference may be:

1. Two-dimensional computations are being compared with three-dimensional measurements

2. Laminar or transitional flow (computed) is being compared with a turbulent one (measured)

In the next section the boundary layers along the plate are inspected in detail.

4.2.4 Boundary layer

Analysing the boundary layer is important to study the connection between viscous phenomena and porous treatments for noise reduction. The presence of a porous surface strongly alters the usual velocity profile within the boundary layer. Understanding how this mechanism occurs can be useful to identify the mechanisms are involved in sound reduction with porous materials.

Figures 4.8, 4.9, 4.10 and 4.11 present the velocity profiles and the RMS at four locations on the surface of the plate for the porous and the solid case, i.e.

$x/c = 0.7$, $x/c = 0.8$, $x/c = 0.9$, $x/c = 0.99$. An alternative representation of the velocity profiles is given in Figure 4.9, where the the non-dimensional velocity is plot against the non-dimensional wall-coordinate y^+. Among the four locations presented, only two (those located more downstream at $x/c = 0.9$ and $x/c = 0.99$) lie above the region where the porous material is implemented, i.e. $[0.857c,\ c]$.

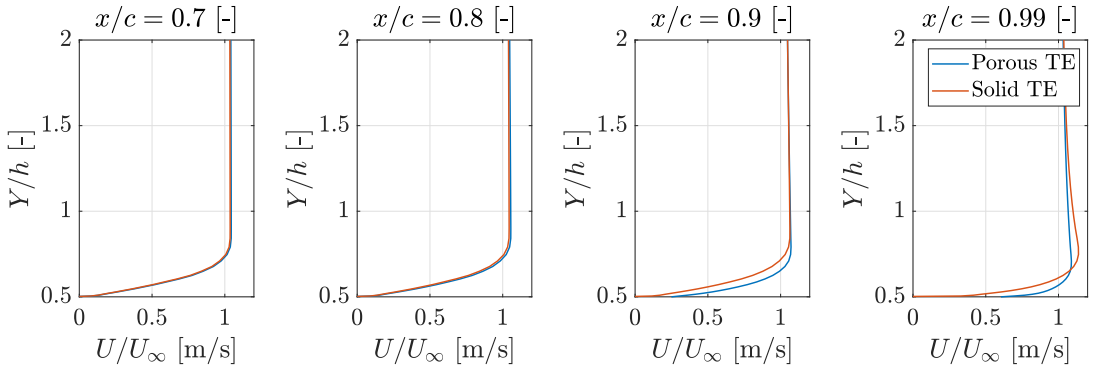

(a) $x/c = 0.7$ **(b)** $x/c = 0.8$ **(c)** $x/c = 0.9$ **(d)** $x/c = 0.99$

Figure 4.8: Horizontal velocity profiles. Solid case (—), porous case (—).

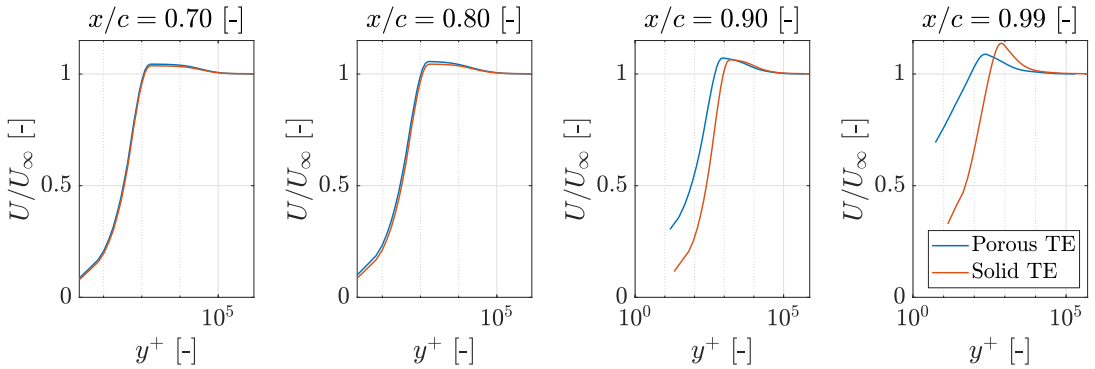

(a) $x/c = 0.7$ **(b)** $x/c = 0.8$ **(c)** $x/c = 0.9$ **(d)** $x/c = 0.99$

Figure 4.9: Horizontal velocity profiles plot against the logarithm of y^+. Solid case (—), porous case (—).

In Figure 4.8 it can be seen that the porous insert increases the velocity in the boundary layer compared to the solid case. However, the overshoot is reduced significantly at $x/c = 0.99$. These aspects were also find by Showkat Ali et al. [9] in their experiments. The presence of a porous material increases the shear of the velocity profile. However, it is interesting to notice that above the porous trailing edge, the non-slip condition is not valid. The profiles plot in Figure 4.9 clearly

show that the solid and porous results start diverging in proximity of the porous insert.

Figure 4.10 illustrates the vertical velocity profiles at the same locations presented above.

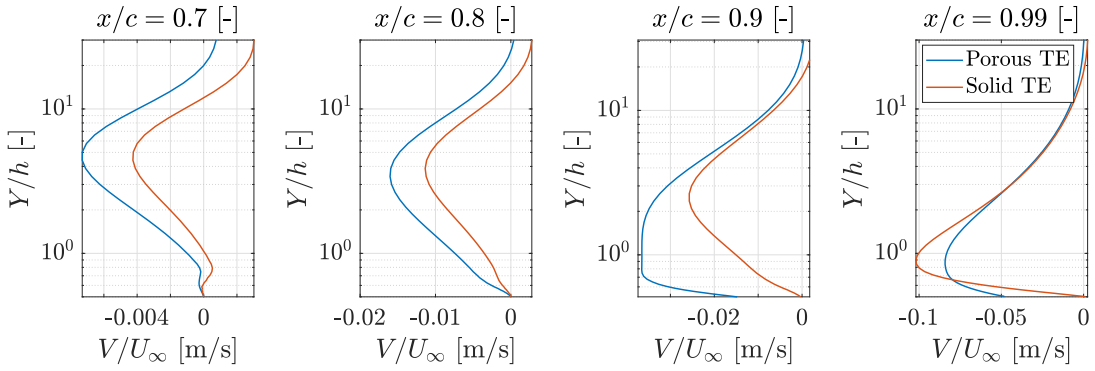

(a) $x/c = 0.7$ **(b)** $x/c = 0.8$ **(c)** $x/c = 0.9$ **(d)** $x/c = 0.99$

Figure 4.10: Vertical velocity profiles. Upper side of the plate. Solid case (—), porous case (—).

At all locations, except for the one most downstream ($x/c = 0.99$), the magnitude of the vertical velocity is increased by the porous treatment. As suggested by Rubio [7], this aspect could be due to the inner hydrodynamic field lying inside the porous media.
As expected, the profiles of the porous case diverges significantly from the solid case above the porous trailing edge. The profile of the root mean square at the trailing edge is plot in Figure 4.11.

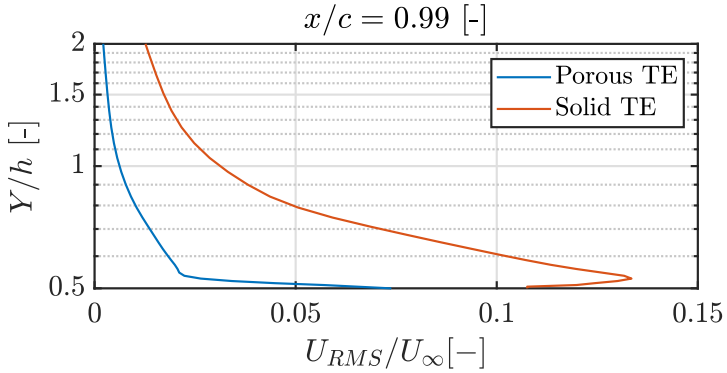

Figure 4.11: Root mean square of horizontal velocity at $x/c = 0.99$. A semi-logarithmic plot was chosen to describe the near wall region. Solid case (—), porous case (—).

From Figure 4.11, it can be seen that the porous trailing edge significantly reduces the RMS at the trailing edge. This is consistent with both Rubio [7] and Showkat Ali [9]. Close to the wall, the RMS is seen to reduce in the solid case due to the wall proximity and the non-slip condition. In the papers from Rubio and Showkat Ali however, the porous media increases turbulence close to the wall. This aspect, which is due to enhanced skin friction with porous media, cannot be captured by CFD. This is because no skin friction can be accounted for.
Table 4.3 summarises the boundary layer parameters, defined previously in Section 3.1.1.3.

Table 4.3: Boundary layer parameters computed at four locations along the flat plate wall. Results for both porous and solid cases are included. The last two location lie above the porous insert.

	$x/c = 0.7$ [-]		$x/c = 0.8$ [-]		$x/c = 0.9$ [-]		$x/c = 0.99$ [-]	
	Solid	Porous	Solid	Porous	Solid	Porous	Solid	Porous
δ^* [mm]	4.3	4.2	4.3	4.0	3.7	2.0	1.4	0.34
θ [mm]	1.94	1.9	1.95	1.86	1.8	1.2	0.9	0.29
H [-]	2.24	2.21	2.19	2.14	2.11	1.68	1.62	1.20
U_f/U_∞ [-]	0.187	0.185	0.179	0.175	0.164	0.119	0.109	0.043
C_F [-]	0.07	0.068	0.064	0.061	0.054	0.028	0.024	0.004

The parameters in Table 4.3 have been computed by defining the boundary layer up to $y = \delta_{99}$, with y being the wall-coordinate at which $U(y) = 0.99U_\infty$. Figure 4.12 gives a visual representation of these parameters along the solid plate.

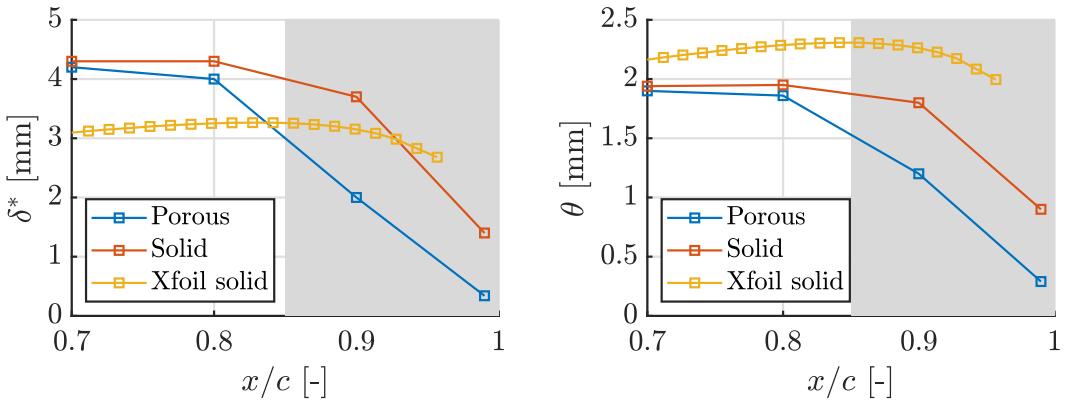

(a) Displacement thickness δ^*

(b) Momentum thickness θ

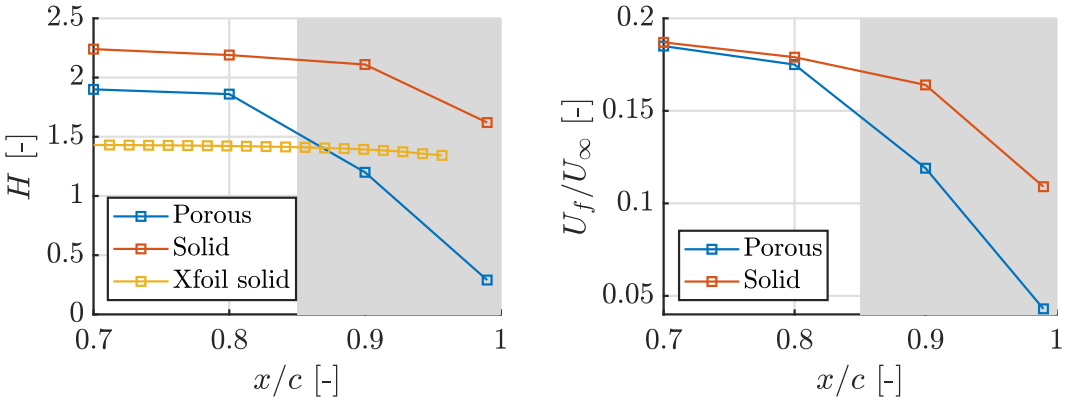

(c) Shape factor H **(d)** Friction velocity U_f/U_∞

Figure 4.12: Boundary layer quantities. The grey background indicates the location of the variable insert. Solid case (—), porous case (—), XFoil solid (—).

The porous insert generally reduces all the boundary-layer parameters compared to the solid case. It is important to point out that at the stations $x/c = 0.9$ and $x/c = 0.99$, the velocity profiles of the porous case are very different from canonical profiles in the boundary layers. This is due to the lack of validity of the non-slip condition in this case.
The results for the shape factor H suggest that in the results from CFD, the flow at the trailing edge is not yet turbulent. Transition phenomena seem to arise for $x/c > 0.8$, while at this location XFoil predicts the flow to be already turbulent, with $H \approx 1.5$.

4.2.5 Trailing edge flow field

With the method implemented, it is possible to visualize the flow inside the porous insert. Firstly, this allows to understand the effect of the Forchheimer term to the overall solution. Secondly, it allows to study the hydrodynamic field mentioned in many experimental papers. Figure 4.13 show the full velocity profile through the trailing edge at $x/c = 0.99$.

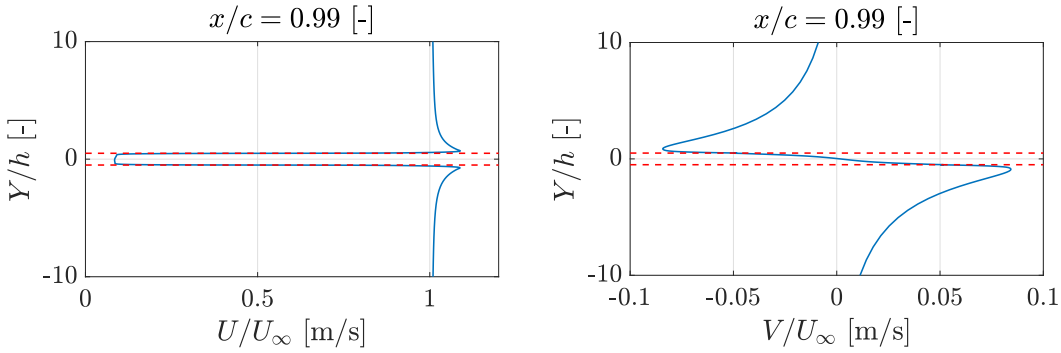

(a) U/U_∞ **(b)** V/U_∞

Figure 4.13: Velocity profiles inside the permeable insert at $x/c = 0.99$.

Figure 4.13a shows that the horizontal velocity is significantly reduced inside the porous material. Its magnitude increases towards the regions located more downstreams. Figures 4.13b show that a linear profile is resolved inside the porous material for the vertical velocity component.

To conclude this analysis, Figure 4.14 shows a zoom of the pressure distribution around the trailing edge.

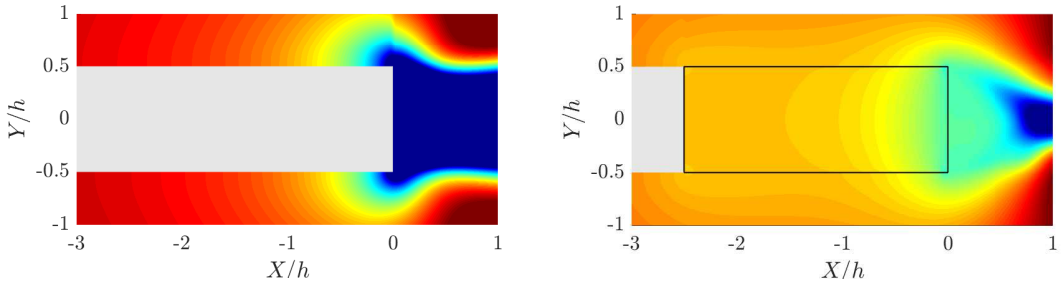

(a) Solid trailing edge. **(b)** Porous trailing edge.

Figure 4.14: Pressure contours at the trailing edge.

Focusing on the porous case in Figure 4.14b, it can be seen that the in correspondence of the boundaries of the trailing edge a discontinuity in the pressure contours. Inside the insert, pressure is seen to gradually increase downstream towards the trailing edge. Overall, the pressure field shows less variation than the solid case. In fact, a very high discontinuity can be seen at the solid trailing edge. To conclude, an articulated hydrodynamic field is resolved inside the porous trailing edge. This phenomenon could be relevant to explain the noise scattering mechanism from partially porous bodies with high bluntness.

4.2.6 Validation with experimental data

In this section, results from CFD in the wake are directly compared with experimental data acquired with particle image velocimetry (PIV) by Showkat Ali et al. [9]. This experiment was the main reference for the setup of the CFD study. Figure 4.15 presents the results for the velocity fields in the wake with a fully solid model, while the porous case is showed in Figure 4.16.

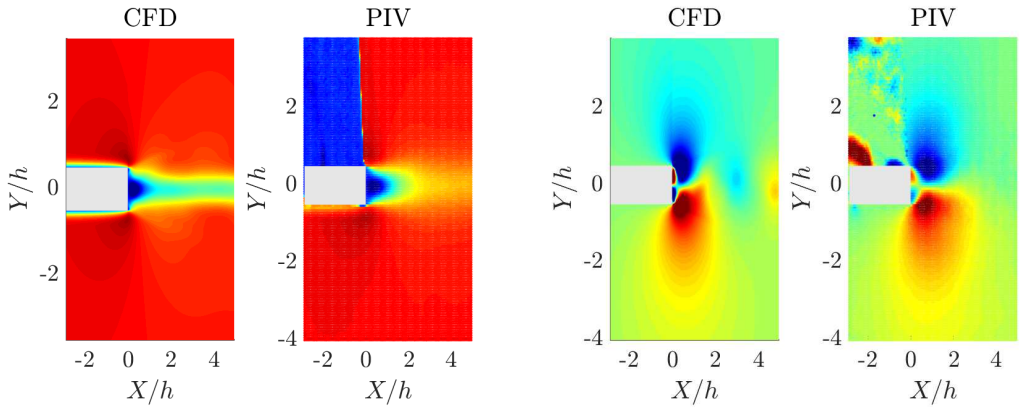

(a) Non-dimensional horizontal velocity. **(b)** Non-dimensional vertical velocity.

Figure 4.15: Comparison between the results for the velocity fields in the wake from CFD and wind tunnel measurements from Showkat Ali et al. [9]. Solid insert case.

The region above the trailing edge in the plots of the results from PIV, for $Y/h > 0$ and $X/h > 0$ is a shadow for the camera used. Hence, experimental results in this area are not meaningful.
Figure 4.15 allows to state that, compared to experimental results, the wake deficit of the horizontal velocity component is much stronger. A reason for this could be that in the CFD simulations the flow is still laminar. In the vertical coordinate the results are pretty similar close to the wall. In the far wake a high vortex shedding phenomenon is visible in the CFD results. This does not occur in the wind tunnel measurement and could be due to enhanced strength of 2D vortices compared to 3D.
In the porous case in Figure 4.16, a much closer agreement between computations and measurements can be seen. The numerical results predict a similar wake recovery to the one measured experimentally.

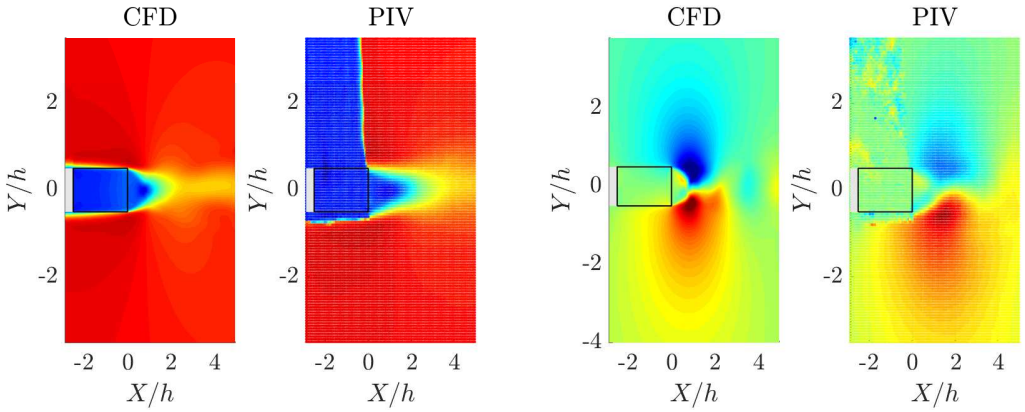

(a) Non-dimensional horizontal velocity. **(b)** Non-dimensional vertical velocity.

Figure 4.16: Comparison between the results for the velocity fields in the wake from CFD and wind tunnel measurements from Showkat Ali et al. [9]. Permeable insert case.

The vertical velocity computed numerically has a similar trend to the experimental results. Once again, a stronger magnitude can be observed. This effect could be enhanced by the fact that two-dimensional simulations are being compared to three-dimensional measurements.

4.2.7 Wake

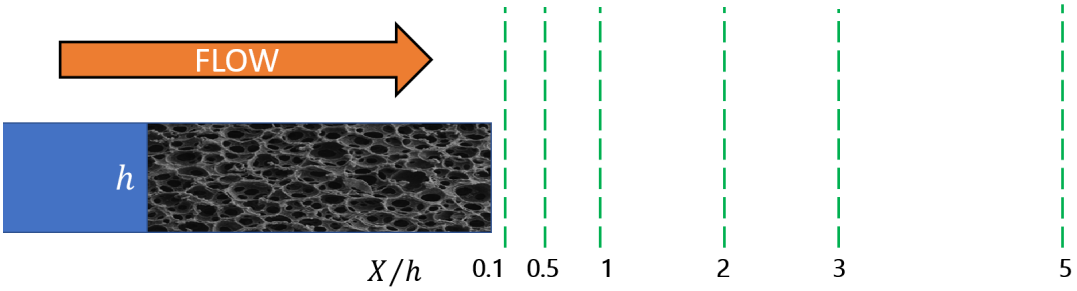

Figure 4.17: Stations considered for velocity analysis in the wake.

A more detailed comparison can be made if the velocity profiles in the wake are extracted and plotted at different locations in the wake. Five stations were isolated. A sketch of their position relatively to the trailing edge is presented in Figure 4.17. Figure 4.18 presents the velocity profiles evaluated at these stations.

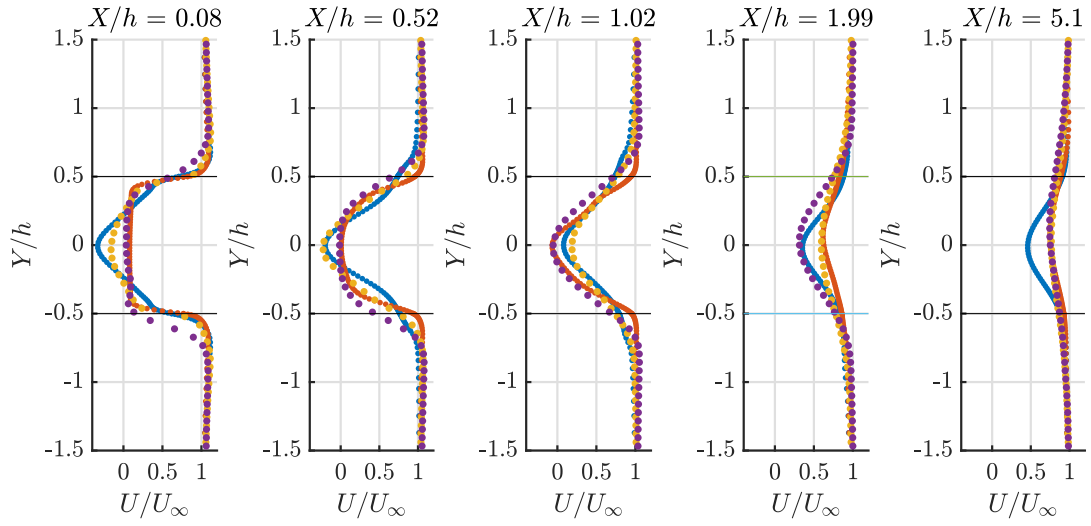

(a) Horizontal velocity profiles in the wake.

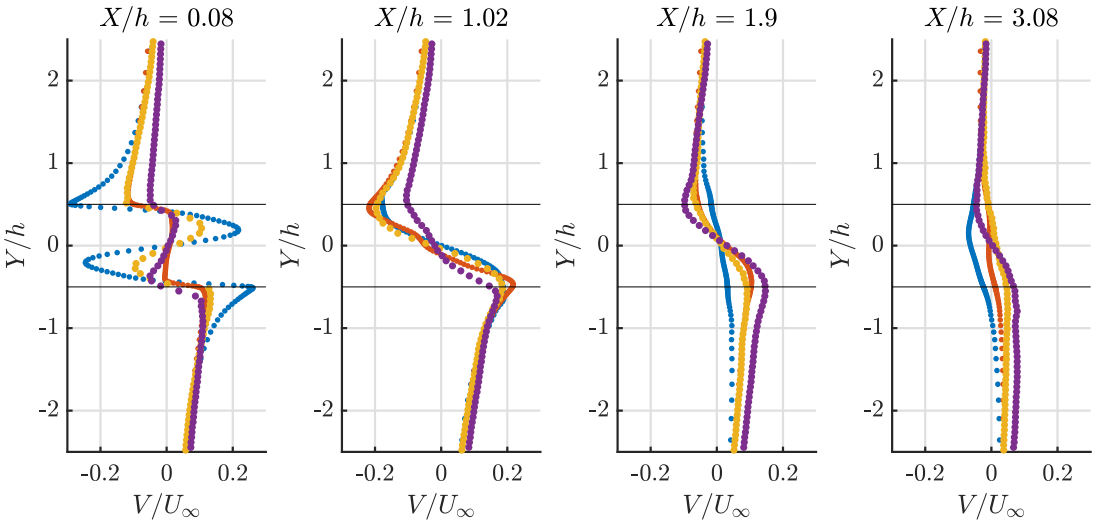

(b) Vertical velocity profiles in the wake .

Figure 4.18: Wake velocity analysis compared with wind tunnel measurements [9] (Solid case, CFD ●; Porous case, CFD ●; Solid case, PIV ●; Porous case, PIV ●).

The comparison of the horizontal velocity profiles in Figure 4.18 confirms a good match between experiments and computations up to $X/h = 1$. In the far wake the results tend to diverge significantly, especially for the solid case.
Overall, the velocity reduction observed by Showkat Ali can be also observed in the CFD results. In the near wake, the higher deficit caused by porous materials is responsible for the reduced drag.
Regarding the vertical velocity profiles in Figure 4.18b, it can be said that the

resemblance between CFD and measurements is poorer than the horizontal velocity profiles. However, the porous and solid case follow the same trends in the numerical and experimental results. Specifically, the porous insert presents higher vertical velocities than the solid case close to the "virtual" wall. More downstream, the opposite trend can be observed.

4.3 Discussion

The results of this validation case on a flat plate allow to state that penalization method could be a promising way to study flows through porous materials. Indeed, the modified Navier-Stokes equations provided results which are in line with wind tunnel results from [9]. The partially porous plate suppresses vortex shedding and alters the velocity profiles in the wake. The presence of a hydrodynamic field inside the porous material was observed. This phenomenon strongly mitigates the pressure discontinuity at the trailing edge.
The validity of the mesh used should be inspected further, as the boundary layer discretization should be finer. Furthermore, a trip of the boundary layer should be added to ensure the presence of turbulent flow along the plate. Finally, a sensitivity analysis of the constant C_0 for LES should be made.

Chapter 5

Numerical study: NACA0018

The next step in the numerical analysis is to apply the method to inspect airfoil flows. A symmetric 18% thick NACA0018 was chosen to replicate the experiments from Rubio at TU Delft [7]. The equivalent streamwise coordinates x and X used are showed in Figure 5.1.

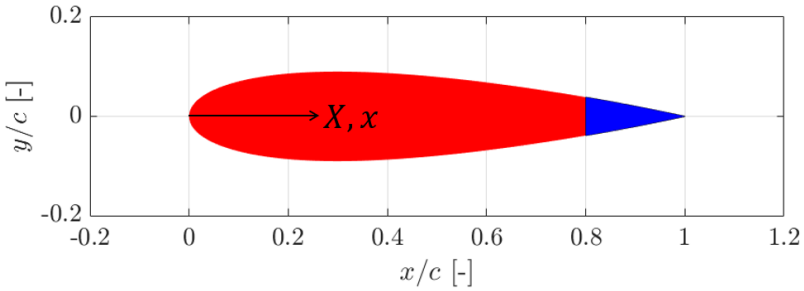

Figure 5.1: Streamwise coordinates for NACA0018 airfoil case.

5.1 Mesh

The procedure to obtain a correct mesh for the airfoil study case took a big portion of the total time available. Initially, erroneous results were obtained due to a poor mesh. After a study of the mesh quality, it was found that the reason for the poor results was the coarse discretization of the boundary layer.
The mesh was then re-built concentrating 32 points in the boundary layer (estimated height of 10 mm). The height of the first cell was chosen to be 0.2 mm to capture the required y^+ (see Section 3.3.1). In order to reach the desired height of 10 mm, a cosine distribution was used to slightly stretch the mesh in the refined

region, after which the usual hyperbolic tangent distribution was applied. The downside of this is a poor discretization outside the boundary layer, which reduces accuracy when dealing with turbulent flows with high boundary layer thickness. In a future refinement of this work, one of the first things to do would be to increase the number of blocks in the orthogonal direction and in the wake.
The final version of the mesh is presented in Figure 5.2.

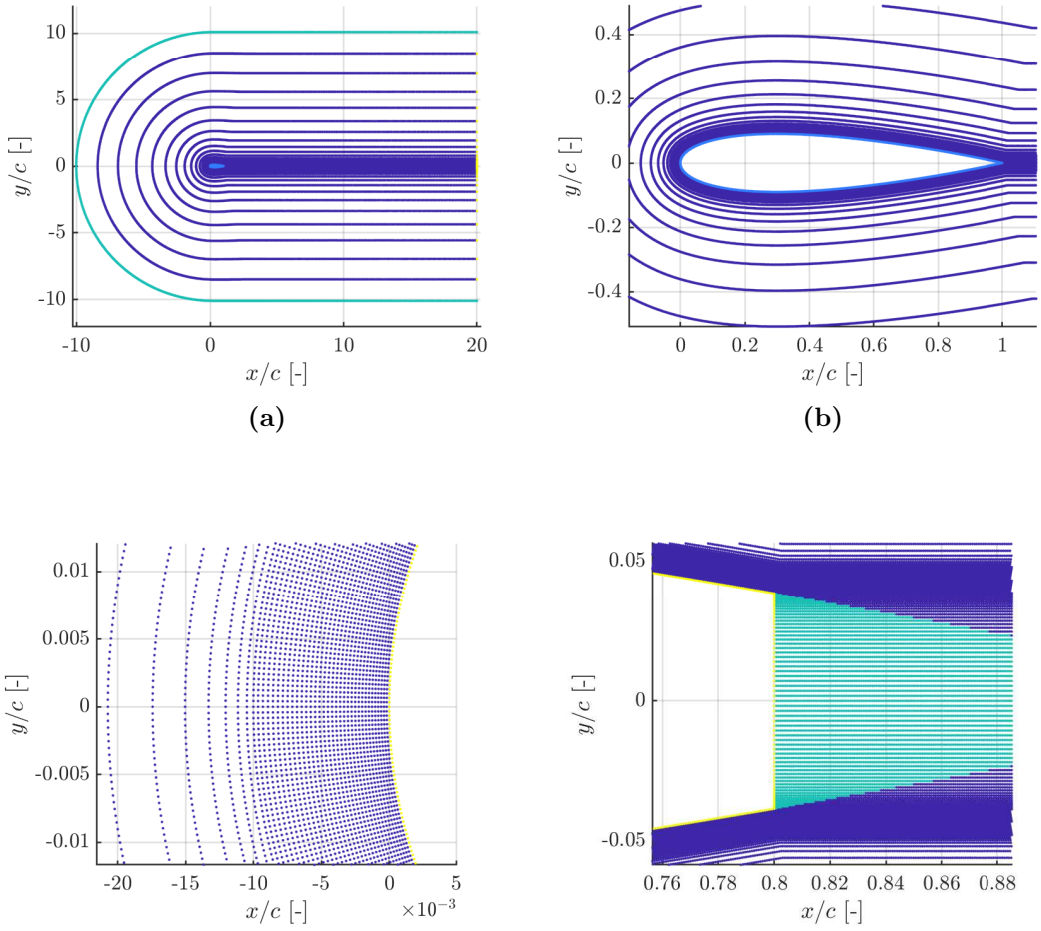

Figure 5.2: Mesh of a NACA0018 equipped with a porous trailing-edge. The porous attributes are marked in green. The wall with no-slip condition are marked in yellow (Figure c,d) and in light blue (Figures a,b).

Figure 5.2c highlights the presence of a very fine region within the boundary layer and a coarse mesh outside of it. The porous trailing edge was meshed with a simple, orthogonal grid, in which the points lying inside the trailing edge

are marked as porous. This can be seen in detail in Figure 5.2d. The meshing technique of the porous trailing edge is very basic. Its main downsides are the impossibility to extract velocity profiles within the boundary layer, and the coarse discretization of the very end of the body. In future work, the mesh could be improved by maintaining orthogonality between solid-porous interface and mesh lines.
Due to lack of time, no sensitivity analysis on this mesh was performed. It is hence very likely that results could be improved with a further analysis in this direction. The domain was divided in regions to build the mesh. Figure 5.3 compares the two strategies used for solid and porous.

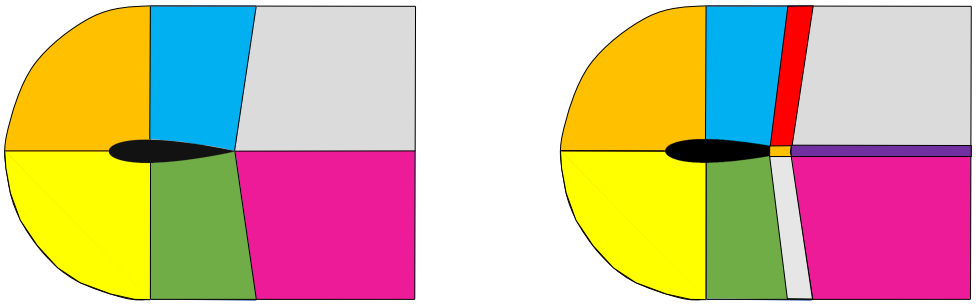

(a) Solid case. **(b)** Porous case.

Figure 5.3: Mesh strategy, block division.

Each region, marked by a different color, is divided in blocks. In the porous case, a blunt airfoil is meshed, and this requires higher number of mesh regions in the wake. The total number of blocks was carefully obtained to find the right balance between computational cost and reliability of results.

5.2 Trip of the boundary layer

Due to the relatively low Reynolds numbers considered for a turbulent flow, it is needed to trip the boundary layer to force transition from laminar to turbulent flow.

In the current study, a turbulent flow is essential to study the broadband trailing-edge noise phenomenon. Implementing a trip to force transition to turbulence is not trivial with LES in 2D. The reason for this, is that the very small eddies (usually) generated with a perturbation to trip the boundary layer must not be quickly dissipated. To achieve this, the eddy viscosity must be monitor. Most often, this coincides with a very fine mesh. Indeed, a coarse mesh could imply a significant loss of information, which would prevent turbulence structures

generated at the perturbation from developing downstream.
The most common techniques to trip the boundary layer in two-dimensional CFD are:

1. Simulation of roughness particles
2. Simulation of a single roughness element
3. Source term for perturbation

In the current thesis, points 2 and 3 were studied in detail.

5.2.1 Localized perturbation in the momentum equation

One of the most applied methods in literature, is the inclusion of a source term S_{trip} in the momentum equation to simulate the effect of a trip. In this work, the perturbing source term S_{trip} was defined in the domain with the aid of a Gaussian distribution, centred on the trip location. The use of such a distribution allows to localize the effect of the trip in the desired locations, smoothly enough to ensure numerical stability.
Equation 5.1 shows the distribution, in which A represents the magnitude of the source term and a, c are chosen to determine the *steepness* of the distribution.

$$S_{\text{trip}}(x, y) = Ae^{-(a(x-x_0)^2+c(y-y_0)^2)} \tag{5.1}$$

Figure 5.4 gives an example of the distribution of S_{trip} for $a = 10^3$, $c = 10^5$.

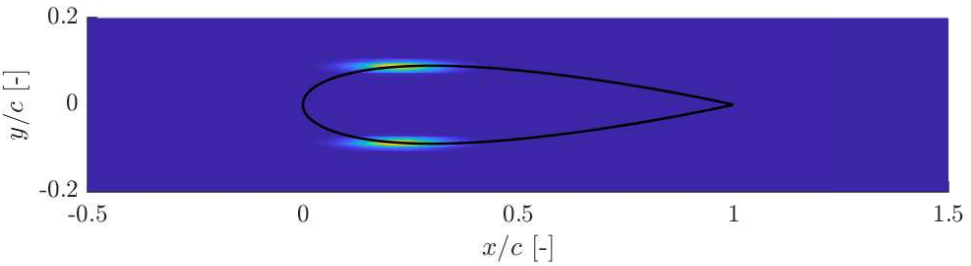

Figure 5.4: Non-symmetric Gaussian "*bell*" centered at $x/c = 0.225$ to simulate a trip in the boundary layer. Gaussian function parameters used: a = 10^2, c = 10^4.

The amplitude obtained from Equation 5.1, was then decomposed on x and y to simulate a force acting perpendicularly to the airfoil. The decomposition is

showed in Equations 5.2 and 5.3.

$$S_{\text{trip},x} = S_{\text{trip}}(x, y) \cos \zeta \tag{5.2}$$

$$S_{\text{trip},y} = S_{\text{trip}}(x, y) \sin \zeta \tag{5.3}$$

For a trip located at $x/c = 0.2$ and a NACA0018 airfoil, $\zeta \approx 93.5°$ on the top surface and 266.5° on the bottom one.
The distribution described above was combined with a suction/blowing term, following the work of Huai et al. [26]. The authors succesfully applied this technique for a three-dimensional channel flow using large eddy simulation as turbulence model.
The unstable perturbation is obtained by combining time-dependent with space-dependent terms. The time-dependent term is made of a fundamental and a subharmonic mode, lying at different frequencies. The perturbation from Huai is defined as

$$S^*(\chi, t) = A_1 \mathcal{F}(\chi) \sin(\Omega t) + A_2 \mathcal{F}(\chi) \sin\left(\frac{\Omega}{2} + \text{phase}\right) \tag{5.4}$$

where A_1 and A_2 are amplitudes. Ω is the frequency of the oscillating perturbation. $\mathcal{F}(\chi)$ is a function of the streamwise coordinate χ defined along the trip region. In this work it was defined with a 5th-order polynomial, as

$$\mathcal{F}(\chi) = P_1 \chi^5 + P_2 \chi^4 + P_3 \chi^3 + P_4 \chi^2 + P_5 \chi \tag{5.5}$$

with

$$\begin{aligned} P_1 &= -120.63 \\ P_2 &= 301.59 \\ P_3 &= -242.56 \\ P_4 &= 62.25 \\ P_5 &= -0.64 \end{aligned}$$

A visual representation of $\mathcal{F}(\chi)$ is presented in Figure 5.5. The final source term, obtained by combining the Gaussian distribution with the space/time dependent term, is presented in Equation 5.6.

$$S_{\text{perturbation}}(x, y, \chi, t) = S_{\text{trip}}(x, y) \left[A_1 \mathcal{F}(\chi) \sin(\Omega t) + A_2 \mathcal{F}(\chi) \sin\left(\frac{\Omega}{2} + \text{phase}\right) \right] \tag{5.6}$$

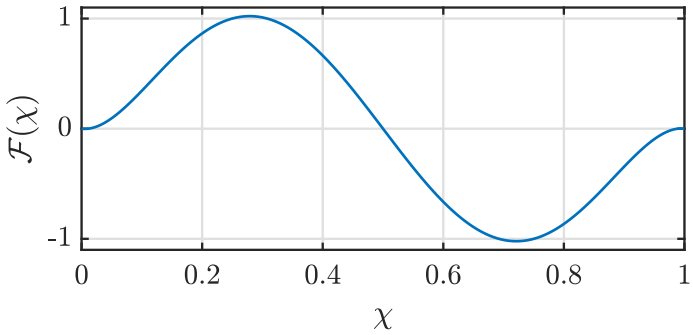

Figure 5.5: $\mathcal{F}(\chi)$ function along the trip.

5.2.1.1 Results

Three cases have been inspected to determine the right parameters to force transition without affecting the flow too significantly. The cases are described in Table 5.1.

Table 5.1: $a = 10^3$, $b = 10^5$.

Case #	Ω [Hz]	A	A_1	A_2	C (LES)
1	110	1	10^{-3}	10^{-5}	0.02
2	110	1	2.510^{-3}	10^{-4}	0.02
3	110	1	2.510^{-3}	10^{-4}	0.01

The results regarding boundary layer quantities are showed in Figure 5.6.

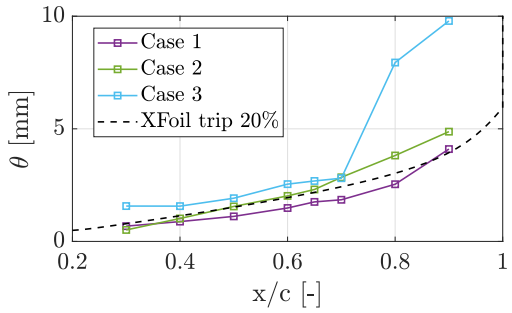

(a) Displacement thickness θ.

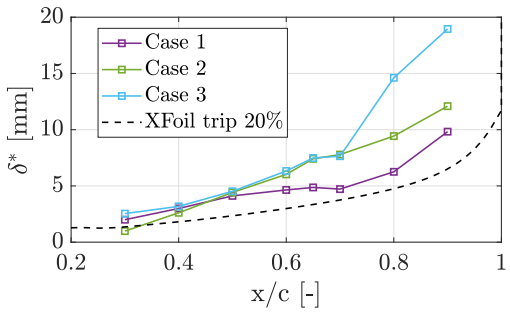

(b) Displacement thickness δ^*.

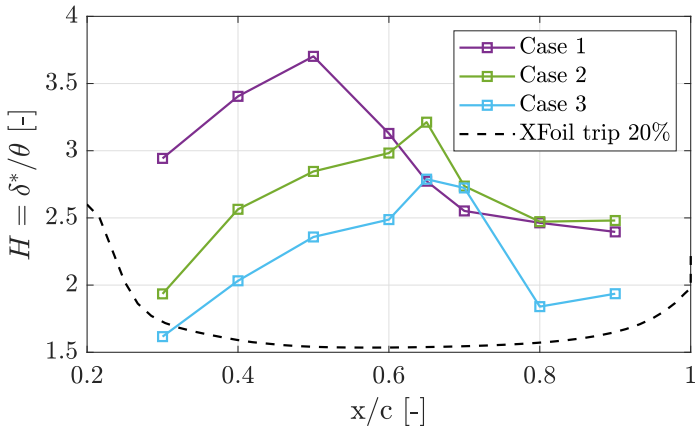

(c) Shape factor H.

Figure 5.6: Boundary layer analysis with a perturbation introduced as a source term. Three cases with different parameters are inspected. The solution from XFoil features forced transition at $x/c = 0.2$.

Case 1 shows the best agreement with the result from XFoil regarding both displacement thickness and momentum thickness. However, the shape factor H shows significant disagreement. Cases 2 and 3 have the lowest value for H immediately after the perturbation at $x/c = 0.3$. This means that the boundary layer is given high momentum from the perturbation. However, moving downstream, it seems that turbulence is dissipated and the shape factor increases towards a maximum. This could mean the presence of transitional flow.
The method seems promising, especially with Case 1. It is likely that with an accurate tuning of the parameters available, this kind of perturbation could trigger transition to turbulence. Due to lack of time, the trial and error process required for tuning could not be actuated.

5.2.2 Single roughness element

A rectangular protrusion was included in the mesh at the trip location. Figure 5.7 provides an example.
The mesh, originally written for a smooth case, is obtained by shifting a set of blocks of the mesh in the wall-orthogonal direction, at the trip location. The height of the step is determined by the amplitude of the aforementioned shift.
The disadvantage of this method is that it requires a very fine mesh to resolve the very small eddies which are responsible for transition. The mesh needs to be very fine to allow the eddies to be transported downstream. A coarse mesh would imply an undesirable loss of information, which would make the step completely

ineffective.

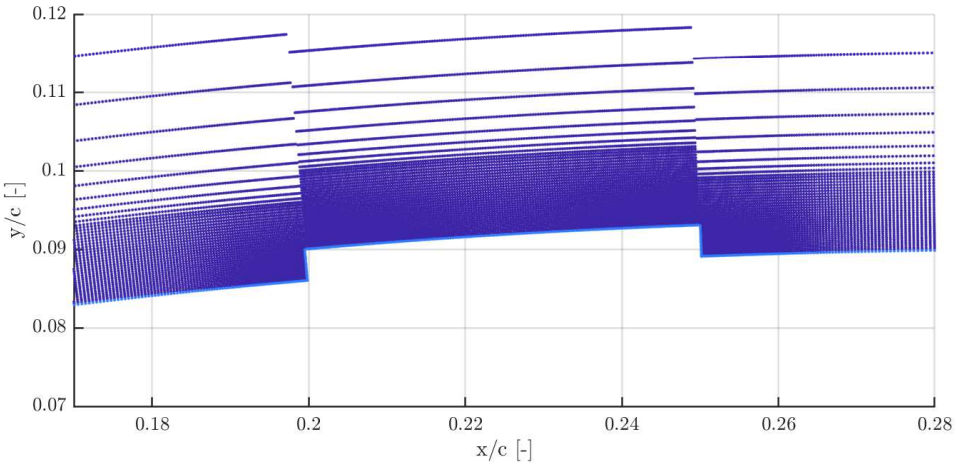

Figure 5.7: Example of trip implemented in the airfoil geometry at $x/c = 0.2$. In this Figure, the height of the step is 4 mm. The mesh has been refined in correspondence of the leading-edge and the trailing-edge of the step.

5.2.2.1 Sensitivity analysis of the step height

To choose the correct height of the step, a sensitivity analysis was prepared. In wind tunnel experiments, such as [7] and [9], roughness particles for tripping have a diameter lower than 1 mm. In two-dimensional computations with LES, it is expected that a higher magnitude should be applied. For this reason, 1 mm, 2 mm and 4 mm rectangular steps are studied.

Figure 5.8 shows the effect of the presence of the perturbation on the drag coefficient.

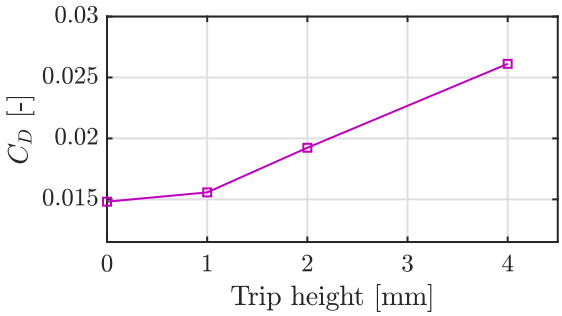

Figure 5.8: Influence of the trip height on the drag coefficient. Constant C_0 for LES set to 0.01 .

As expected, drag increases significantly with the height of the step used. The mean horizontal velocity profiles at different locations in the boundary layer are plot, for different step sizes in Figure 5.9.

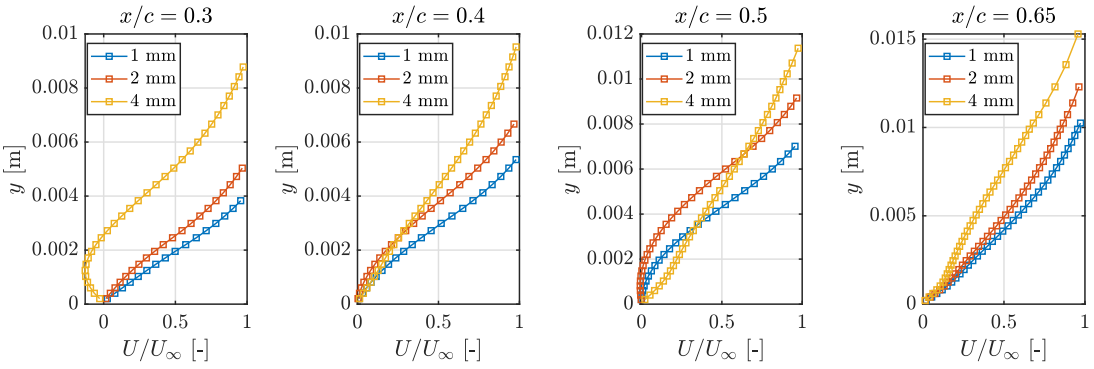

(a) $x/c = 0.3$. **(b)** $x/c = 0.4$. **(c)** $x/c = 0.5$. **(d)** $x/c = 0.65$.

Figure 5.9: Velocity profiles in the boundary layer at different streamwise locations.

Similar trends can be observed for the 1 mm and 2 mm cases. The thickness of the boundary layer increases with the height of the step. The 4 mm step varies the trend of the velocity profiles significantly. In fact, at $x/c = 0.3$ a portion of negative velocity can be seen close to the wall. This means that a recirculation region is present in proximity of the step. The analysis of the boundary layer quantities is showed in Figure 5.10.

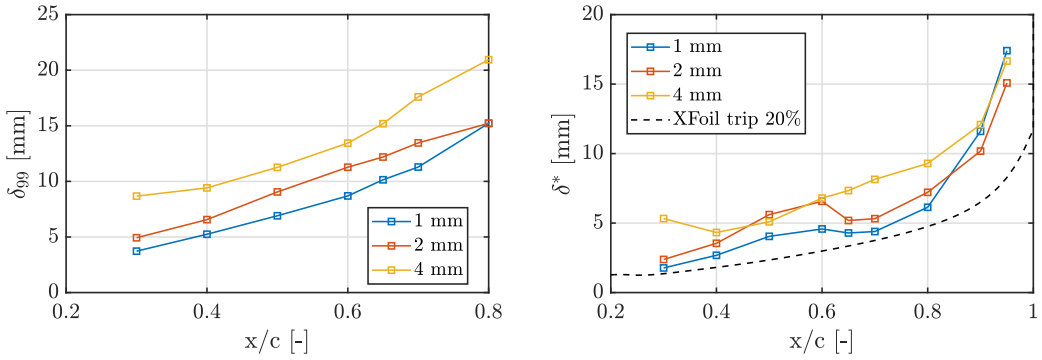

(a) Boundary layer thickness δ_{99}. **(b)** Displacement thickness δ^*.

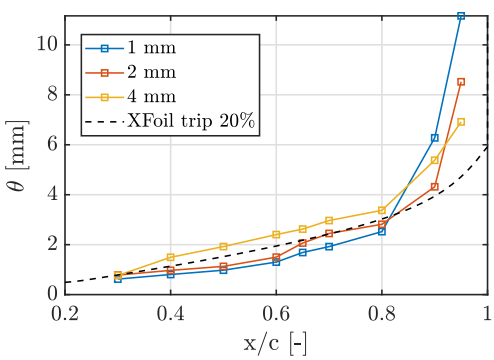

(c) Momentum thickness θ.

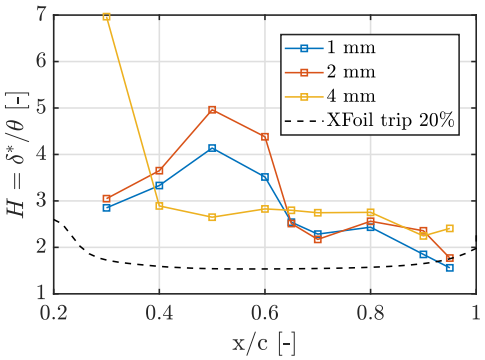

(d) Shape factor H.

Figure 5.10: Boundary layer analysis with a perturbation introduced by a single roughness element (i.e. a rectangular step). Three elements with different heights are studied (1 mm, 2 mm, 4 mm). The solution from XFoil was obtained by imposing forced transition at $x/c = 0.2$.

As observed in the previous paragraph, the boundary layer thickness, displacement thickness and momentum thickness grow with the height of the step. For $x/c > 0.8$, results may not be reliable due to the high δ_{99}, reaching coordinates at which the mesh used is already very stretched and coarse. The trend for the shape factor H suggests that the 4 mm case is the only one to suppress the high peak, typical of natural transition phenomena. For this reason, the 4 mm step was chosen as tripping element. It would be interesting to inspect even higher steps, but numerical stability should be carefully monitored when doing so.
In the remaining part of this chapter results for clean and perturbed configurations are presented.

5.3 Numerical stability and convergence

The numerical stability of the simulations was checked. Specifically, both normalized residuals for pressure and velocity were inspected. Plots are available in Appendix C for both clean and perturbed configurations. Furthermore, residuals after each iteration within a timestep of the SIMPLE were monitored. In all computations (both clean and perturbed) these were reduced by one order of magnitude, generally from 10^{-4} to 10^{-5}. Furthermore, residuals before and after the iterative solution of the pressure equation were reduced by two orders of magnitude.
Overall, the addition of a perturbation in the forms of single roughness elements or source terms affected the residuals for pressure. The higher the magnitude of the perturbation, the higher instability is introduced in the solution.

5.4 Clean configuration

The non-perturbed configuration was considered as benchmark. The main inputs to the CFD software are presented in Table 5.2.

Table 5.2: Review of main parameters used in the simulations of the NACA0018 airfoil without trip.

Chord-based Reynolds number	263,000	[-]
Free stream velocity U_∞	4	m/s
Timestep Δt	5×10^{-4}	s
Total time for averaging	4 (5-9)	s
Relaxation pressure α_p	0.1	[-]
Relaxation velocity α_u	0.9	[-]
Constant C_0 LES	0.02	[-]
Constant α LES	0.5	[-]
Sub-iterations	22	[-]
Kinematic viscosity ν	1.5×10^{-5}	m^2/s
Porosity ϕ	0.92	[-]
Permeability K	3.4×10^{-8}	m^2
x-location porous trailing edge	[0.8, 1]	c
Angle of attack	0	$^\circ$
Mesh blocks 64×64	60	[-]
Height first cell	1.96×10^{-4}	c
y^+ first cell ($x/c = 0.3$)	14	-
Mesh blocks in the wake (**solid** case)	8	[-]
Mesh blocks in the wake (**porous** case)	4 (TE) + 4	[-]

Compared to the flat plate case presented in Chapter 4, there are few differences. First, the constant for LES C_0 is halved. This was done after reviewing literautre [27], to improve the accuracy of the results. The effect of halving C_0 is to halve the eddy viscosity. This aspect implies less dissipation in the development of turbulent structures within the boundary layer and in the wake. Next, the timestep is increased. This was allowed by the lower free-stream velocity and its effect on the Courant number. Finally, the porous material used has higher values of porosity and lower ones of permeability. Furthermore, it extends for a longer distance (i.e. 20% of the chord). For these reasons, its effect should be even more evident in this study case. In the non-perturbed configuration, the mesh consists of 60 blocks for both porous and solid case. The need to mesh the trailing edge for the porous case leads to a much coarser mesh in the wake compared to the solid case. Finally, the Reynolds number was chosen to match wind tunnel

measurements from Rubio presented in [7].

5.4.1 Results

In this section, results obtained for the clean case are presented.

5.4.1.1 Mean flow field

The mean field was computed by averaging the flow over 4 seconds. A plot of the pressure coefficient is showed in Figure 5.11.

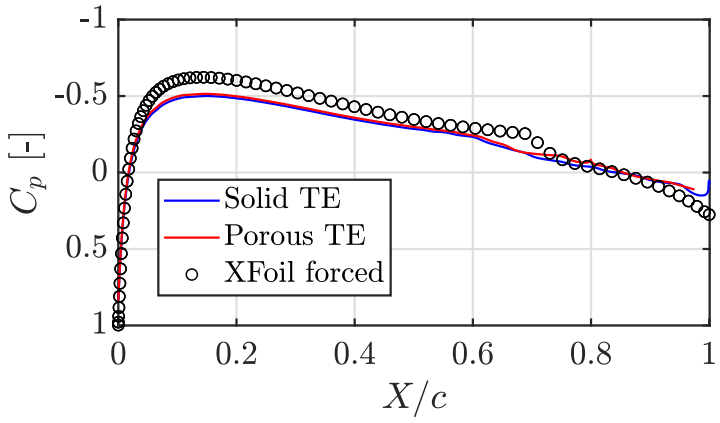

Figure 5.11: Pressure coefficient.

In both solid and porous case, C_p is similar at the leading edge. As observed for the flat plate case, the coefficient is overestimated compared to XFoil. Transition occurs at $x/c = 0.6$ in both solid and porous cases, with a similar trend for C_p downstream. CFD predicts earlier transition than XFoil. The mean fields of velocity and pressure are plotted in Figure 5.12.

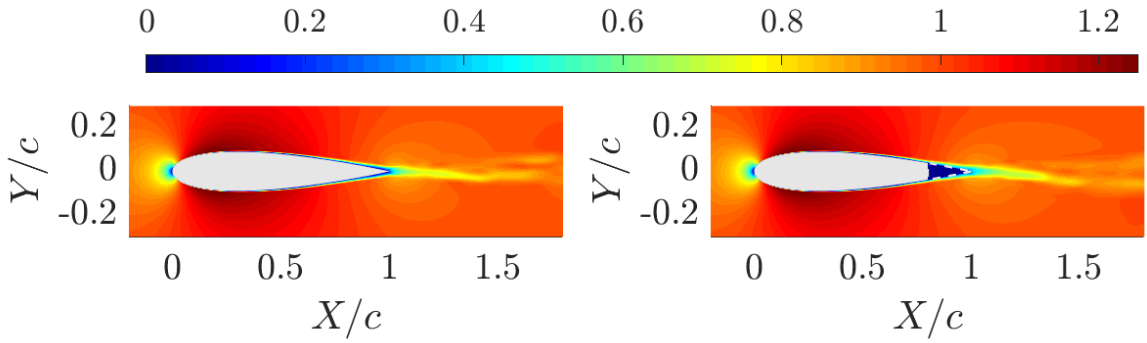

(a) Mean horizontal velocity field non-dimensionalised with U_∞.

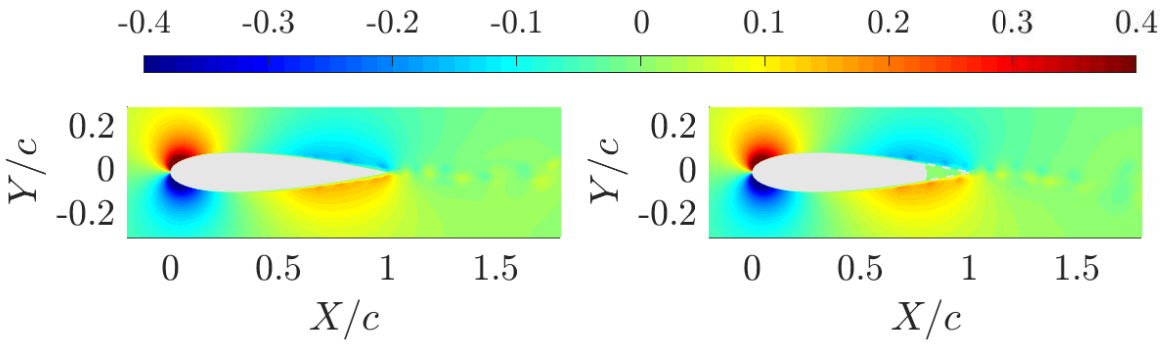

(b) Mean vertical velocity field non-dimensionalised with U_∞.

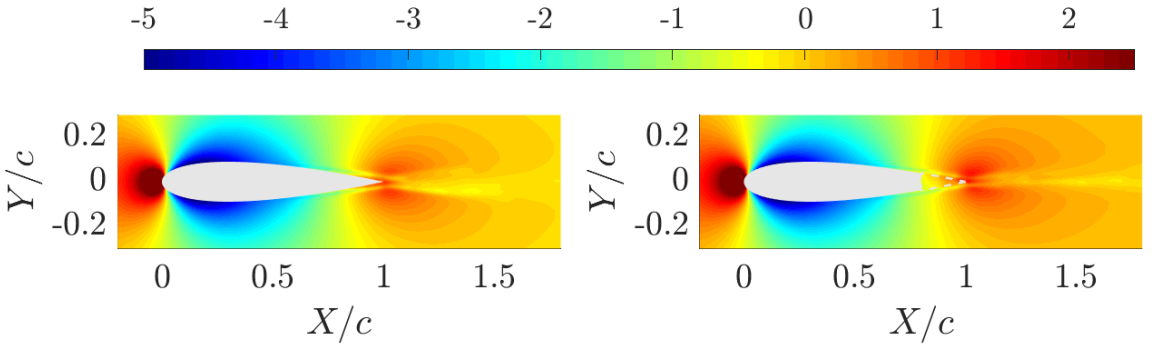

(c) Mean pressure field non-dimensionalised with the maximum field value.

Figure 5.12: Mean fields for a symmetric NACA0018 airfoil at zero angle of attack with a solid (left) and a porous (right) trailing edge. Reynolds number of 263,000. The flow is averaged over 4 seconds.

Similar results for solid and porous cases can be seen along the airfoil. The most relevant differences are concentrated in the wake. This region will be analysed in Section 5.4.1.4. The most interesting aspect from Figure 5.12 is the pressure field in Figure 5.12c. A high pressure region is present at the solid-porous interface, similarly to the solid case. However, another high pressure region develops inside the porous insert, and eventually this affects the near wake significantly. It is important to state that the average field in the wake is not yet converged. Figure 5.12c allows to see this.

5.4.1.2 Boundary layer

The boundary layer is studied in this section. Unlike the wake, for which convergence was not reached, it is expected that in this region the 4 seconds available for

averaging are sufficient to converge. As already mentioned, because of the mesh used for the porous trailing edge, it was not possible to study the boundary layers o top of the permeable insert. The results concerning the parameters describing the boundary layer are plotted in Figure 5.13.

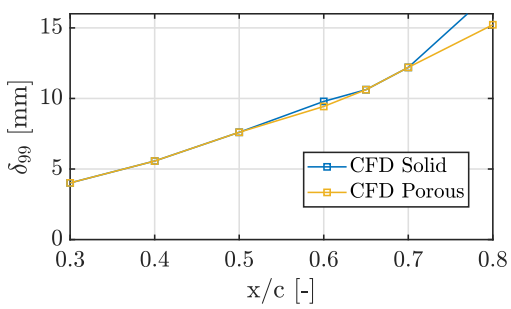

(a) Boundary layer thickness δ_{99}.

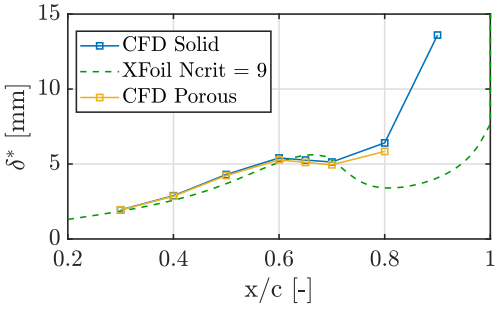

(b) Displacement thickness δ^*.

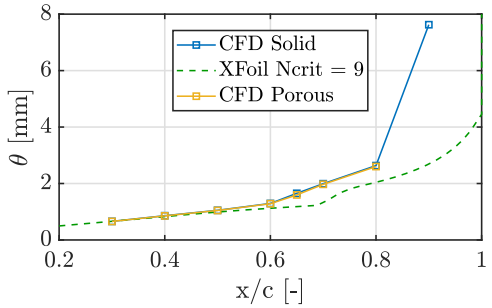

(c) Momentum thickness θ.

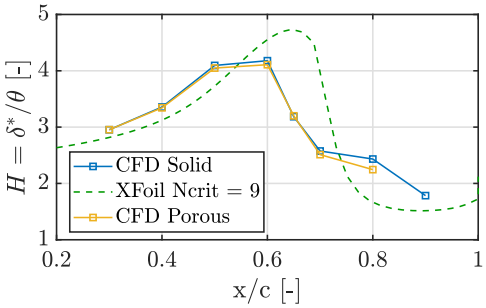

(d) Shape factor H.

Figure 5.13: Boundary layer analysis.

A very close agreement between solid and porous cases can be seen. Transition to turbulence is occurring around $x/c = 0.6$ with a sharp decrease on H.

5.4.1.3 Turbulent flow field

Turbulence is studied in this section. Turbulence intensity for U and V on the airfoil is plot in Figure 5.14.

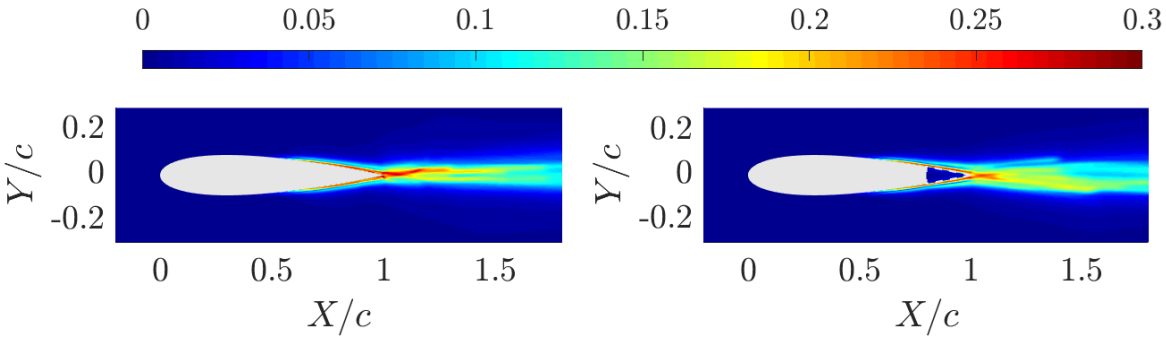

(a) U_{RMS}/U_∞

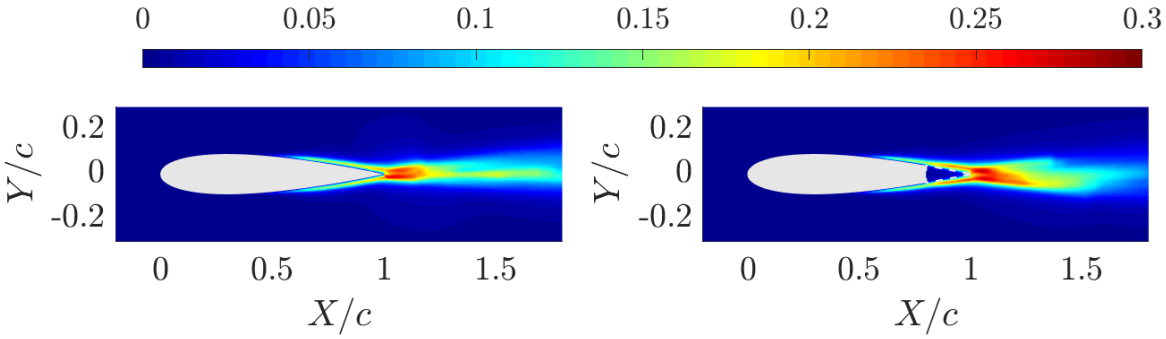

(b) V_{RMS}/U_∞

Figure 5.14: Turbulence intensity.

The trends of RMS are similar in solid and porous cases. The porous material seem to reduce the RMS of horizontal velocity in correspondence of the permeable trailing edge. On the opposite, an increase in turbulence intensity at the trailing edge can be observed for the vertical component V. The mean fields in the wake are not converged yet. More averaging time would be beneficial but was not available. However, it can be said that the porous material increases the RMS of V in the near wake, while it reduces it in the far wake.
Next, time series of velocity and pressure were collected above the porous trailing edge. Because of the different meshes used for porous and solid cases, only a

storage position at $x/c = 0.95$ was found to be in common to both solid and porous meshes. The location of the measurement point in the solid case lies at $(0.9573c, 0.0106c)$, at a distance of $0.0016c$ from the solid wall. The measurement point in the porous case lies at $(0.9578c, 0.0106c)$, $0.0017c$ away from the solid-porous interface. Velocity and pressure signals have been recorded for 2 seconds, which is considered to be enough to converge the mean fields in the boundary layer. Fast Fourier transforms of the time signals are showed in Figure 5.15.

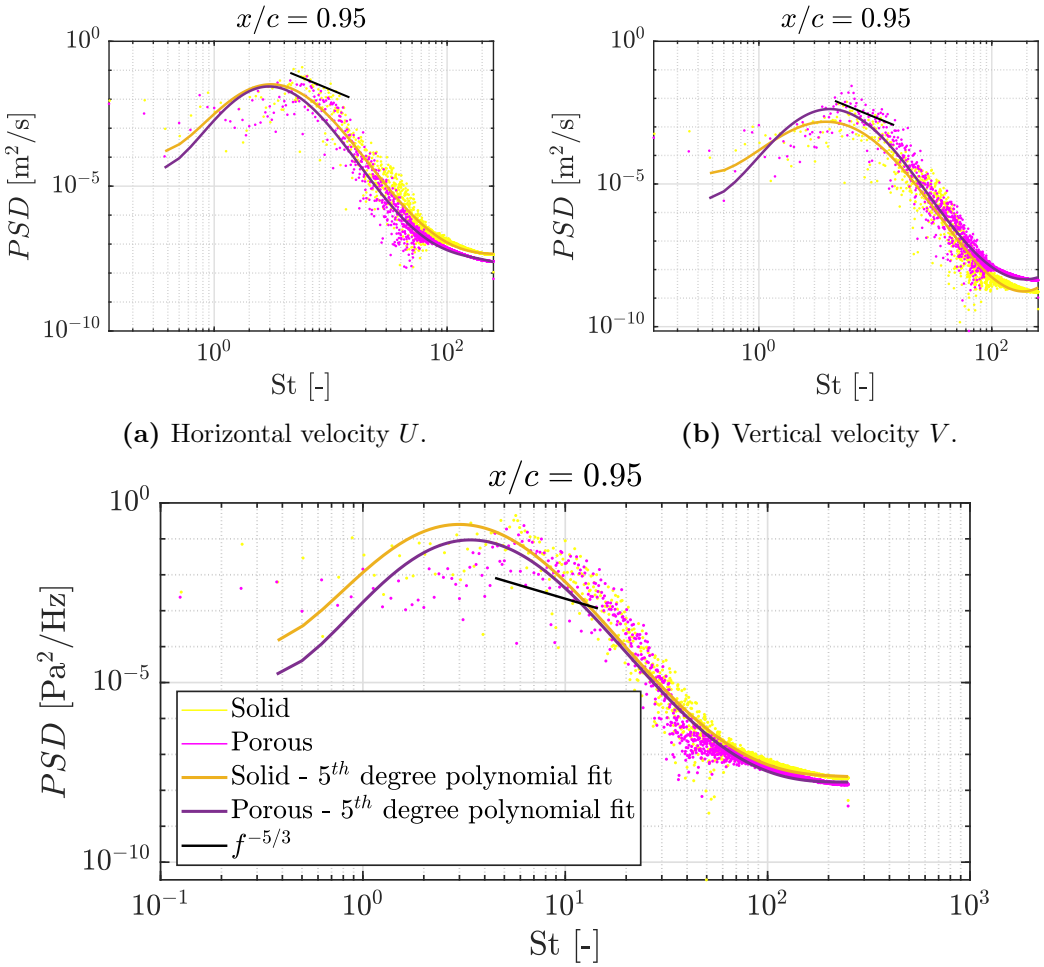

(a) Horizontal velocity U.

(b) Vertical velocity V.

(c) Pressure p.

Figure 5.15: Fast fourier transform of time signals measured at $x/c = 0.95$ plot against the chord based Strouhal number. Distance from the wall is $0.0016c$ for the solid case, and $0.0017c$ for the porous case. Time series acquired over 2 seconds between 3 and 5 seconds into the simulation.

Similar considerations can be made for the spectra of horizontal velocity and

pressure. In both cases, the porous insert reduces the spectral density along the entire frequency domain. The spectrum of wall pressure signal in the wind tunnel is discussed later in section 6.4.2.
A different trend can be seen for the spectral density of the vertical velocity signal, which is increased by the porous treatment at the high frequencies. The result for the vertical velocity is consistent with [7], while this is not the case for the horizontal velocity. This aspect could be due to the lack of skin friction in the CFD simulations.
The average off-diagonal component of the Reynolds stresses at the measurement point are summarised in Table 5.3.

Table 5.3: Average reynolds stresses at $x/c = 0.95$.

	CFD	
	Solid	Porous
$-\overline{u'v'}/U_\infty$ [-]	0.0125	0.0130

In the porous case a slightly higher $-\overline{u'v'}$ is computed.

5.4.1.4 Wake

Results for the mean flow indicated that an interesting region to compare solid and porous cases is the wake. To study the flow in this region, time signals of velocity and pressure were acquired at different locations in the wake. Storage stations were created at the chord-line ($y = 0$) for $x/c = 1.06$, 1.25, 1.6 and 2.5. The streamwise locations for solid and porous mesh differ of a maximum value of $0.04c$ at the station $x/c = 2.5$. Figure 5.16 shows the results of the frequency domain analysis performed at the storage stations. The porous insert at the trailing edge reduces the spectrum amplitude of p in the entire frequency domain. The effect is more evident in the far wake. Similar spectra are observed for the horizontal velocity, with a strong energy reduction in the far wake. Finally, the vertical velocity spectrum is the one which presents the most irregular behaviour. This could be due to the fact that the sampling time may not be enough. Overall, the porous material influences the spectra in the wake significantly.

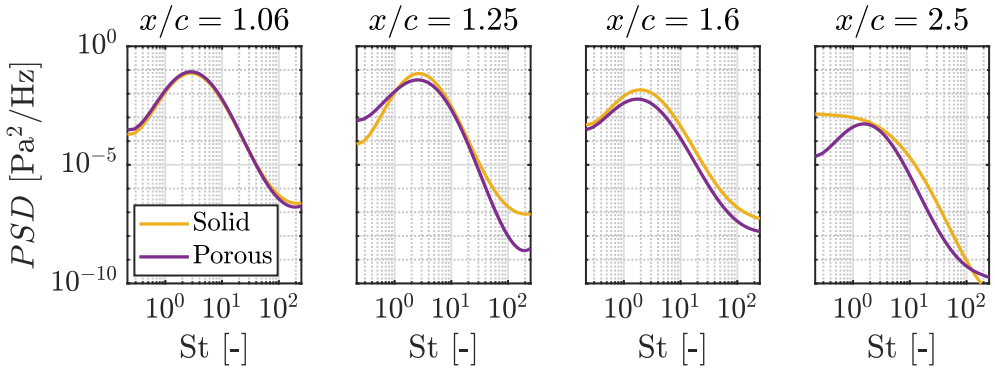

(a) Pressure.

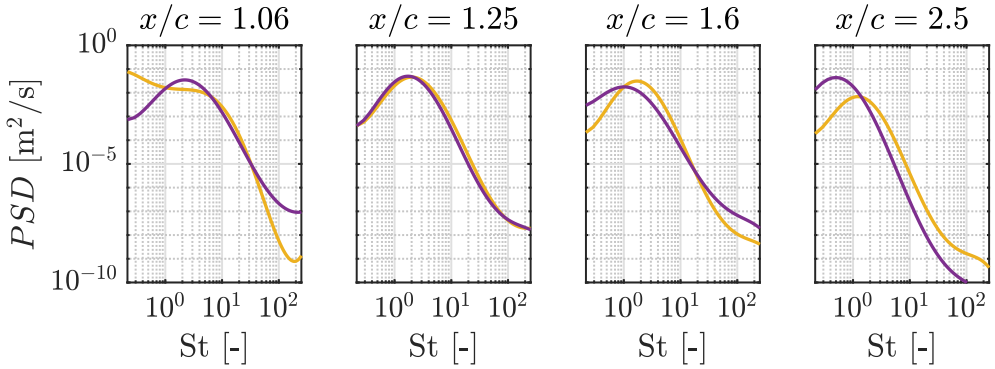

(b) Horizontal velocity.

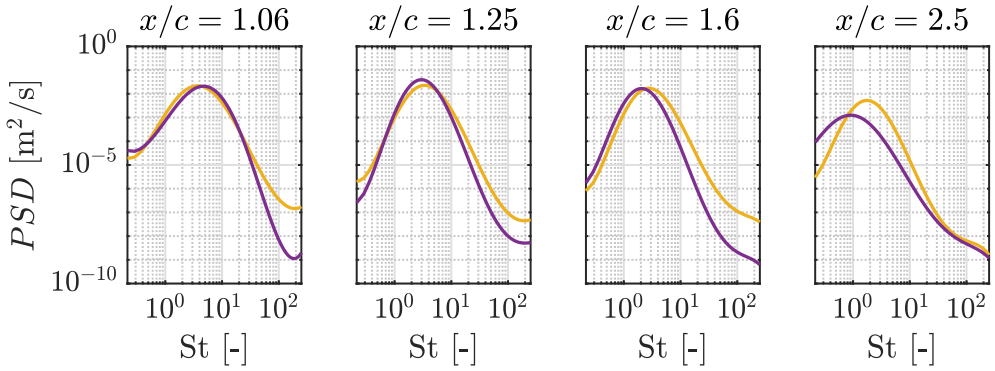

(c) Vertical velocity.

Figure 5.16: FFT of signals in the wake. 5^{th}-order polynomial fit. Solid case in yellow –, porous case in purple –. Both axis are logarithmic. The samples have been acquired and averaged over 3.48 seconds.

5.4.1.5 Trailing edge flow

In this section, the flow at the trailing edge is considered. Figure 5.17 shows the pressure field at the trailing edge for solid and porous cases.

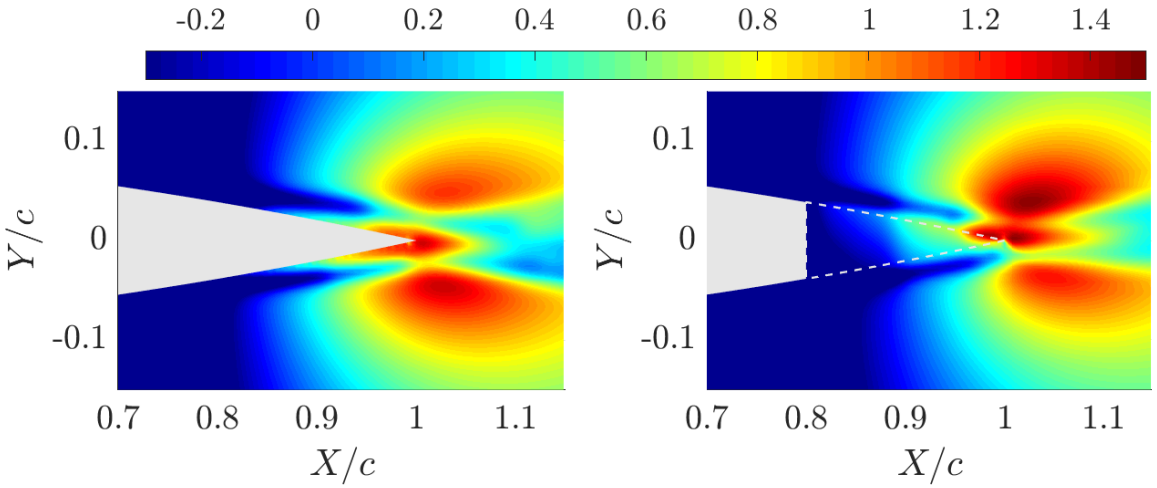

Figure 5.17: Pressure field p at the trailing edge. Solid case (left) compared with porous case (right).

This figure is significant, as it shows that a hydrodynamic field is formed inside the permeable material. This field is more articulated than the one observed for the flat plate case. Unlike this case study, it is limited to the porous trailing edge. The solid-porous interface is still acting as a solid wall. This feature in the porous case is responsible for a milder pressure discontinuity at the trailing edge, which could be responsible for the reduction of acoustic impedance.

5.4.1.6 Force coefficients

The influence of the porous materials on drag and lift for an airfoil is very important. Poor aerodynamic properties could undermine their benefits in terms of sound reduction. It is hence necessary to carefully inspect this.
Unfortunately however, `EllipSys2D` computes drag from the solid cells only. This means that when drag is computed on a partially porous body, the airfoil is considered blunt. The estimation is then wrong.
Drag coefficient was then computed from pressure. Only form drag was considered. Viscous drag was neglected. The (form) drag coefficient was computed by integrating pressure along the vertical coordinate, taking advantage of the fine

discretization used in the mesh. Pressure drag was computed as:

$$C_{D,\text{form}} = 2\,\frac{\int p dy}{0.5\rho U^2 c} \tag{5.7}$$

Given the angle of attack of zero, only one side of the airfoil was considered, and the result was doubled to account for the other side. Results are included in Table 5.4.

Table 5.4: Drag coefficient comparison between numerical results.

Solid	C_D , standard `EllipSys2D`	0.0164 [-]
Porous	C_D , standard `EllipSys2D`	0.0278 [-]
Solid	$C_{D,\text{form}}$, *p-method*	0.0062 [-]
Porous	$C_{D,\text{form}}$, *p-method*	**0.0089**[-]

The method predicts a higher drag in the porous case compared to the solid result. The significant discrepancy between *p-method* and `EllipSys2D` in the solid case is due to the lack of viscous drag, which should be predominant for an airfoil in the conditions inspected in this study. In the solid case case, the pressure drag computed with the *p-method* is 38% of the total drag from `EllipSys2D`.

5.5 Perturbed configuration

The perturbed configuration included a step at $x/c = 0.2$. It was run with different settings from the clean one. The main parameters are summarised in Table 5.5. The most relevant difference with the clean case is that the mesh is finer, with 20 additional blocks. These blocks were made necessary by the very fine mesh used to discretize the step. As a consequence of this refined mesh, the constant C_0 for LES was reduced further to 0.01.

Table 5.5: Review of main parameters used in the simulation of the NACA0018 airfoil with a roughness element to trip the boundary layer.

Chord-based Reynolds number	263,000	[-]
Free stream velocity U_∞	4	m/s
Timestep Δt	5×10^{-4}	s
Total time for averaging	4 (1.75 - 5.75)	s
Relaxation pressure α_p	0.2	[-]
Relaxation velocity α_u	0.9	[-]
Constant C_0 LES	0.01	[-]
Constant α LES	0.5	[-]
Sub-iterations	18	[-]
Kinematic viscosity ν	1.5×10^{-5}	m^2/s
Porosity ϕ	0.92	[-]
Permeability K	3.4×10^{-8}	m^2
x-location porous trailing edge	[0.8, 1]	c
Angle of attack	0	$^\circ$
Mesh blocks 64×64	80	[-]
Height first cell	1.96×10^{-4}	c
Mesh blocks in the wake (solid case)	10	[-]
Mesh blocks in the wake (porous case)	5 (TE) + 5	[-]

5.5.1 Results

5.5.1.1 Mean flow field

The mean flow field was obtained by averaging the flow over 4 seconds, between 1.75 and 5.75 seconds. The first 1.75 seconds of initial transient were neglected. The pressure coefficient along the airfoil sides is plot in Figure 5.18.

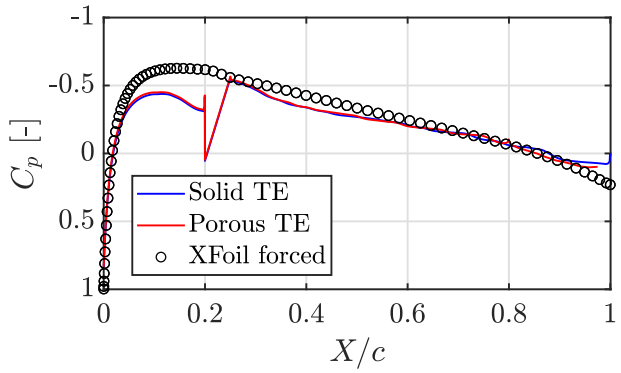

Figure 5.18: Pressure coefficient compared with XFoil (forced transition at 20%, $N_{crit} = 9$).

In the CFD results, both sides of the airfoil present the same C_p, suggesting that the mean values are converged. The discontinuity at $x/c = 0.2$ is due to the presence of the step. As observed for all cases studied so far, the highest discrepancies with XFoil are at the leading edge. The mean fields of velocity and pressure are plot in Figure 5.19.

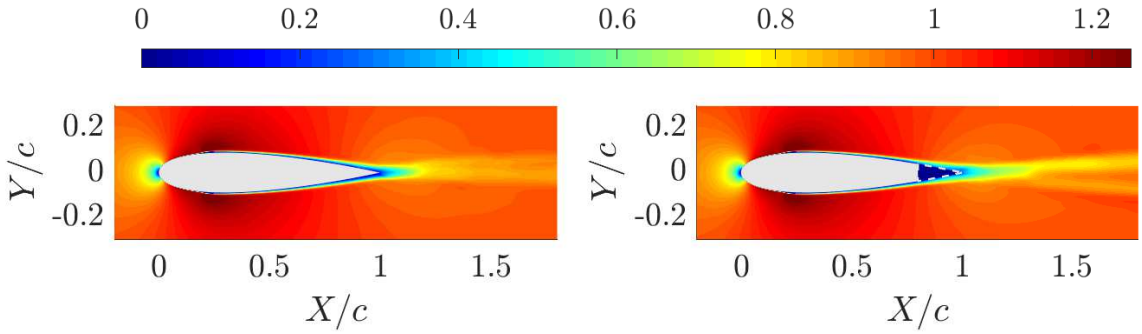

(a) Mean horizontal velocity field non-dimensionalised with U_∞.

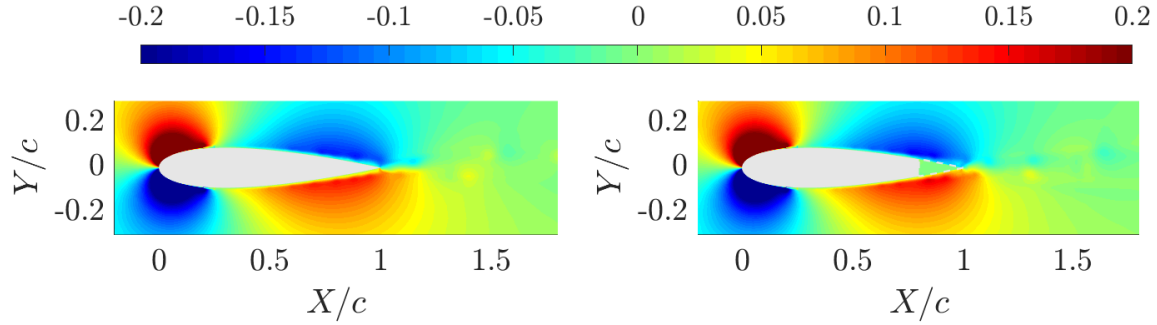

(b) Mean vertical velocity field non-dimensionalised with U_∞.

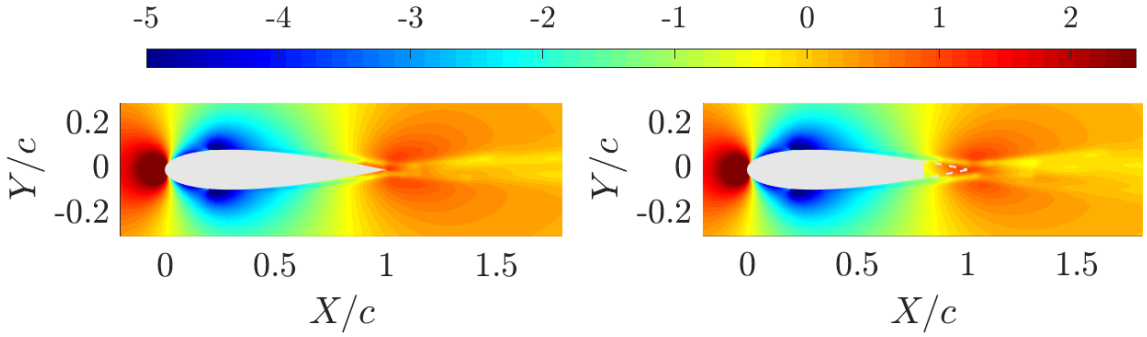

(c) Mean pressure field non-dimensionalised with the maximum field value.

Figure 5.19: Mean fields for a symmetric NACA0018 airfoil with a solid (left) and a porous (right) trailing edge. Reynolds number of 263,000.

As observed in the analysis of the pressure coefficient, the mean fields are well converged on the airfoil. However, in the wake this is still not the case. Once again, the porous insert at the trailing edge influences the wake significantly. In the plot of U/U_∞ in Figure 5.19a it can be seen that the wake deficit is enhanced by the porous material. Also, the low-velocity region extends more downstream until $X/c = 1.4$. The analysis of the results proceeds with a study of the boundary layer.

5.5.1.2 Boundary layer

The study of the boundary layer is interesting to evaluate the effects and effectiveness of the trip. The main parameters for the analysis of the boundary layer are plot along the airfoil in Figure 5.20. The mesh structure of the porous case did

not allow to extract the velocity profiles, hence in this case data are available only up to $x/c = 0.8$.

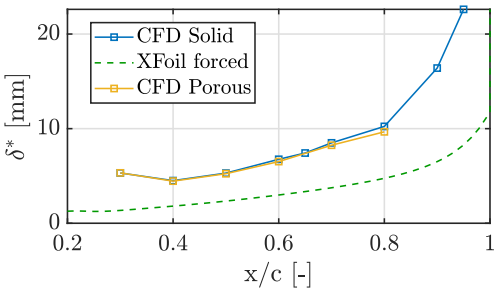

(a) Displacement thickness δ^*.

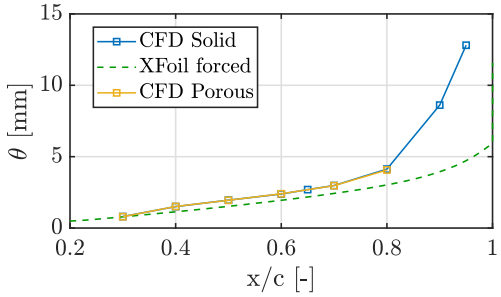

(b) Momentum thickness θ.

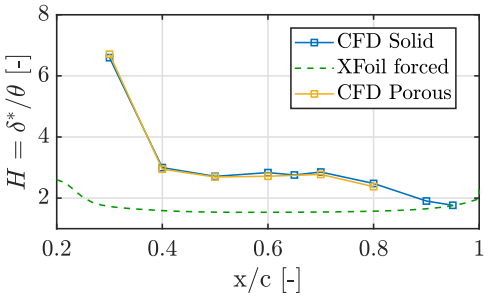

(c) Shape factor H.

Figure 5.20: Boundary layer analysis.

A very fine agreement between porous and solid case can be observed along the airfoil. This is a good aspect, as no differences are expected. Compared to the clean case, no natural transition is seen, meaning that the step is correctly forcing the flow to turbulence at $x/c = 0.2$. In the solid case, the results for δ^* and θ differ significantly from [7]. However, the shape factor is in line with this reference.

5.5.1.3 Turbulent flow field

A plot of the TI along the airfoil and in the near wake is plot in Figure 5.21.

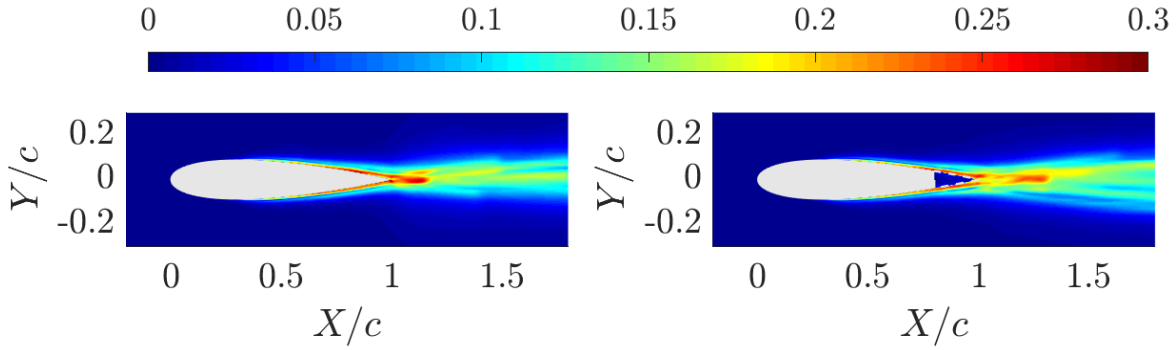

(a) U_{RMS}/U_∞

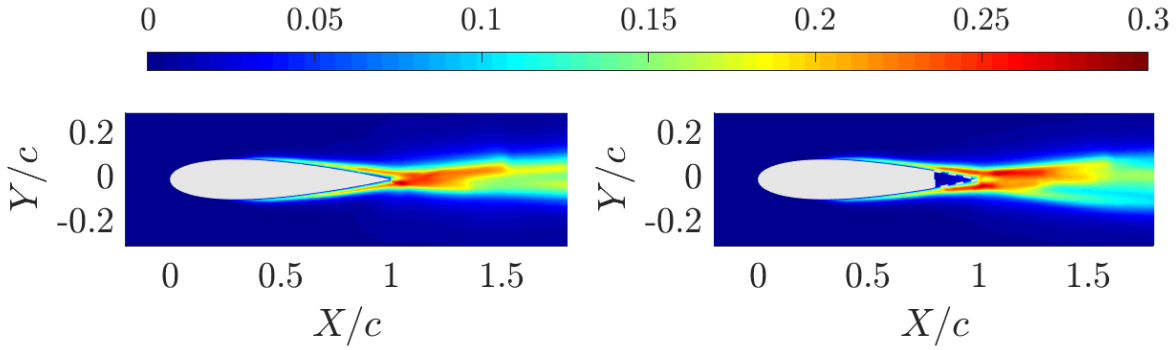

(b) V_{RMS}/U_∞

Figure 5.21: Turbulence intensity.

It can be seen that TI assumes values around 0.1 after the flow has been tripped at $x/c = 0.2$. This confirms that the trip is effective. As observed for the mean fields, the wake region is not converged. However, it can be observed that for both components of velocity, the porous material delays wake recovery.

5.5.1.4 Force coefficients

To end this chapter, results for the force coefficients are showed. The pressure method described in Section 5.4.1.6 was used once again to evaluate the form drag acting on the airfoil. As visible from the results included in Table 5.6, in the perturbed configuration $C_{D,\text{form}}$ is lower in the porous case. This is different from the results for the clean condition. In this case, the form drag computed from pressure is 59% of the total drag from `EllipSys2D`. This is due to the presence of the step for tripping.

Table 5.6: Drag coefficient comparison between numerical results.

Solid	C_D , standard `EllipSys2D`	0.0256 [-]
Solid	$C_{D,\text{form}}$, *p-method*	0.0152 [-]
Porous	$C_{D,\text{form}}$, *p-method*	**0.0126**[-]

5.6 Discussion

The main challenge of the numerical study of the airfoil case has been to set-up the computations in order to obtain meaningful results. A strong dependency on the mesh was observed with the LES turbulence model. It is very important to finely discretize the boundary layer, with at least 30 points. The mesh must be written wisely to avoid the need for too many resources. Furthermore, the right choice of LES constants is essential to obtain reliable results.

The inclusion of a roughness element in the mesh as a rectangular protrusion was used to trip the boundary layer. This configuration increased pressure drag more than 1.5 times compared to the clean configuration. Nevertheless, this trip successfully forced the flow to turbulence by strongly varying the boundary layer parameters.

Porous materials do not influence the flow upstream. Instead, they change the flow behaviour in correspondence of the trailing edge and in the wake. Once again, the presence of a hydrodynamic field inside the permeable trailing edge mitigates the pressure discontinuity. Furthermore, it alters the wake structure and increases turbulence intensity because of discharge and penetration phenomena. A strong variation on the power spectral densities of velocity and pressure is introduced with the porous media. Both in the wake and at the trailing edge wall the spectrum of pressure is reduced significantly.

Chapter 6

Experimental study

In this chapter, wind tunnel measurements on a partially porous airfoil with hot-wire anemometry and surface microphones are treated. The measurement campaign is discussed and the results are presented.

6.1 Wind tunnel set-up

The measurement campaign took place in the AV-Tunnel at the Low Speed Laboratory at TU Delft. The AV-Tunnel is a vertical, open-jet anechoic wind tunnel. It has a contraction ratio of 15:1 and a test section of 40×70 cm^2. The maximum flow speed is 45 m/s, and the turbulence level is very low, below 0.1%. A sketch of its structure is presented in Figure 6.1.

6.1.1 Model and instrumentation

An aluminum symmetric NACA 0018 airfoil was used as model. The airfoil has a chord c of 0.2 m and a span of 0.4 m. It was manufactured via Computer Numerical Control Machining and it allows the installation of different inserts at the trailing edge with a length of $0.2c$. The porous inserts are made via Electrical Discharge Machining. As this procedure does not allow to obtain long samples, three portions were assembled to fit into the trailing edge of the model. A sketch describing the model is presented in Figure 6.2. Two porous materials have been used. They have a cell diameter equal to 450 μm (MF450) and 800 μm (MF800). A porosity of 89.3% and 91.7%, and a permeability of 6×10^{-10} m^2 and 2.7×10^{-9} m^2 respectively. The insert MF800 has been used as reference for the CFD computations presented in Chapter 5.
Measurements were performed at an angle of attack of 0° . The airfoil was tripped at 20% of the chord with a 10 mm tape strip to force transition to turbulence.

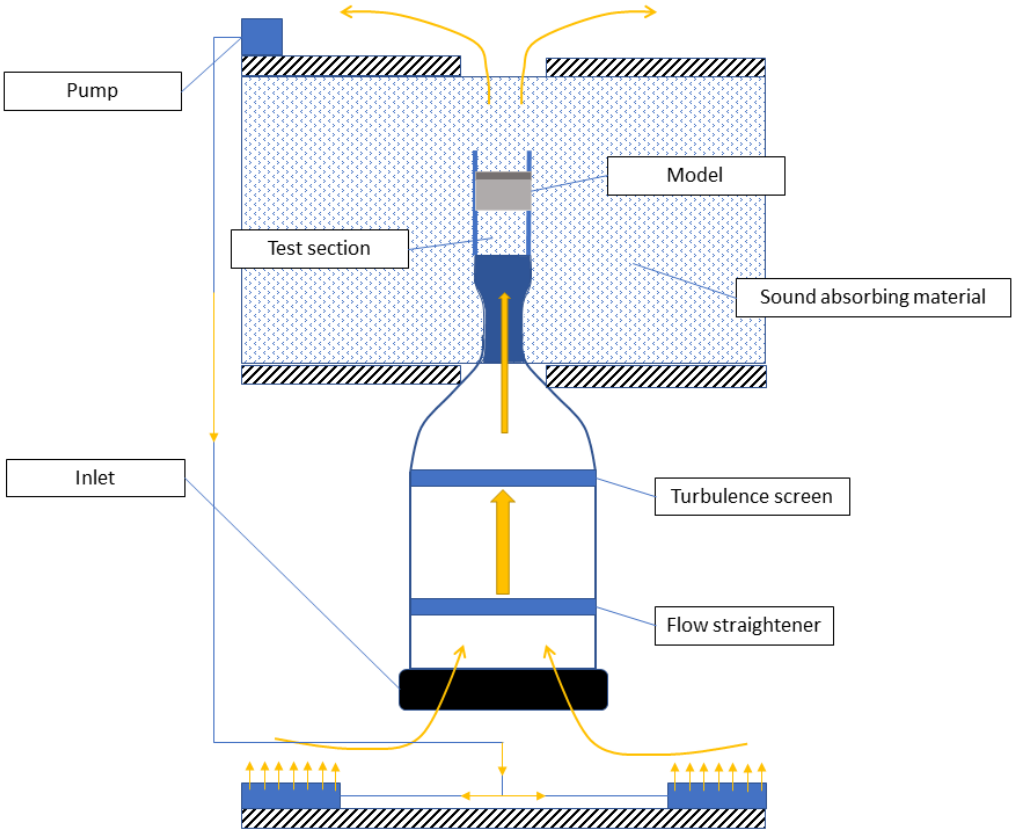

Figure 6.1: Drawing of the open-jet, vertical AV-Tunnel at TU Delft. Different floors of the *Low speed wind-tunnel Laboratory* are marked with black, diagonal lines. The ideal flow path is marked with yellow arrows.

The free-stream velocity was set to 10 m/s, leading to a chord based Reynolds number of 1.3×10^5. Clay was applied to the sides of the airfoil on the wall of the test section to ensure that no flow can get through at the wall. Tape was applied to the junction between the airfoil and the insert at the trailing edge. Surface microphones were installed on the trailing-edge insert. This was done by P.h.D. Alejandro Rubio at TU Delft to study wall-pressure fluctuations. A Pitot tube was used as a reference for the flow velocity. The hot wire probes were connected to a ZABER traverse system with a displacement accuracy of 10^{-3} mm. This system allowed to obtain measurements at different locations by moving the hot-wires automatically. The *Travsys* software was used to control the traverse system. A visual overview of the instrumentation is given in Figure 6.3, while a picture of the wind tunnel set-up is showed in Figure 6.4.

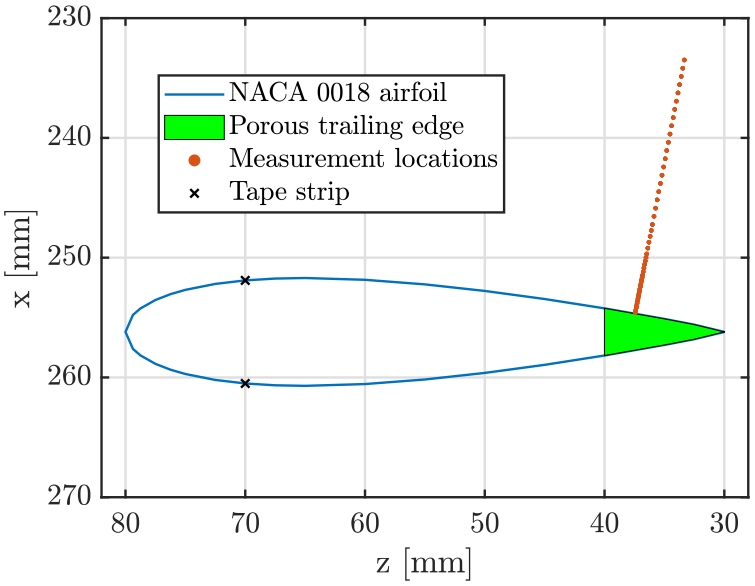

Figure 6.2: Drawing of the model used in the measurement campaign. The measurement locations of the hot-wires relatively to the airfoil are also showed in red.

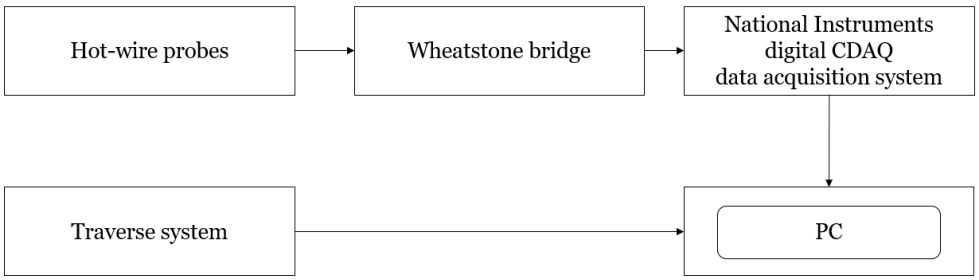

Figure 6.3: Diagram showing dependencies and connection of the tools used in the measurement campaign.

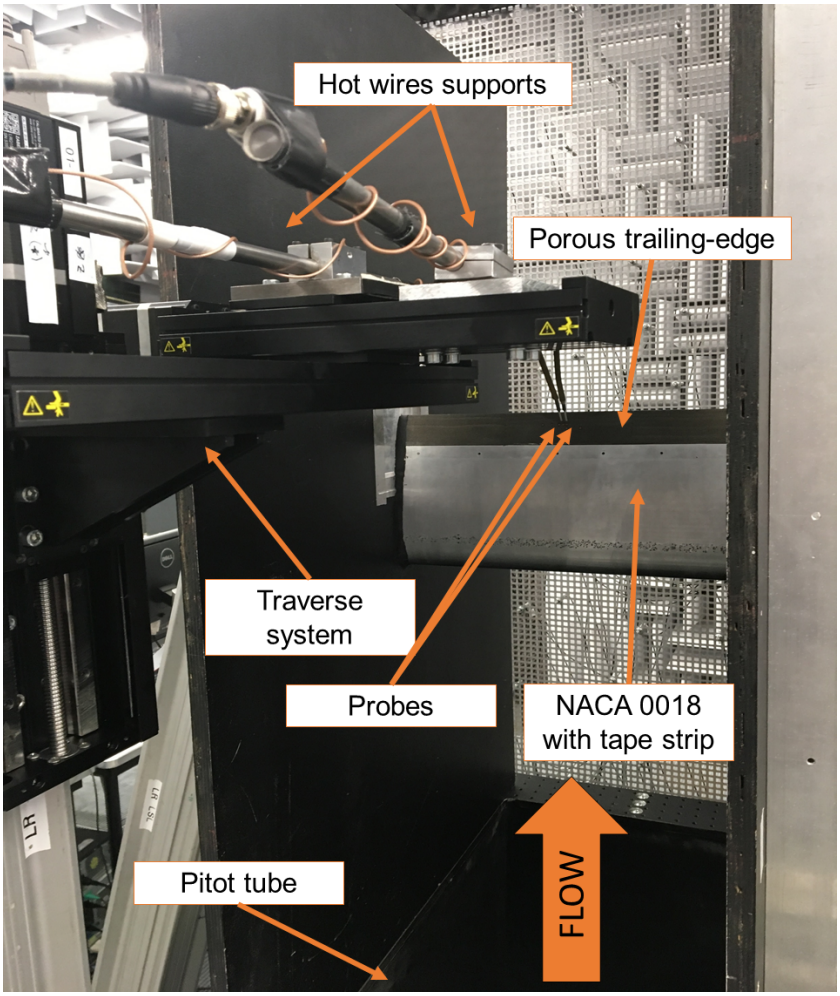

Figure 6.4: Picture of the test section between two measurement campaigns. The convergent duct of the wind tunnel lies at the bottom of the picture. The hot-wire probe on the left is free to slide in the spanwise direction. Both wires move together in the other directions.

6.1.2 Measurement techniques

6.1.2.1 Hot-wire anemometry

Hot wire anemometry is one of the most common techniques for flow measurement. It is more accurate than PIV but it requires a procedure of calibration. Two DANTEC hot wires have been used in the experiment. The reason for this is to study spanwise correlation of velocity in the post-processing phase. Because of this purpose, great attention was given to the alignment of the probes. The wires are made of platinum-plated tungsten, with a diameter of 5 micrometers and a

length of 1.25 mm. The specifics for both wires are presented in Table 6.1

Table 6.1: Specifics of the hot-wire sensors used in the measurement campaign. Hot wire 1 (HW1) is free to slide in the spanwise direction.

	HW 1 (moving)	HW 2 (fixed)
R_{20}	3.24 Ω	3.4 Ω
Operating temperature	230°	230°
Overheat ratio	0.36%	0.36%

Constant temperature anemometry is based on the fact that flow velocity can be empirically linked to the voltage reading from a hot wire. The relation is usually called King's Law, and it is presented in Equation 6.1.

$$U(E) = P_1 E^4 + P_2 E^3 + P_3 E^2 + P_4 E + P_5 \tag{6.1}$$

The probes must be calibrated evaluate the polynomial coefficients P_i. The procedure is described in Appendix D.

6.1.2.2 Surface microphones

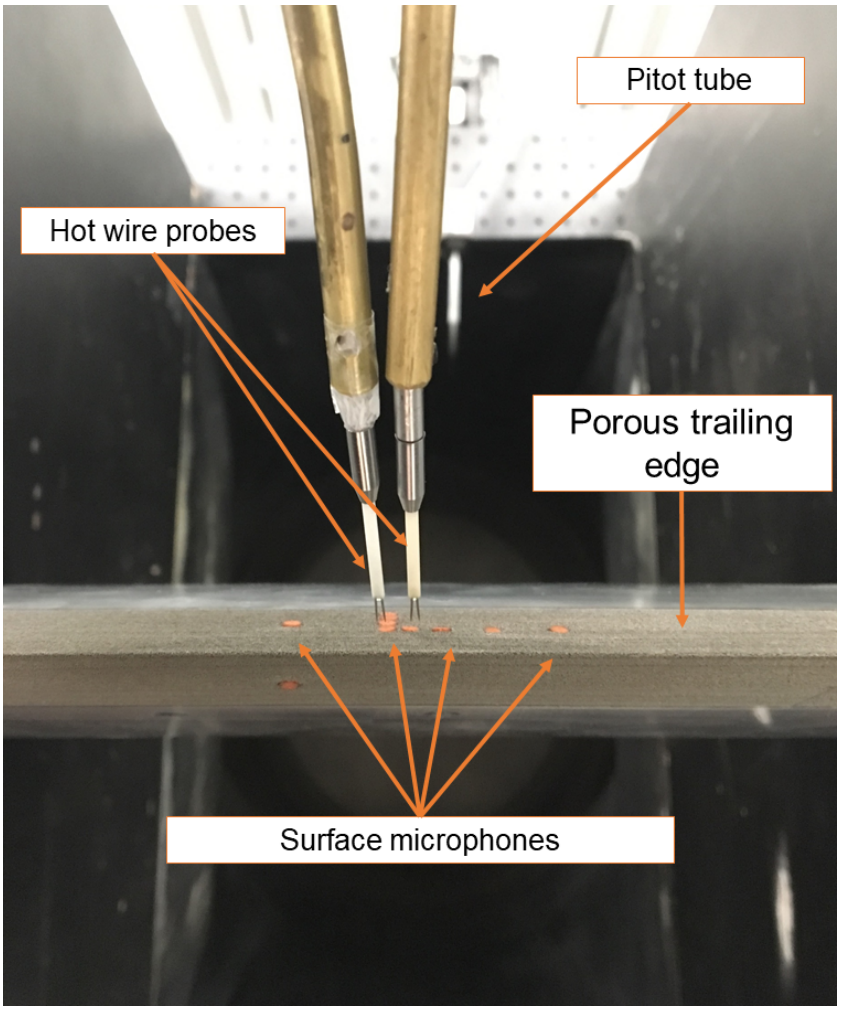

Figure 6.5: Experiment set-up. Detail of the trailing-edge region. In the current configuration, the spanwise location of the spanwise-moving probe is as close as possible to the fixed probe. The convergent duct of the wind tunnel can be seen in the background.

Some of the trailing-edge inserts used in the campaign are equipped with ten surface microphones to acquire data about wall-pressure fluctuations. The microphones were calibrated by playing two tones at 500 Hz and 2000 Hz respectively with an amplifier, as well as broadband noise to check all the frequencies lying in between. A Sonion microphone was used as reference for calibration. By measuring the voltage output at these frequencies with the SONION microphone, it is possible to evaluate the sensitivity of the surface microphones. This parameter allows to convert the signal voltage into acoustic pressure.

The SONION microphone used in the latter procedure was calibrated with a GRAS 42AA pistophone. This tool emits a signal at 250 Hz with an amplitude of 114 dB.
A sketch of the microphones location is presented in Figure 6.6.

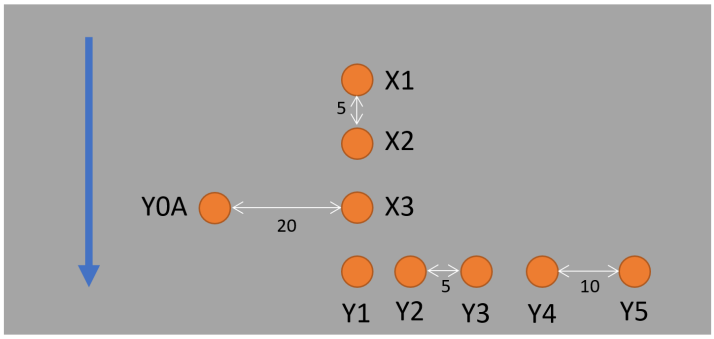

Figure 6.6: Surface microphones (in orange) location on the trailing edge insert with relative distances. Microphone *Y0B* lies on the other side of the airfoil. The flow direction is indicated by the blue arrow.

A picture showing the measurement techniques used is presented in Figure 6.5.

6.2 Measurement campaign

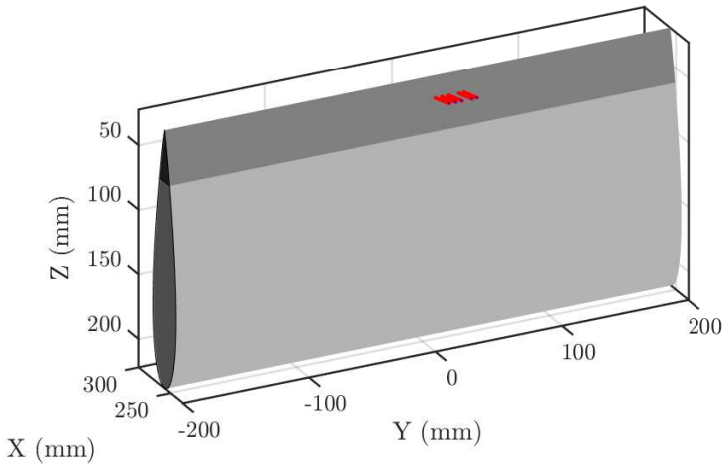

Figure 6.7: Coordinate system used in the wind tunnel to control the traverse system. The porous material is marked with a darker color. Furthermore, the locations of the hot-wire measurements are marked in red.

In order to evaluate spatial correlation, one of the two hot wires was kept at a fixed spanwise position, while the other was free to slide along the airfoil span. An illustration of the coordinate system used is presented in Figure 6.7.
Both probes were connected to the traverse so that the same displacement along x and z was followed.
The measurements were taken at a specified set of coordinates. The coordinates are also visible in detail in Figure 6.8, together with the path followed by the moving probe mounted on the traverse system. Specifically, measurements were taken perpendicularly to the airfoil trailing edge (approx. 11° inclination for NACA 0018) directly above the surface microphones. Two additional span-wise points were added. One halfway between the first two microphones, and the other where the two hot wires are as close as possible. The measurement points are more clustered towards the airfoil surface to capture the viscous effects within the boundary layer. The closest distance reached was around 1.5 mm. The sequence of measurement points was ordered so that the traverse system covers the shortest path. This is also visible in Figure 6.8.

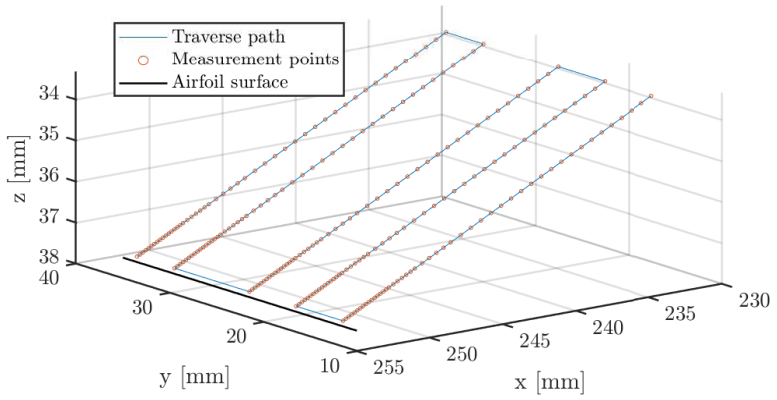

Figure 6.8: Detail of the measurement locations (orange circles) and path followed by the traverse system (blue line). The wall of the airfoil is marked by a black solid line. The hot wire number 2 lies at a fixed y location $y \approx 40$ mm (depending on the sample inspected, for which the origin of the traverse system could lie at a different locations).

6.2.1 Data acquisition

The sampling frequency was set to 51200 Hz. The acquisition of data required to synchronize LabVIEW (data management) with the software *Travsys* (control of the traverse system). The procedure is presented below.

1. A measurement point is loaded and run in *Travsys*

2. A trigger is sent from *Travsys* to LabVIEW to start the signal acquisition
3. Data are acquired for 2 seconds plus 2 other seconds of standstill
4. The traverse moves the probe to the next location

6.2.2 Corrections

Corrections are needed due to the high sensitivity of the equipment used. Specifically, if air temperature and pressure recorded during the measurement differ from those measured during probes calibration, corrections are needed. For instance, the air temperature usually differed by around 3 degrees between morning and afternoon. Once the voltage signal from the probes has reached the data acquisition system, it must be corrected to account for temperature differences

$$E = E0\sqrt{\frac{T_{wire} - T_{calibration}}{T_{wire} - T_{avg,measurement}}}$$

Air temperature in the contraction of the tunnel was recorded over 15 minutes and averaged in each measurement.
Secondly, King's Law must be applied to the corrected voltage. An additional correction to account for pressure differences between calibration conditions and measurement conditions is applied to the velocity as

$$U = U_x \frac{P_{calibration}}{P_{measurement}}$$

6.3 Data analysis

The acquired data was analysed with MATLAB. A summary of the post-processing procedure is presented:

1. Load calibration files (polynomial coefficients, room temperature and ambient pressure)
2. Load pressure and room temperature data recorded in the early phase of the measurement
3. Load traverse coordinates file
4. Load file of data acquired at one traverse location point (time,voltage from hot-wires,wall pressure from surface microphones)
    - Correct signals of pressure and velocity as showed in Section 6.2.2.

- Compute turbulence level, mean velocity and pressure correlations
- Move to the next traverse point

5. Plot the obtained values

6.4 Results

6.4.1 Mean flow

The mean, non-dimensional velocity is plotted against the non-dimensional wall-orthogonal coordinate z^+ in Figure 6.9. The non-dimensionalising process is essential to compare the results, also because of discrepancies due to the calibration of the hot-wires. To study the velocity profiles, it was chosen to use the results from the porous inserts which are not equipped with surface microphones to exclude any intrusiveness. A reduction of velocity can be observed when the porous inserts are

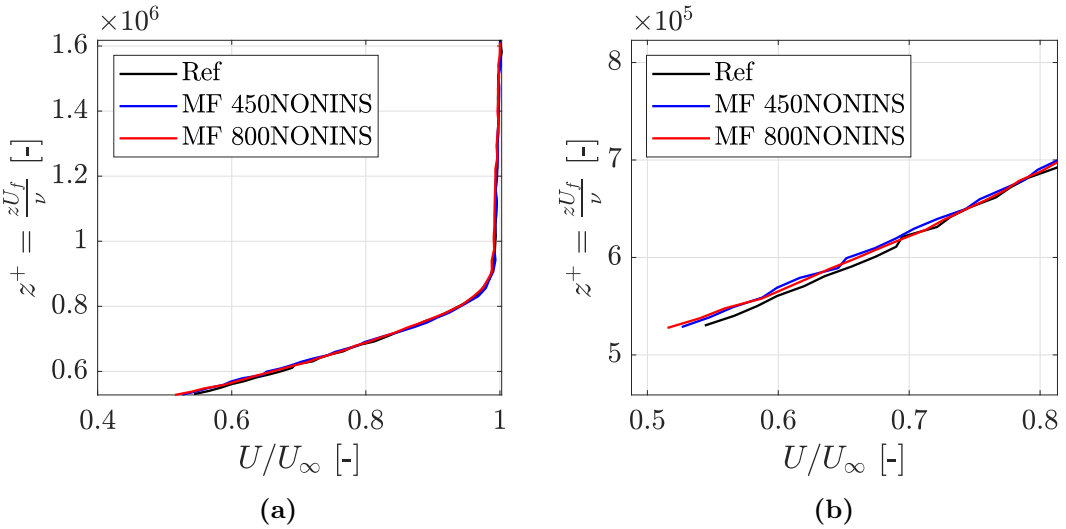

Figure 6.9: Mean wall-parallel velocity non-dimensionalised with the free-stream flow velocity, at a streamwise location of $x/c = 0.925$. The inserts used are not equipped with microphones. Solid case (—), porous case 450μm (—), porous case 800μm (—).

applied. Specifically, this phenomenon gets more evident with the trailing edge with the highest pores size (MF800). Furthermore, another interesting difference between the solid and the porous cases is the increased shear with permeable inserts. In order to quantify this, the friction velocity has been computed by fitting a line to the velocity profile close to the wall, to satisfy the logarithmic law

$$\overline{U} = A\,U_f \log(y) + B \tag{6.2}$$

with A = 2.5 [-]. The results are presented in Table 6.2.

Table 6.2: Non-dimensional friction velocity in the three cases inspected.

	U_f/U_∞ [-]
Ref	0.397
MF450	0.394
MF800	0.473

The values of friction velocity indicate that the more porous insert (MF800) increases shear significantly.

6.4.2 Turbulent flow field

The root mean square (r.m.s.) of a signal provide an estimation of its turbulence level, i.e. magnitude of the fluctuations. The r.m.s. of the wall-parallel velocity at 92.5% of the chord is presented in Figure 6.10.

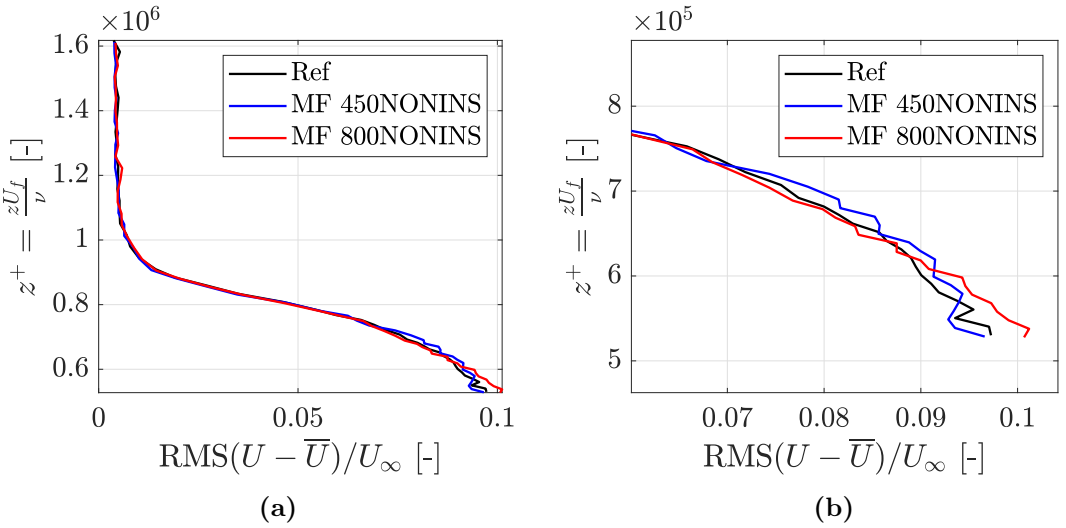

Figure 6.10: R.m.s. wall parallel velocity at $x/c = 0.925$. The MF inserts are not equipped with surface microphones. Solid case (—), porous case 450μm (—), porous case 800μm (—).

Figure 6.10 shows clearly that the r.m.s. is higher close to the wall when porous inserts are applied. The same has been found by [9], [7]. This aspect could be linked to the enhanced skin friction of a porous surface. Far from the wall, turbulence is slightly reduced by porous treatments.

Finally, a Fast Fourier Transform of pressure fluctuations measured with the surface microphones is presented in Figure 6.11.

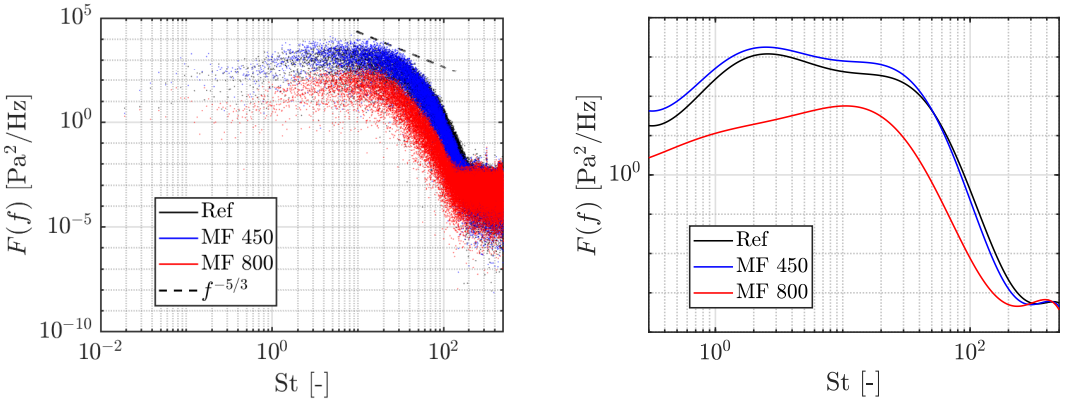

(a) Raw data. **(b)** 9^{th} order polynomial fit.

Figure 6.11: Power spectral density of wall pressure fluctuations at $x/c = 0.925$. Chord-based Strouhal number is plot on the x-axis. Acquisition frequency 51.2 kHz, Nyquist frequency 25.6 kHz. Solid case (—), porous case 450μm (—), porous case 800μm (—).

The MF800 insert reduces the power spectral density compared to the solid case in the whole frequency range. On the contrary, the MF450 insert reduces the PSD at high frequencies, while it increases it at high frequencies. The results for MF800 are consistent with the results from CFD which are presented in Section 5.4.1.3. Additional results from microphones are included in Appendix E.

6.5 Discussion

The calibration procedure of the hot-wires must be performed accurately. During the measurement campaign it was necessary to re-calibrate after any operation in the test section of the wind tunnel as well as just periodically. Near-wall flow is hard to capture with HWA and reaching locations very close to the wall can lead to the risk of breaking the sensors.
Porous material were found to increase shear of the velocity profiles in the boundary layer. Furthermore, their application reduces the spectra of wall-pressure signals at the trailing edge. This is in line with results from CFD analysis presented in Chapter 5.

Chapter 7

Conclusions and Recommendations

This chapter includes the main conclusions which can be drawn from the results.

7.1 Conclusions

The study of permeable inserts with CFD underlined some key aspects. First of all, the penalization method seems to be a vaild and promising tool to describe flows through partially porous bodies. A good agreement with wind tunnel data in the case of a flat plate was observed in terms of mean fields and forces. For a NACA0018 airfoil, the influence of porous trailing edge on turbulence predicted by CFD is in line with experimental data. The adoption of a mixed-scale subgrid model in LES introduced many challenges. The most influential parameter was the mesh, which must respect strict constraints. The application of a porous material at the trailing edge of an airfoil must go together with a trip of the boundary layer to force transition to minimize the relative increase in drag.
The measurement campaign on a NACA0018 in the wind tunnel provided results which are consistent with existing literature. Furthermore, CFD and experimental results agree on the results for turbulence.

Porous media have relevant effects on the wake and at the solid-porous interface due to flow penetration and discharge processes. In correspondence of a porous trailing edge, the power spectral density of pressure close to the wall is reduced in the whole frequency spectrum compared to a solid case. The wake structure is highly affected by the presence of porous media. This is more evident for blunt bodies. For an airfoil, porous media at the trailing edge vary the power spectral density of turbulence signals. Finally, the presence of a complex hydrodynamic

field inside the permeable media mitigates the pressure discontinuity at the trailing edge.

7.2 Future work

This work could be refined in many aspects and also extended with new proposals. First, a deeper analysis of mesh construction should be applied, to ensure independent results. A sensitivity study is essential for this purpose. Next, more computation time should be added to allow the mean fields to reach convergence in the wake.

Regarding future steps which could follow this thesis work, many activities could be done. The most obvious one is to resolve the acoustic field from the current incompressible results to quantify the emitted noise spectrum.
Next, the simulations should be extended to three-dimensions to have a more complete view over turbulence.
Finally, simulating the flow at a non-zero angle of attack would allow to evaluate the influence of the porous trailing edge on lift and glide ratio. This step is necessary to determine the range of applicability of permeable inserts to airfoils for noise reduction.

Bibliography

[1] Wind in power 2017: annual combined onshore and offshore wind energy statistics, 2018.

[2] Eja Pedersen, Jelte Bouma, R.H. Bakker, and Frits van den Berg. Response to wind turbine noise in the Netherlands. *The Journal of the Acoustical Society of America*, 123:3536, 06 2008.

[3] S Oerlemans, Pieter Sijtsma, and B Mendez Lopez. Location and quantification of noise sources on a wind turbine. *Journal of Sound and Vibration*, 299:869–883, 02 2007.

[4] Franck Bertagnolio. Trailing edge noise model applied to wind turbine airfoils. 2008.

[5] Thomas F. Brooks, Dennis Pope, and Michael A. Marcolini. Airfoil self-noise and prediction. 1218, 08 1989.

[6] B. Lyu, M. Azarpeyvand, and S. Sinayoko. Prediction of noise from serrated trailing edges. *Journal of Fluid Mechanics*, 793:556–588, 2016.

[7] Alejandro Rubio Carpio, Roberto Merino-Martinez, Francesco Avallone, Daniele Ragni, Mirjam Snellen, and Sybrand van der Zwaag. Experimental characterization of the turbulent boundary layer over a porous trailing edge for noise abatement. *Journal of Sound and Vibration*, 443, 12 2018.

[8] Thomas Geyer and E Sarradj. Trailing edge noise of partially porous airfoils. *20th AIAA/CEAS Aeroacoustics Conference, Atlanta*, 2014.

[9] Syamir Showkat Ali, Mahdi Azarpeyvand, and Carlos Silva. Trailing-edge flow and noise control using porous treatments. *Journal of Fluid Mechanics*, 850:83–119, 09 2018.

[10] J. C. Hardin and D. S. Pope. An acoustic/viscous splitting technique for computational aeroacoustics. *Theoretical and Computational Fluid Dynamics*, 6(5):323–340, Oct 1994.

[11] C. M. Rhie and W. L. Chow. Numerical study of the turbulent flow past an airfoil with trailing edge separation. *AIAA Journal*, 21(11):1525–1532, 1983.

[12] Niels N. Sørensen. *General Purpose Flow Solver Applied to Flow over Hills.* PhD thesis, 12 2003.

[13] W. Z. Shen, J. A. Michelsen, and J. N. Sorensen. Improved Rhie-Chow interpolation for unsteady flow computations. *AIAA Journal*, 39:2406–2409, 2001.

[14] H. Darcy. Les fontaines publiques de la Ville de Dijon: Exposition et application des principes a suivre et des formulesa employer dans les questions de distribution d'eau. paris. *Victor Dalmont*, 1856.

[15] J Schulze and Jörn Sesterhenn. Optimal distribution of porous media to reduce trailing edge noise. *Computers & Fluids*, 78:41–53, 04 2013.

[16] F Cimolin and Marco Discacciati. Navier–Stokes/Forchheimer models for filtration through porous media. *Applied Numerical Mathematics*, 72:205–224, 10 2013.

[17] J Lage, Bogdan Antohe, and Donald Nield. Two types of nonlinear pressure-drop versus flow-rate relation observed for saturated porous media. *Journal of Fluids Engineering*, 119, 09 1997.

[18] Ennes Sarradj and Thomas Geyer. Noise generation by porous airfoils. *13th AIAA/CEAS Aeroacoustics Conference (28th AIAA Aeroacoustics Conference), AIAA paper*, 07 2007.

[19] Charles-Henri Bruneau and Iraj Mortazavi. Numerical modelling and passive flow control using porous media. *Computers & Fluids*, 37, 08 2007.

[20] Fulvio Scarano. Experimental aerodynamics. Course reader: AE4-180 Flow Measurement Techniques, February 2013.

[21] F. Thauvin and K. K. Mohanty. Network modeling of non-darcy flow through porous media. *Transport in Porous Media*, 31(1):19–37, Apr 1998.

[22] P. Sagaut. *Large Eddy Simulation for Incompressible Flows.* Springer-Verlag Berlin Heidelberg, 2006.

[23] Wen Zhong Shen, Weijun Zhu, and Jens Nørkær Sørensen. Aeroacoustic computations for turbulent airfoil flows. *AIAA Journal*, 47(6):1518–1527, 2009.

[24] Stephen B. Pope. *Turbulent Flows*. Cambridge University Press, 2000.

[25] B. Mutlu Sumer. *Lecture Notes on Turbulence*. Technical University of Denmark DTU Mekanik, Section for Fluid Mechanics, Coastal Maritime Engineering Building 403, 2800 Lyngby, Denmark, bms@mek.dtu.dk.

[26] Huai Xiaoli, David. Ronald, and Piomelli Ugo. Large-eddy simulation of transition to turbulence in boundary layers. 1997.

[27] Wen Zhong Shen and Wei Jun Zhu. Aeroacoustic computations for turbulent airfoil flows. *AIAA Journal*, 47:1518–1527, 06 2009.

Appendix A

Mesh orthogonality

In this appendix, the procedure to obtain wall-orthogonal mesh lines is presented and derived. This method was implemented in `MATLAB` to generate the mesh.
A sketch of the geometry is presented in Figure A.1. The series of points in blue represent one wall of known points (i.e. belonging to the solid body). The procedure below allows to find the coordinates of the orange points so that the grey lines joining blue and adjacent orange points are perpendicular to the blue perimeter. Given points d, c, and u belonging to a set of points, the line orthogonal

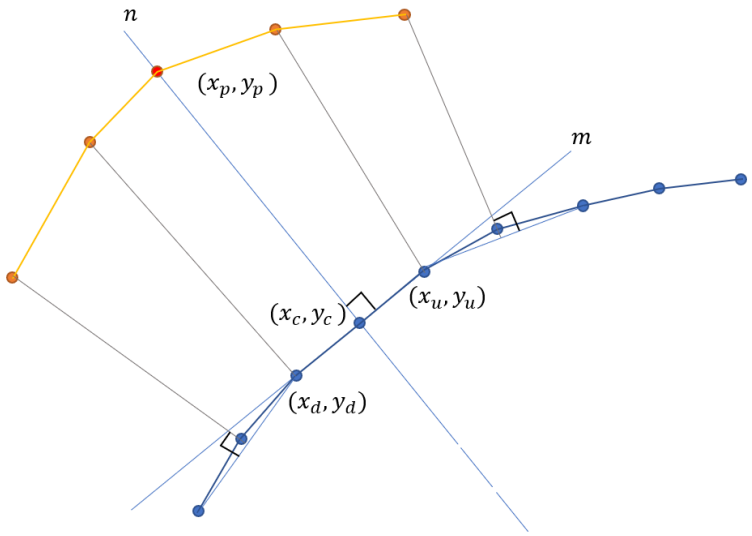

Figure A.1: Sketch to present the criteria used for mesh orthogonality.

to the wall in point c is passing through point p and point c. Point c lies on the line perpendicular to the line passing through the closest neighbour points d and

u. In the code, the coordinate y_p is given from a linear scaling of y_c. x_p can be found from the definition of orthogonality with the scalar product. If the two perpendicular lines are marked as m and n respectively, we have that

$$\langle m, n \rangle = 0$$

with $m = (x_u - x_d, y_u - y_d)$ and $n = (x_p - x_d, y_p - y_d)$. By inserting the points coordinates, we obtain that

$$\langle (x_u - x_d, y_u - y_d), (x_p - x_d, y_p - y_d) \rangle = 0$$

$$x_p - x_d = \frac{(y_u - y_d)(y_p - y_d)}{x_u - x_d}$$

$$x_p = \frac{(y_u - y_d)(y_p - y_d)}{x_u - x_d} + x_d$$

At the extreme boundaries of the wall, point u (or d) is replaced with point c.

Once the coordinates of point p have been found, a correction must be applied to ensure a constant spacing between the corrected p^* and c, i.e. R.
Line n can be described as

$$(y_c - y_p) = m(x_c - x_p) + q \tag{A.1}$$

with m the slope, and q the y-intercept.
The slope of a line passing by two points c and p^* is computed as

$$m = \frac{y_{p^*} - y_c}{x_{p^*} - x_c} \tag{A.2}$$

The y-intercept is instead computed as

$$q = \frac{x_{p^*} y_c - x_c y_{p^*}}{x_{p^*} - x_c} \tag{A.3}$$

To compute the corrected coordinates x_{p^*} and y_{p^*}, a constant distance R between c and p^* is imposed with the Pythagorean theorem

$$(y_{p^*}(x_{p^*}) - y_c)^2 + (x_{p^*} - x_c)^2 = R^2 \tag{A.4}$$

$$y_{p^*}^2 + y_c^2 - 2y_{p^*} y_c + x_{p^*}^2 + x_c^2 - 2x_{p^*} x_c = R^2 \tag{A.5}$$

y_{p^*} can be expressed as a function of x_{p^*} as

$$y_{p^*} = m x_{p^*} + q \tag{A.6}$$

with m and q previously evaluated from Equations A.2 and A.3 respectively. x_{p^*} can be computed if Equation A.6 is plugged in Equation A.5

$$m^2 x_{p^*}^2 + q^2 + 2mqx_{p^*} + y_c^2 - 2y_c(mx_{p^*} + q) + x_{p^*}^2 + x_c^2 - 2x_{p^*}x_c = R^2 \tag{A.7}$$

Isolating the quadratic and the linear terms leads to

$$(m^2 + 1)x_{p^*}^2 + (2mq - 2x_c - 2y_c m)x_{p^*} = R^2 - q^2 - y_c^2 + 2y_c q - x_c^2 \tag{A.8}$$

Equation A.8 is a second order equation. Written in canonical form, we obtain

$$(m^2 + 1)x_{p^*}^2 + (2mq - 2x_c - 2y_c m)x_{p^*} - R^2 + q^2 + y_c^2 - 2y_c q + x_c^2 = 0 \tag{A.9}$$

Equation of the kind $ax^2 + bx + c = 0$ can be solved for x using Equation A.10

$$x_{1,2} = \frac{-b \pm \sqrt{b^2 - 4ac}}{2a} \tag{A.10}$$

In our case we have that

$$\begin{aligned} a &= m^2 + 1 \\ b &= 2mq - 2x_c - 2y_c m \\ c &= q^2 + y_c^2 - R^2 - 2y_c q + x_c^2 \end{aligned}$$

Two solutions for x_{p^*} will be obtained. Only the solutions lying in the desired region of the leading edge area are kept. The relative y_{p^*} coordinate is computed from Equation A.6.

$$\boxed{x_{p^*1,2} = \frac{-mq + x_c + y_c m \pm \sqrt{2y_c x_c m - 2mqc_c + R^2 m^2 - x_c^2 m^2 - q^2 - y_c^2 + R^2 + 2qy_c}}{m^2 + 1}} \tag{A.11}$$

Appendix B

MATLAB code for mesh generation

This appendix includes codes and functions used in `MATLAB` to generate the mesh. *main.f* is the main script, *orto_mesh.m* is a function to compute the scalar product, *NACA_4digits generates airfoil coordinates of the NACA 4 digits kind, and eventually Storage65.m* is used to store the mesh points according to `EllipSys2D`.

main.m

```
close all
clear all
clc

A = load('NACA0018_coord.txt'); % load coordinates airfoil
xx = A(:,1);
yy = A(:,2);

t= 18/100;

X_LE_n = (1-(sin(linspace(0,pi/2-0.00325,64*8))))*0.3;
Y_LE_n = NACA_4digits(X_LE_n,t);

X_LE = [(X_LE_n) fliplr(X_LE_n)];
Y_LE = [-(Y_LE_n) fliplr(Y_LE_n)];

X_body_n = linspace(0.3,0.8,64*10+1);
Y_body_n = NACA_4digits(X_body_n,t);
```

```
19
20 X_body = [fliplr(X_body_n) X_body_n];
21 Y_body = [-fliplr(Y_body_n) Y_body_n];
22
23 X_TE_n = (sin(linspace(0,asin(1),65)))*0.2+0.8;
24 Y_TE_n = NACA_4digits(X_TE_n,t);
25
26 X_TE = [fliplr(X_TE_n) X_TE_n];
27 Y_TE = [-fliplr(Y_TE_n) Y_TE_n];
28
29 X_prof = [fliplr(X_body_n(1:end-1)) X_LE_n(2:end) fliplr(
       X_LE_n(2:end)) X_body_n(1:end-1) ];
30 Y_prof = [-fliplr(Y_body_n(1:end-1)) -Y_LE_n(2:end) fliplr(
       Y_LE_n(2:end)) Y_body_n(1:end-1) ];
31
32 X_blunt = X_prof;
33 Y_blunt = Y_prof;
34 index = find(X_prof>0.8);
35 X_blunt(index) = [];
36 Y_blunt(index) = [];
37
38 X_blunt = [0.8 X_blunt 0.8];
39 Y_blunt = [0 Y_blunt 0];
40
41 %% Mesh Leading Edge - region 1
42 stretcher_tanh = 5; % stretching parameter
43 R_LE = 10;          % mesh extension/height
44
45 % determine spacing of stretching function at the wall
46 auto_dist = [(1-tanh(linspace(0,stretcher_tanh,64)))*R_LE];
47 base_4_interpol = auto_dist(end)-(auto_dist(end-1)-
       auto_dist(end));
48
49 % create a layer of points within the boundary layer with
50 %  slight stretching (cosine function)
51 BL_m = linspace(base_4_interpol*1.6,0.006,32);
52 parameter = 0.485;
53 dist1 = BL_m(end)-BL_m(1);
54 BL_m = (1-cos(linspace(-pi/2+parameter,0-parameter,32)))
55 BL_m = BL_m-min(BL_m);
```

```
56 BL_m = BL_m/max(BL_m);
57 BL_m = BL_m*(dist1*1.9)+9.5e-4;
58 BL_m = fliplr(BL_m);
59
60 buffer = 5.5e-4;
61
62 semiax = max(X_LE);
63 semiay = 0;
64
65 % Outer perimeter mesh leading edge
66 Y_perimeter = Y_LE/0.3*35;
67
68 % Obtain orthogonal mesh points to the leading edge
69 for i = 1:length(Y_perimeter)/2
70     if i == 1
71         X_perimeter(i) = orto_mesh(X_LE(2),X_LE(1),Y_LE(2),
              Y_LE(1),Y_perimeter(1)-Y_LE(1));
72     elseif i == length(Y_perimeter)/2
73         X_perimeter(i) = orto_mesh(0,X_LE(length(
              Y_perimeter)/2-1),0,Y_LE(length(Y_perimeter)
              /2-1),Y_perimeter(length(Y_perimeter)/2)-Y_LE(
              length(Y_perimeter)/2-1));
74     else
75         X_perimeter(i) = orto_mesh(X_LE(i+1),X_LE(i-1),Y_LE
              (i+1),Y_LE(i-1),Y_perimeter(i)-Y_LE(i-1));
76     end
77 end
78
79 X_perimeter(1) = (X_perimeter(2)+X_body_n(1))/2;
80
81 % Correction
82 for i = 1:length(X_perimeter)
83     [m,q] = linea(X_perimeter(i),Y_perimeter(i),X_LE(i),
          Y_LE(i));
84     a = m^2 + 1;
85     b = 2*m*q - 2*X_LE(i) - 2*Y_LE(i)*m;
86     c = q^2 + Y_LE(i)^2 - R_LE^2 - 2*Y_LE(i)*q + X_LE(i)^2;
87     X_perimeter(i) = (-b-sqrt(b^2-4*a*c))/(2*a);
88     Y_perimeter(i) = m*X_perimeter(i) + q;
89 end
```

```
90
91  X_perimeter(length(Y_perimeter)/2+1:length(Y_perimeter)) =
        fliplr(X_perimeter(1:length(Y_perimeter)/2));
92  Y_perimeter(length(Y_perimeter)/2+1:length(Y_perimeter)) =
       -fliplr(Y_perimeter(1:length(Y_perimeter)/2));
93
94  B = [X_LE; X_perimeter];
95  C = [Y_LE; Y_perimeter];
96
97  % Generate mesh at the leading edge
98  gessiX = interp1([base_4_interpol R_LE],B,[-buffer+max(BL_m
        )+(1-tanh(linspace(0,stretcher_tanh,32)))*(R_LE-max(BL_m
        )) fliplr(BL_m)],'linear');
99  gessiY = interp1([base_4_interpol R_LE],C,[-buffer+max(BL_m
        )+(1-tanh(linspace(0,stretcher_tanh,32)))*(R_LE-max(BL_m
        )) fliplr(BL_m)],'linear');
100
101 % Include centerline
102 adjo = interp1([base_4_interpol R_LE],[min(X_LE); min(
        X_perimeter)],[-buffer+max(BL_m)+(1-tanh(linspace(0,
        stretcher_tanh,32)))*(R_LE-max(BL_m)) fliplr(BL_m)],'
        linear');
103
104 gessiX1 = [(gessiX(:,1:size(gessiX,2)/2)) adjo'];
105 gessiX2 = [adjo' (gessiX(:,size(gessiX,2)/2+1:end))];
106
107 gessiY1 = [(gessiY(:,1:size(gessiY,2)/2)) zeros(size(gessiY
        ,1),1)];
108 gessiY2 = [zeros(size(gessiY,1),1) (gessiY(:,size(gessiY,2)
        /2+1:end))];
109
110 % Include wall
111 gessiY1 = [gessiY1; (Y_LE(1:length(Y_LE)/2)) 0];
112 gessiY2 = [gessiY2; 0 (Y_LE(length(Y_LE)/2+1:end))];
113
114 gessiX1 = [gessiX1; (X_LE(1:length(X_LE)/2)) 0];
115 gessiX2 = [gessiX2; 0 (X_LE(length(X_LE)/2+1:end))];
116
117 %% Mesh Main Body - region 2
118 X_top = linspace(0.3,4,length([X_body_n]));
```

```
119 Y_aux = NACA_4digits(linspace(0.3,0.4,length(X_top)),1/100)
    ;
120 Y_aux = Y_aux/(Y_aux(1))*max(Y_perimeter);
121 Y_top = ones(1,length(Y_aux))*max(gessiY(:));
122
123 % Generate orthogonal mesh lines
124 for i = 1:length(Y_aux)
125     if i == 1
126         X_top(i) = orto_mesh(X_body_n(2),X_body_n(1),
                Y_body_n(2),Y_body_n(1),max(gessiY(:))-Y_body_n
                (1));
127     elseif i == length(Y_aux)
128         X_top(i) = orto_mesh(X_body_n(end),X_body_n(end-1),
                Y_body_n(end),Y_body_n(end-1),max(gessiY(:))-
                Y_body_n(end));
129     else
130         X_top(i) = orto_mesh(X_body_n(i+1),X_body_n(i-1),
                Y_body_n(i+1),Y_body_n(i-1),max(gessiY(:))-
                Y_body_n(i-1));
131     end
132 end
133 X_top(1) = (X_top(2)+X_perimeter(1))/2;
134
135 % Generate grid
136 X_B_top = interp1([base_4_interpol R_LE],[X_body_n; X_top
    ],[-buffer+max(BL_m)+(1-tanh(linspace(0,stretcher_tanh
    ,32)))*(R_LE-max(BL_m)) fliplr(BL_m)],'linear');
137 Y_B_top = interp1([base_4_interpol R_LE],[Y_body_n; Y_top
    ],[-buffer+max(BL_m)+(1-tanh(linspace(0,stretcher_tanh
    ,32)))*(R_LE-max(BL_m)) fliplr(BL_m)],'linear');
138 Y_B_bot = interp1([R_LE base_4_interpol],[-Y_top ; -
    Y_body_n ],fliplr([ -buffer+max(BL_m)+(1-tanh(linspace
    (0,stretcher_tanh,32)))*(R_LE-max(BL_m)) fliplr(BL_m)]),
    'linear');
139 X_B_bot = interp1([R_LE base_4_interpol],[X_top;    X_body_n
      ],fliplr([ -buffer+max(BL_m)+(1-tanh(linspace(0,
    stretcher_tanh,32)))*(R_LE-max(BL_m)) fliplr(BL_m)]),'
    linear');
140
141 Y_B_top = [Y_B_top;
```

```
142                 Y_body_n ];
143 Y_B_bot = [-Y_body_n;
144                 Y_B_bot ];
145 X_B_top = [X_B_top;
146                 X_body_n ];
147 X_B_bot = [X_body_n ;
148                 X_B_bot];
149
150 % Junction between LE and Body meshes
151 gessiY2(:,end) = Y_B_top(:,1);
152 gessiY1(:,1)   = -Y_B_top(:,1);
153
154 gessiX2(:,end) = X_B_top(:,1);
155 gessiX1(:,1)   = X_B_top(:,1);
156 %% Mesh wake - region 4
157 % Localize mesh start
158 wake_X = X_B_top(:,end);
159 wake_Y = Y_B_top(:,end);
160
161 Y_end = cos(linspace(acos(min(wake_Y)),acos(max(wake_Y)),
        length(wake_Y)));
162 Y_end = real(Y_end);
163 Y_end = fliplr(Y_B_top(:,end)');
164
165 stretcher_tanh_wake = 3.61; % stretching parameter
166 blk_wk = 4; % mesh blocks within the wake
167
168 auto_dist = [(1-tanh(linspace(0,stretcher_tanh_wake,64*
        blk_wk)))*R_LE];
169 basis_wake_inter = auto_dist(end)-(auto_dist(end-1)-
        auto_dist(end));
170
171 offset = 0.2;
172
173 % Generate mesh in the wake
174 W_Y_U = interp1([basis_wake_inter R_LE],[wake_Y'; fliplr(
        Y_end)],[(1-tanh(linspace(0,stretcher_tanh_wake,64*
        blk_wk)))*R_LE],'linear');
175 W_X_U = interp1([basis_wake_inter R_LE],[offset+wake_X';
        ones(1,length(wake_X))*20],[(1-tanh(linspace(0,
```

```
    stretcher_tanh_wake,64*blk_wk)))*R_LE],'linear');
W_Y_D = interp1([basis_wake_inter R_LE],[-wake_Y'; fliplr(-
    Y_end)],[(1-tanh(linspace(0,stretcher_tanh_wake,64*
    blk_wk)))*R_LE],'linear');

W_X_U = [W_X_U; offset+wake_X'];
W_Y_U = [W_Y_U; wake_Y'];
W_Y_D = [W_Y_D; -wake_Y'];
%% Mesh porous area - region 3
X_ext = W_X_U(:,end);

spacing = 0.09;
auxilium =  cos(linspace(-pi+spacing,0-spacing,65));
Y_ext = fliplr(auxilium./max(auxilium)*min(W_Y_U(:)));

[X_S,Y_S] = meshgrid(X_ext,Y_ext);

% Generate mesh above and below blunt trailing edge
W_Y_UP = interp1([-R_LE R_LE],[wake_Y'; W_Y_U(end,:)],
    linspace(-R_LE,R_LE,64*4+1),'linear');
W_X_UP = interp1([-R_LE R_LE],[wake_X'; W_X_U(end,:)],
    linspace(-R_LE,R_LE,64*4+1),'linear');
W_Y_DP = interp1([-R_LE R_LE],[-wake_Y'; -W_Y_U(end,:)],
    linspace(-R_LE,R_LE,64*4+1),'linear');
W_X_DP = interp1([R_LE -R_LE],[wake_X'; W_X_U(end,:)],
    fliplr(linspace(-R_LE,R_LE,64*4+1)),'linear');

% Center wake porous area
X_grid = flipud(W_X_UP(:,end));
Y_grid = Y_ext;

% Generate uniform mesh in the porous region
[X_grid_TE,Y_grid_TE] = meshgrid(X_grid,Y_grid);
%% Storage ...
% Wake bottom
WD = flipud(storage65(fliplr(W_X_U),fliplr(W_Y_D)));
% Wake up
WU = flipud(storage65((W_X_U),(W_Y_U)));
% Wake little uniform bottom
WDP = (storage65((W_X_DP),(W_Y_DP)));
```

```
209 % Wake little uniform up
210 WUP = (storage65(fliplr(W_X_DP),fliplr(W_Y_UP)));
211 % Body center bottom
212 BB = storage65((X_B_top'),(-Y_B_top'));
213 % Body center up
214 BU = storage65((X_B_bot'),(-Y_B_bot'));
215 % Wake center
216 WC = flipud(storage65((X_S'),(Y_S')));
217 % Wake center porous
218 WCP = flipud(storage65((X_grid_TE'),(Y_grid_TE')));
219 % Leading edge 1
220 NA1 = storage65((fliplr(gessiX1')),(fliplr(gessiY1')));
221 % Leading edge 2
222 NA2 = storage65((fliplr(gessiX2')),(fliplr(gessiY2')));
223
224 % Generate array with coordinates to be saved later
225 xy = [flipud(WD); flipud(WDP); flipud(BB); NA1; NA2; BU;
      WCP; WUP; WC; WU];
226 %% Attributes
227 attributes = zeros(length(xy),1);
228
229 ix = xy(:,1);
230 iy = xy(:,2);
231
232 disp('Placing attributes...')
233
234 % Outflow attributesibute 401
235 co40 = find(ix == max(W_X_U(:)));
236 attributes(co40) = 401;
237
238 % Inflow attributesibute 201
239 co31 = find(iy <= max(Y_end)+10 & iy > (Y_end(end-1)) & ix
      >=5);
240 co32 = find(iy >= -max(Y_end)-10 & iy < (-Y_end(end-1)) &
      ix>=5);
241 co33 = find(ismember(iy,Y_B_top(1,:)));
242 co34 = find(ismember(iy,-Y_B_top(1,:)));
243 attributes([co31' co32' co33' co34']) = 201;
244
```

```
co20 = find(ismember(ix,[gessiX(1,:)]) & ismember(iy,[
    gessiY(1,:)]));
attributes(co20) = 201;

% Porous attributesibute 51
co51 = find(inpolygon(ix,iy,X_TE,Y_TE) == 1);
attributes(co51) = 51;

% Wall attributesibute 101
co10 = find(ix >= 0 & ix <=1 & iy < 0.091 & iy > -0.091 &
    ...
                (ismember(ix,[1 X_blunt ])==1 & ismember(iy,[0
                    Y_blunt ])==1));
co11 = find(ix==0 & iy ==0);
co112 = find(ix == 0.8 & ismember(iy,Y_S(:,end))==1);
attributes([co10; co11; co112]) = 101;

% Save file
dlmwrite('mesh_naca0018.txt',pluto,'delimiter','\t','
    precision',9)
```

orto_mesh.m

```
function [xm] = orto_mesh(xau,xap,yau,yap,ym)

ya = yau-yap;
xa = xau-xap;

xm = -ya.*ym./xa + xap;

end
```

NACA_4digits.m

```
function [y] = NACA_4digits(x,t,blunt)
if blunt == 0
    y = 5*t*(0.2969*sqrt(x)-0.1260*x-0.3516*x.^2+0.2843*x
        .^3-0.1036*x.^4); % sharp
else
    y = 5*t*(0.2969*sqrt(x)-0.1260*x-0.3516*x.^2+0.2843*x
        .^3-0.1015*x.^4); % blunt
```

```
end
```

Storage65.m

```
function [X] = storage65(mx,my)
bsize = 64;
p = 1;

for j = 1:bsize:size(mx,2)-bsize
    for i = 1:bsize:size(mx,1)-bsize
        cooEX = mx(i:i+bsize,j:j+bsize);
        cooEY = my(i:i+bsize,j:j+bsize);
        X(p:p+(bsize+1)^2-1,:) = [cooEX(:) cooEY(:)];
        p = p + (bsize + 1)^2;
    end
end
```

Appendix C

Convergence analysis

Flat plate

This section includes results from the study of the flat plate in Chapter 4. Figures C.1 and C.2 display the residuals for the solid and the porous case respectively. The residuals in Figures C.1a, C.1c, as well as in C.2a and C.2c, have been computed after each iteration in the solution of the pressure equation in the SIMPLE method. The discontinuity in the plot indicates the end of the solution for a timestep and the beginning of the next one.

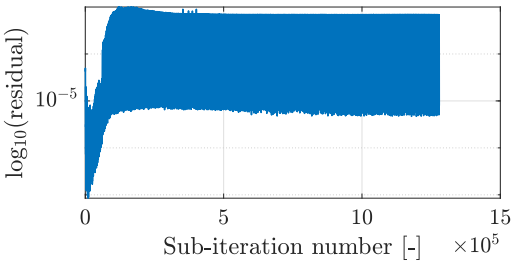

(a) Residuals after pressure equation.

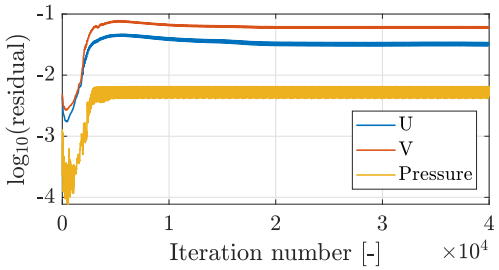

(b) Normalized residuals for velocity and pressure.

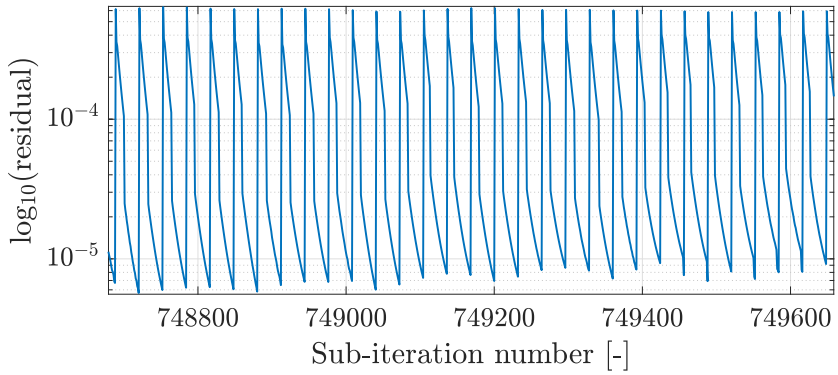

(c) Zoom of Figure C.1a

Figure C.1: Residuals from the simulation of the flat plate with a solid insert.

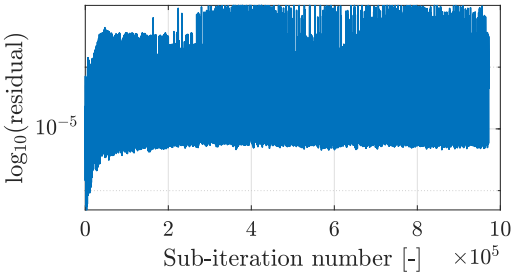

(a) Residuals after pressure equation.

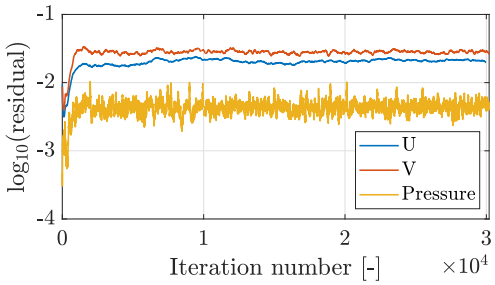

(b) Normalized residuals for velocity and pressure.

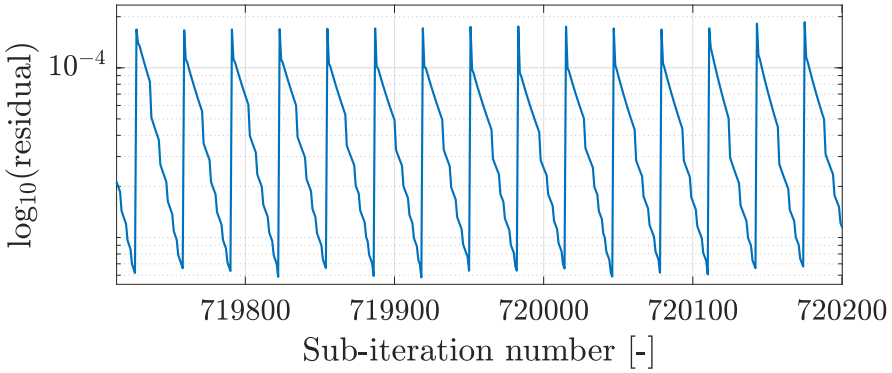

(c) Zoom of Figure C.2a

Figure C.2: Residuals from the simulation of the flat plate with a porous insert.

Airfoil case

This section includes results from the study of partially porous airfoils presented in Chapter 5. Figures C.3a and C.3b display the residuals for the clean and tripped cases respectively. In the clean case, non-dimensional residuals are similar to the

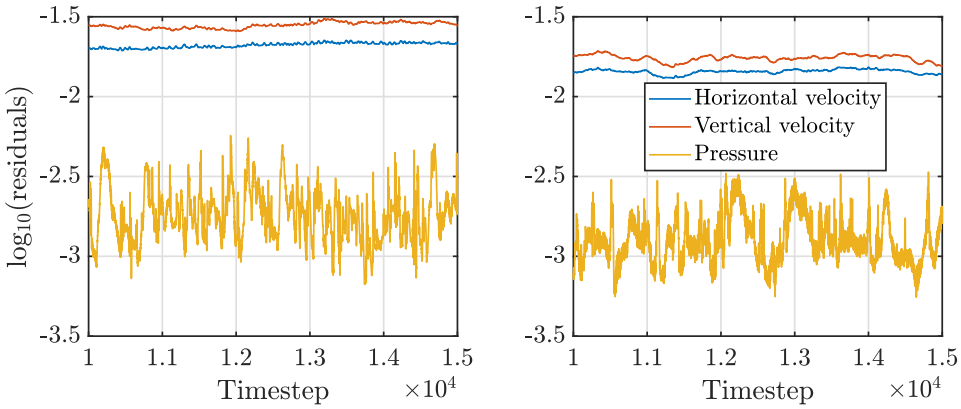

(a) Clean configuration.

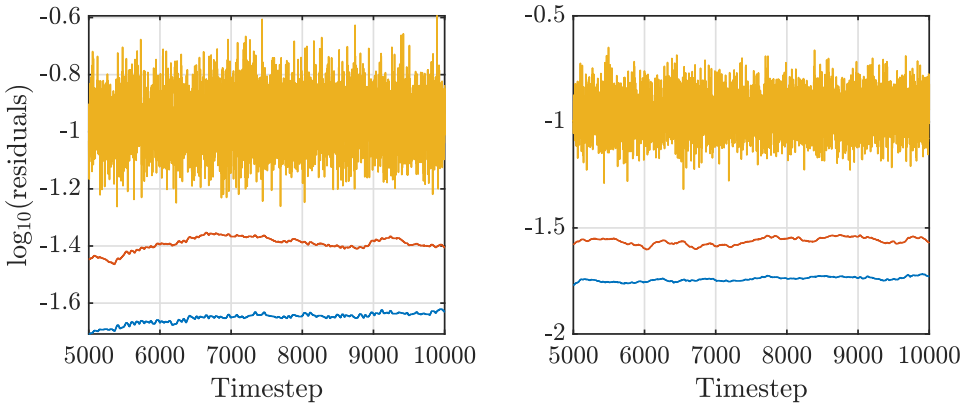

(b) Tripped configuration.

Figure C.3: Sample of convergence history for airfoil case. Residuals are normalized with an accumulated value to account for the entire time history of the simulation. Solid case (left) and porous case (right).

flat plate case. The addition of a porous material does not seem to affect numerical stability. The addition of a perturbation to trip the boundary layer increases the pressure residuals significantly. Furthermore, a higher computational time is needed.

Appendix D

Calibration of hot-wire sensors

This appendix includes the calibration procedure of the hot-wire sensors used in the measurement campaign.
The calibration procedure is required when using hot-wire anemometry technique. It can be a repetitive and sometimes long procedure, which makes it one of the main disadvantages of the technique. Figure D.1 presents an example of a calibration curve obtained in the wind tunnel.

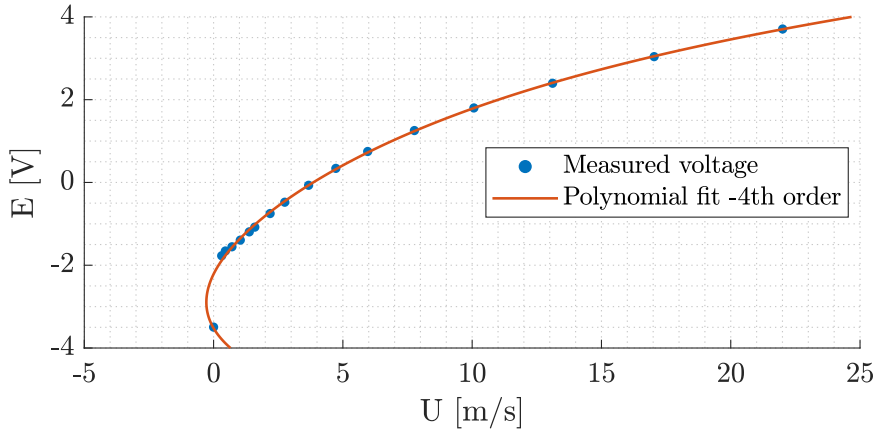

Figure D.1: Calibration curve for hot-wire calibration. A fourth-order polynomial is used to fit the voltage data. It can be seen that the points used for calibration are clustered at low values to improve accuracy in this region.

The first step in the calibration procedure is to measure the cable resistance by placing a shorting probe to close the circuit. Next, the shorting probe is replaced with the hot wire to measure the probe resistance. The operating resistance can then be computed as

$$R_{operating} = R_{tot} + R_{20}\alpha(T - T_e)$$

At this point the voltage output from the sensor was manipulated to restrict (and maximize) it in the range -5 V to + 5 V. This was done by applying a gain and an offset to the voltage output from the Wheatstone bridge to make it readable by the analog to digital converter (which can read only voltages between -5 V and +5 V). As a reference to compute gain and offset, the voltage was recorded at the lowest (i.e. 0 m/s) and highest operating conditions (i.e. 22 m/s).

The velocity calibration was then performed by running the wind tunnel in the range of velocities to be inspected. For this, the probes were placed in the free-stream flow, away from any form of undesired turbulence. The calibrating position is showed in Figure D.2.

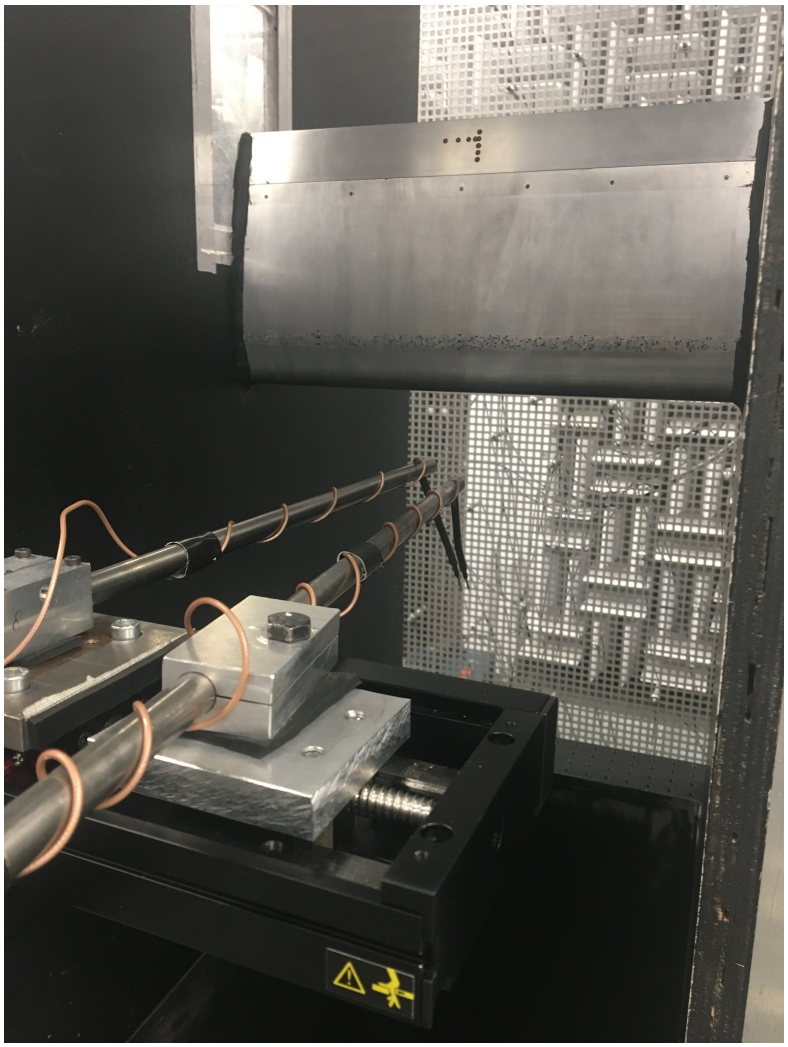

Figure D.2: Calibration position. Once the wires were properly distanced, their calibration could take place.

As visible from Figure D.1, in this experiment it was chosen to calibrate between 0 m/s and 22 m/s. This was done to include all the wind speeds to be tested later. The velocities at which voltage was recorded were chosen to optimize the accuracy of the interpolation. For this reason, the sequence is clustered at lower velocities.
Once the blue dots in Figure D.1 have been acquired, LabVIEW was used to operate the curve fitting, showed in red in Figure D.1. It can be seen that a fourth order polynomial, as predicted by King's Law, provides a good fitting. In the specific case of Figure D.1, the polynomial coefficients were:

$$U(E) = P_1E^4 + P_2E^3 + P_3E^2 + P_4E + P_5$$

$$\begin{aligned} P_1 &= -2 \times 10^{-5} \\ P_2 &= 0.001 \\ P_3 &= -0.04 \\ P_4 &= 0.64 \\ P_5 &= -1.98 \end{aligned}$$

Appendix E

Spanwise coherence and frequency analysis

The experimental work of this master thesis represents part of the work of Alejandro Rubio for his P.h.D. at TU Delft. Although the results presented in this appendix are not directly relevant to this thesis work, they are significant from a research point of view.
In the field of aeroacoustics, a great topic of research deals with the relation between the hydrodynamic quantities in the boundary layer and the broadband trailing edge noise. Amiet's theory provides an analytical model to predict the acoustic emission. The power spectral density of the far-field acoustic pressure emitted by an airfoil can be expressed (for an observer at the midspan plane of the airfoil, i.e. $Z = 0$) as

$$S_{pp}(X, Y, Z = 0, \omega) = \frac{L}{2}\left(\frac{\omega c Y}{4\pi c_0 \sigma^2}\right)|\mathscr{L}|^2 \phi_p \Lambda_{p|z} \tag{E.1}$$

where $\mathscr{L}$ is the acoustically weighted lift function, ϕ_p the power spectral density of surface pressure fluctuations, $\Lambda_{p|z}$ the spanwise coherence length of surface pressure fluctuations. σ is the corrected distance between observer and trailing-edge, defined as $\sigma = X^2 + \beta^2 Y^2$, with $\beta = \sqrt{1 - (U_\infty - c_0)^2}$.
Another useful relation is given by the TNO-Blake model which allows to estimate the product of $\Lambda_{p|z}$ and ϕ_p. In this relationship, $\phi_p \Lambda_{p|z}$ is proportional to the square of the shear $\partial U/\partial y$.
The spanwise space correlation of the signals from the surface microphones $F(r)$ was computed as

$$F(r) = \frac{\overline{p'(y)p'(y+r)}}{\overline{p'^2}} \tag{E.2}$$

with r being the spanwise distance between the microphones. The spanwise cor-

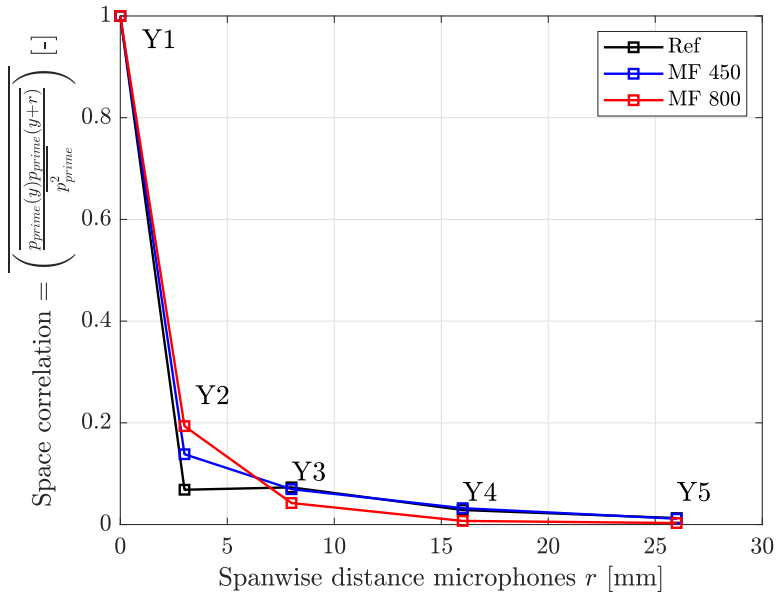

Figure E.1: Spanwise space correlation of pressure signals from surface microphones $F(r)$. The location of the microphones is marked. The location of each microphone can be seen in Figure 6.6.

relation length was then obtained by integrating $F(r)$ along r

$$\Lambda_p = \int_0^\infty F(r)dr \tag{E.3}$$

Table E.1: Relevant hydrodynamic quantities for the estimation of the power spectral density of the far-field acoustic pressure.

	$\Lambda_{p\|z}$ [mm]	$\partial U/\partial y$ [1/s]
Ref	2.57	253.28
MF450	2.85	230.06
MF800	2.63	232.8